Title

Hippocampal Neural Dynamics of Spatial Navigation in the Morris Water Maze

Author

Shahi, Mina

Publication Date

2024

Peer reviewed|Thesis/dissertation

UNIVERSITY OF CALIFORNIA

Los Angeles

Hippocampal Neural Dynamics of Spatial Navigation in the Morris Water Maze

A dissertation submitted in partial satisfaction

of the requirements for the degree

Doctor of Philosophy in Bioengineering

by

Mina Shahi

2024

ABSTRACT OF THE DISSERTATION

Hippocampal Neural Dynamics of Spatial Navigation in the Morris Water Maze

by

Mina Shahi
Doctor of Philosophy in Bioengineering
University of California, Los Angeles, 2024
Professor Peyman Golshani, Co-Chair
Professor Weizhe Hong, Co-Chair

This thesis investigates changes in neural dynamics during spatial learning by recording the activity of large populations of CA1 hippocampal neurons during performance of the Morris water maze (MWM) navigation task.

Employing a generalized linear model, we found significant enhancements in the sparsity of both spatial and head-directional firing rates, indicating more refined neuronal representations after learning. Artificial neural networks successfully decoded position, head direction, and distance-to-platform from neural activity patterns, with decoding accuracy improving as animals mastered the task.

To determine if long-term potentiation (LTP), a form of synaptic plasticity important for learning, was essential for learning associated changes in hippocampal representations, we recorded CA1 hippocampal activity in GluA1^{C2KI} mutant mice, which have impaired CA1 LTP and learning deficits. We found that GluA1^{C2KI} mice exhibited impaired spatial memory consolidation during probe trials, suggesting a specific impairment in the retention of learned spatial information. Single-cell and network analyses in GluA1^{C2KI} mice revealed no significant increase in head-

directional sparsity with learning, nor any notable reduction in decoding error for head-direction, and distance-to-platform information. These findings suggest a potential role of LTP in fine-tuning neural representations associated with task learning. These findings underscore the importance of LTP mechanisms in spatial memory and highlight its implications for cognitive disorders involving spatial navigation deficits.

The dissertation of Mina Shahi is approved.

Mason A. Porter

Jingyi Li

Stephanie Kristin Seidlits

Weizhe Hong, Committee Co-Chair

Peyman Golshani, Committee Co-Chair

University of California, Los Angeles

2024

To my beloved husband Ryan and cherished dog, Niko, for being my constant companions and sources of inspiration.

TABLE OF CONTENTS

LIST OF FIGURES

ACKNOWLEDGMENTS

This work couldn't have been accomplished without the invaluable support, guidance, and contributions of numerous individuals, to whom I owe a deep debt of gratitude.

I would like to extend my sincere gratitude to my esteemed committee members, Dr. Weizhe Hong, Dr. Jingyi J. Li, and Dr. Stephanie Seidlits, for their invaluable support and guidance throughout this journey. I am also deeply thankful to my advisors, Dr. Peyman Golshani and Dr. Mason A. Porter for providing me with the opportunity to work in their esteemed labs and for their unwavering guidance throughout this journey. Their mentorship has been instrumental in shaping this work. Dr. Golshani's mentorship has been invaluable, and I am grateful for the wisdom and insights he shared. Dr. Porter's meticulous approach to science has been a constant source of inspiration, and I am thankful for his careful guidance. Both of my mentors played an invaluable role in guiding me through the toughest moments of my PhD journey. Their persistent support and guidance were the pillars that helped me navigate challenges and emerge stronger. I am deeply grateful for their mentorship and encouragement during those difficult times.

I am deeply grateful to Dr. Ronen Reshef, whose immense support and collaboration have been invaluable in tackling this challenging project together. This project wouldn't have been possible without overcoming all the challenges during the experiments and recording the data that he patiently collected. Moreover, his presence and readiness to assist whenever I needed guidance have been vital to my progress in this endeavor.

I would like to express my sincere appreciation to the members of Dr. Golshani's lab, Dr. Samara Miller, Dr. Liron Sheintuch, Dr. Arash Bellafard, Dr. Pingping Zhao, Blake Madruga, Conor Dorian, Douglas Vormstein-Schneider, Diego Espino, Dr. Yan Jin, Dr. Karen Safaryan, and Dr. Long Yang, for their feedback during our discussions and lab meetings. Their support and constructive criticism have significantly contributed to the development of this thesis. I would also like to extend my gratitude to Zoe Day for her invaluable help, support, and exceptional role as our lab manager. Working with her has been incredibly smooth, thanks to her efficiency and

dedication.

Special thanks are also due to Chengfeng Jiang for his indispensable assistance with the statistical questions I encountered. His patience and willingness to spend time answering my questions were immensely helpful.

Additionally, I would like to express my profound gratitude to my family. My father Khosrow, especially, has been a consistent source of support and love, and my mentor throughout my life's journey. From my earliest days, his encouragement, often through challenging puzzles that fueled my curiosity, has shaped the way I think and approach problems. During difficult moments, his wisdom and steadfast support have been providing me with strength and motivation. Equally important is my mother, Roghi, whose nurturing guidance, endless patience, and unconditional love have been the cornerstone of my journey. Their belief in my abilities has instilled confidence in me and shaped me into the person I am today. Moreover, I want to express my deep gratitude to my sister, Maryam, for her unconditional love, support, and belief in me. Your encouragement has been a constant source of motivation, and your readiness to help and support me never ceases to amaze me. Your remarkable intuition allows you to understand my needs even before I articulate them, and I am truly grateful for your innate ability to anticipate and provide support.

Last but certainly not least, I want to express my heartfelt gratitude to my better half, Ryan, and my beloved dog, Niko. You both bring immeasurable joy and support to my life. Ryan, your unwavering encouragement and understanding have been my anchor throughout this journey. From the first day of my PhD, you've been by my side, offering a level of support that exceeds my wildest expectations. Your steadfast presence has continually amazed me, and I'm grateful for every moment we've shared. Niko, your presence is a source of calm and serenity in my life and melts away all my stresses. Your selflessness and exceptional loyalty make you the best friend I could ever wish for. Thank you, Ryan and Niko, for making this journey more beautiful.

VITA

2008 B.Sc. Computer Science, Sharif University of Technology, Tehran, Iran

2014 M.Sc. Cognitive Science, Osnabrueck University, Osnabrueck, Germany

PUBLICATIONS AND PRESENTATIONS

Shahi, Mina*, Carl van Vreeswijk, and Gordon Pipa. *"Serial Spike Time Correlations Affect Probability Distribution of Joint Spike Events."* Frontiers in computational neuroscience 10 (2016): 139.

Mina Shahi*, Carl van Vreeskwijk, Gordon Pipa. *"Serial Spike Time Correlations Affect Probability Distribution of Joint Spike Events."* Society for Neuroscience Conference, San Diego 2016.

Shonali Dhingra*, R. Sandler, R. Rios, C. Vuong, M. Shahi, L. Acharya, A. Hachisuka, Mayank Mehta.*"Visual cues evoke object-centric directional tuning across the entire hippocampal place cell ensemble."* Society for Neuroscience Conference, Washington DC 2017.

Mina Shahi*, R. Sandler, S. Dhingra, R. Rios, C. Vuong, L. Acharya, A. Hachisuka, Mayank Mehta.*"A generalized linear model approach to dissociate object-centric and allocentric directional responses in hippocampal place cells."* Society for Neuroscience Conference, Washington DC 2017.

Mina Shahi*, S. Dhingra, R. Sandler, R. Rios, C. Vuong, L. Acharya, Mayank Mehta.*"A statistical model-based approach to decipher the mechanisms governing spatial and directional tuning of*

hippocampal neurons." Society for Neuroscience Conference, San Diego 2018.

Mina Shahi*, S. Dhingra, R. Sandler, R. Rios, C. Vuong, L. Acharya, M. R. Acharya.*"Hippocampal Anchor Fields."* Society for Neuroscience Conference, Chicago 2019.

Ronen Reshef*, Mina Shahi, Peyman Golshani.*"Hippocampal neural dynamics of spatial navigation in the Morris water."* Society for Neuroscience Conference, Virtual 2021.

Ronen Reshef*, Mina Shahi, Daniel Aharoni, Peyman Golshani.*"Hippocampal neural dynamics of spatial navigation in the Morris Water Maze: Spatial learning is dependent on CA1 map and compass coding."* Society for Neuroscience Conference, San Diego 2022.

Ronen Reshef*, Mina Shahi, Tom J. O'dell, Daniel Aharoni, Peyman Golshani.*"Improved coding of head direction and spatial location during spatial learning in the morris water maze are differentially affected by loss of long-term potentiation."* Society for Neuroscience Conference, Washington DC 2023.

CHAPTER 1

Introduction

Learning and memory underpin the acquisition of new skills [CB10], adaptive behavior [PAF05], decision-making [Eic17], ability to recall information [Squ92] and personal experience [Eic00], cognitive development [Nel00], problem solving [And13], and ability to navigate [ON79, MKM08, SB15], silently orchestrate behind the scenes.

Among various forms of learning, spatial learning stands out as critical for the animal. The skill of navigating the physical world, grasping spatial relationships, and constructing mental maps isn't merely a cognitive luxury; it is a fundamental necessity for the survival of almost all vertebrates. Animals rely on spatial memory to help them locate water and food, and evade predators and physical hazards. This remarkable ability hinges on the development of a mental representation of the external world, highlighting the intricate interplay between spatial learning, memory, and the adaptive capacities vital for survival.

1.1 Hippocampus and spatial representation

Unraveling the neural basis for learning and memory has been an intense topic of investigation for nearly a century. The foundational work that initially linked the hippocampus to learning and memory was conducted by Brenda Milner and William Beecher Scoville in the 1950s [SM57]. The famous case study involved patient H.M. (Henry Molaison), who had undergone bilateral removal of the medial temporal lobes, including the hippocampus, to treat severe epilepsy.

The study revealed that H.M. experienced profound anterograde amnesia and was unable to

form new memories after the surgery. This groundbreaking research provided crucial insights into the role of the hippocampus in memory formation. Brenda Milner's extensive work with H.M. significantly contributed to our understanding of the neural basis of memory and the importance of the hippocampus in the process [Mil70, MCT68, SW11].

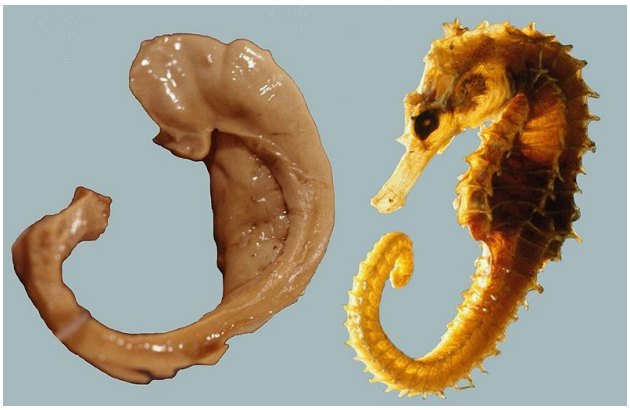

Figure 1.1: HIPPOCAMPUS
Left: Human hippocampus. Right: Seahore. Prepared by Laszlo Seress, 1980. Source: Wikipedia (https://en.wikipedia.org/wiki/Hippocampus)

The primary regions within the hippocampus include:

1. **Dentate Gyrus (DG)**

   The dentate gyrus, an essential component of the hippocampal formation, receives input from the entorhinal cortex, a key region responsible for initial sensory information processing. This input is conveyed through the perforant path, a major input pathway to the hippocampus. The granule cells of the dentate gyrus project axons, known as mossy fibers, to the CA3 region of the hippocampus. The dentate gyrus is believed to contribute significantly to pattern separation [YLS11, SMM12, BSM16], the ability to discern and encode distinct memories from similar experiences. Additionally, it plays a crucial role in spatial memory, participating in the encoding and retrieval of information related to spatial contexts [NPJ99, KTW07, SGN09]. Notably, the dentate gyrus stands out as one of the few brain regions where neurogenesis, the generation of new neurons, persists throughout an individual's lifespan [EPB98, GRG99].

2. **Cornu Ammonis 1 (CA1)**

   The CA1 region, a subfield within the hippocampal formation receives input from the entorhinal cortex and the CA3 region and for extrahippocampal regions, it receives input from pallidum, striatum, hypothalamus, and the nucleus reuniens of the thalamus [TWP21]. Following the processing of the information, CA1 serves as a critical output region, directing signals to the subiculum and entorhinal cortex. The principal neurons in CA1 are pyramidal cells. Renowned for its pivotal role in memory formation and spatial navigation, CA1 is vital for the integration and consolidation of information [ON79, MM98, THT96, MBM94, EPJ17]. Damage to CA1 can result in memory impairments, impacting both episodic and spatial memory functions [SBH01, ZSA86]. Furthermore, disruptions in CA1 function have been implicated in various neurological and psychiatric disorders. These may include conditions such as Alzheimer's disease [SPS07, GAC10], epilepsy [Wal15], and other cognitive or mood disorders [MF11, BFW11, LSL07].

3. **Cornu Ammonis 2 (CA2)**

   Nestled between CA1 and CA3 in the hippocampus, CA2 has historically received less attention, but recent studies have unveiled its unique functions. Positioned as an intermediate link, CA2 receives input from the entorhinal cortex and CA3, sending output to CA1. Notably, CA2 is critical for social memory processing, contributing to the understanding of complex cognitive functions in the hippocampus [HS14, SWC16, MLB18].

4. **Cornu Ammonis 3 (CA3)**

   The CA3 region, situated within the hippocampus between CA2 and the DG, forms a densely interconnected network of neurons. Its intricate neural circuitry involves receiving primary input from the DG and collateral input from neighboring CA3 neurons. Through its output, notably via the Schaffer collateral pathway, CA3 communicates with other hippocampal regions, including CA1. A key feature of CA3 is its recurrent connectivity, facilitating the formation of pattern completion—an ability to retrieve complete memories from partial or incomplete cues [LL07, YLS11]. Beyond this, CA3 plays crucial roles in associative

learning [GMD06], enabling connections between stimuli or events, as well as in spatial [SSM02, GK06, GB09] and episodic memory, contributing to the encoding and retrieval of specific personal experiences [KHW08, MCA20].

5. **Subiculum**

   The subiculum, situated in the hippocampal formation near CA1 and the dentate gyrus, receives inputs from various regions, including CA1 and the entorhinal cortex. It serves as a major output pathway, projecting to several regions, including the entorhinal cortex (with reciprocal connections), prefrontal cortex, and amygdala. In addition to its primary functions in information integration [OM06], memory consolidation [GBD97, BWF09], spatial navigation [SM85, MST90], decision-making [WMS17], and contextual memory [OSB09], the subiculum may have other roles and contributions within the broader cognitive processes of the brain.

1.2 Diverse response properties

Various studies in neuroscience have revealed a diverse array of neuronal responses which have been hypothesized to be crucial for spatial navigation. Here are a few notable contributors:

1. **Place cells**

   Place cells are a subset of neurons that exhibit activity specifically when an animal is in a particular location within its environment, often referred to as the 'place field' [OD71]. Place cells have been hypothesized to play a pivotal role in spatial cognition. These neurons showcase sensitivity to the geometry and distinctive features of the surrounding environment, contributing to the formation of a mental map. (see section 1.6)

2. **Head-direction cells**

   Head-direction cells are specialized neurons that respond specifically to the orientation of an animal's head in space. These neurons exhibit firing patterns independent of the

animal's location in space. They are commonly found in various brain regions, including the postsubiculum [TMR90], thalamus [MW93, Tau95], CA1 region of the hippocampus [LRM00, AAV16], and the entorhinal cortex [GSB14].

3. **Gird cells**

   Grid cells, along with place cells, play a crucial role in creating spatial map of the environment. Located in the entorhinal cortex, these neurons exhibit a distinctive firing pattern—a hexagonal grid-like arrangement—spanning the animal's navigated space [HFM05]. This unique firing pattern contributes significantly to the brain's ability to create a comprehensive cognitive map, allowing for precise and effective navigation through diverse surroundings.

4. **Boundary-vector cells (BVCs)**

   BVC cells are a subset of cells within the subiculum that exhibit maximal firing when the animal is positioned at a preferred distance and allocentric direction from the boundary of its environment [BLH06, LBJ09].

5. **Boarder cells**

   Border cells are particularly responsive to the proximity of environmental boundaries, and they exhibit increased activity when an animal is closer to the border of the environment. These specialized cells are found in the entorhinal cortex [SBK08, SYK08].

6. **Speed cells**

   Speed cells, a type of neurons located in the entorhinal cortex, exhibit firing patterns that intricately correspond to the speed at which an animal navigates through its environment [KCM15].

7. **Time cells**

   Time cells are neurons that exhibit a distinctive firing pattern during successive moments within temporally organized period. These unique neural elements have been observed in the CA1 region of the hippocampus [MLE11, TPD20].

8. **Object-vector cells (OVCs)**

   OVC cells are a distinct class of neurons found in the entorhinal cortex, exhibiting responses when an animal occupies a preferred distance and direction relative to an object in its environment [HSA19].

1.3 Different behavioral paradigms to study navigation

Researchers employ a variety of mazes to study navigation, selecting specific mazes based on the questions they aim to answer. Different mazes and navigation tasks are chosen to unravel the complexities of spatial cognition. Commonly used mazes include:

1. **Linear track**

   A linear track is a confined, straight pathway where animals move from one end to the other, enclosed by walls to maintain the animal within the designated area (Figure 1.2 (a)).

2. **Radial arm maze**

   A radial arm maze features a central platform from which several arms extend outward. The task for the animals is to discriminate between rewarded and non-rewarded arms, navigating to the former while abstaining from the latter. Distal cues play a crucial role in aiding the animals to navigate the radial arm maze and remember the locations of arms with rewards (Figure 1.2 (b).

3. **Morris water maze**

   The Morris water maze is a circular pool filled with opaque water. A hidden escape platform is submerged below the water's surface. The animal's task is to navigate and locate the hidden platform, relying on distal visual cues on the surrounding walls (Figure 1.2 (c)).

4. **Barnes maze**

   The Barnes maze is a circular platform with a dry surface featuring several indistinguishable holes, with only one serving as the target escape hole. The animal's objective is to locate the

specific escape hole amidst the others, utilizing distal visual cues on the surrounding walls (Figure 1.2 (d)).

5. **T-maze**

   The T-maze is shaped like the letter 'T', and features a central stem with two arms extending from it. Animals commence at the stem's starting point and navigates towards one of the arms containing a reward (Figure 1.2 (e)).

6. **Y-maze**

   The Y-maze exhibits a distinctive Y-shaped configuration with three arms extending from a central point. Notably, all three arms are similar, and the animal faces a trinary choice. In contrast, the T-maze features a simpler design with two similar arms, presenting a binary choice for the animal to navigate between (Figure 1.2 (f)).

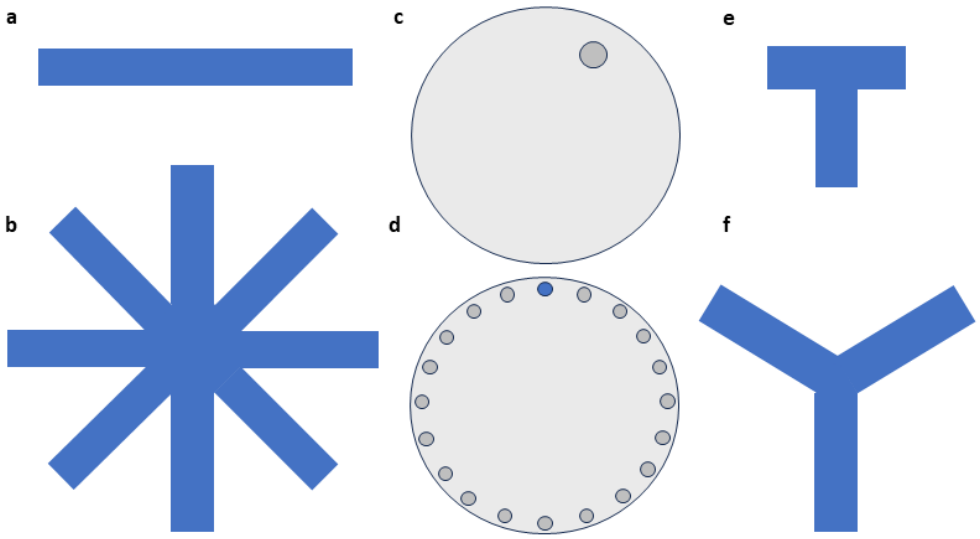

Figure 1.2: SPATIAL LEARNING ASSESSMENT MAZES
A diverse array of mazes designed to study spatial navigation. **(a)** Linear track. **(b)** Radial arm maze. **(c)** Morris water maze. **(d)** Barnes maze. **(e)** T-maze. **(f)** Y-maze.

1.4 Neural learning mechanisms: synapses and beyond

The brain employs diverse learning rules to adapt and extract knowledge from its environment. Among these, synaptic plasticity emerges as a prominent mechanism. Synapses, the intracellular junctions where neurons communicate, undergo dynamic changes through synaptic plasticity. These alterations shape how neurons respond to experiences and environmental changes, facilitating the formation of memories. This intricate process involves the modification of synaptic strength and efficacy such as, increased neurotransmitter release and changes in both the number and sensitivity of neurotransmitter receptors.

Several well-established synaptic plasticity learning rules govern the adaptive capabilities of neural networks. Donald Hebb's seminal statement [Heb05], "cells that fire together wire together", encapsulates a foundational principle of synaptic plasticity. According to Hebbian learning, when the activity of a presynaptic neuron is succeeded by the activation of a postsynaptic neuron, the connection between them strengthens. A more refined and temporally specific variation of this concept is embodied in the spike-timing-dependent plasticity (STDP) rule. STDP dictates that the relative timing of spikes between presynaptic and postsynaptic neurons critically influences synaptic modifications. Specifically, if the presynaptic spike precedes the postsynaptic spike, it induces long-term potentiation (LTP), enhancing synaptic strength. Conversely, if the postsynaptic spike precedes the presynaptic spike, long-term depression (LTD) occurs, leading to synaptic weakening. The excitatory postsynaptic potential (EPSP), quantified in millivolts (mV), indicates the degree of depolarization in the postsynaptic membrane resulting from excitatory synaptic input. Multiple factors shape the EPSP, including the synaptic connection's strength, the number of open ion channels, and the inherent characteristics of the postsynaptic membrane. Figure 1.3 depicts how the timing of pre and post-synaptic spikes can trigger either synaptic potentiation or depression.

Another notable form of synaptic plasticity that can lead to LTP or LTD is Burst-Time-Dependent Plasticity (BTDP) [BKS07]. This rule takes into account the precise timing of burst firing—rapid sequences of action potentials—the frequency of spikes, and the temporal organization of spikes

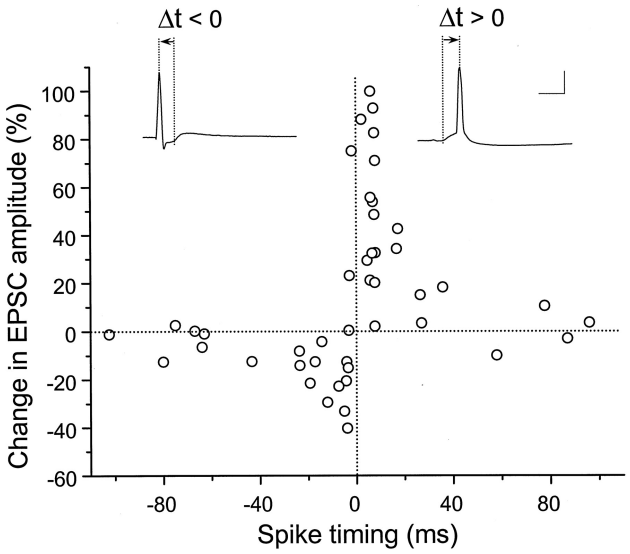

Figure 1.3: SPIKE-TIMING-DEPENDENT PLASTICITY
In Spike-Timing-Dependent Plasticity (STDP), the precise timing of activation between the pre and post neurons critically determines the induction of synaptic potentiation or depression. When the presynaptic neuron fires before the postsynaptic neuron, it results in synaptic potentiation. Conversely, if the postsynaptic neuron fires before the presynaptic neuron, this leads to synaptic depression. Prepared by Bi and Poo, 1998 [BP98]. Copyright [1998] Society for Neuroscience.

within bursts to determine how synaptic connections are modified.

STDP and BTDP have been mainly studied in-vitro, and evidence for the induction of behaviorally specific forms of potentiation has been found in-vivo. The study conducted by Bittner et al. unveiled a novel synaptic plasticity termed behavioral time scale synaptic plasticity (BTSP) in hippocampal area CA1. This newly identified mechanism facilitates rapid formation of place fields by potentiating inputs that were active up to several seconds before the occurrence of a large plateau potential. Unlike Hebbian plasticity reliant on repetitive activations during milliseconds interval, behavioral time scale synaptic plasticity operates on a seconds-long scale, efficiently encoding entire behavioral sequences within synaptic weights [BMG17, MLB21].

Additionally, homeostatic plasticity operates maintains stability and balance in neural network activity[TN04]. The primary objective of homeostatic plasticity is to adjust synaptic strength, ensuring that neural circuits remain within a functional range of activity. For instance, if a neuron is excessively active, homeostatic plasticity mechanisms act to decrease its activity, and conversely,

if the neuron is insufficiently active, it strengthens synapses to enhance neural activity.

Beyond synaptic plasticity, the brain exhibits additional mechanisms of learning, including structural plasticity [HS09] and intrinsic plasticity [ZL03]. Structural plasticity involves a multifaceted process that includes the formation of new synapses (synaptogenesis), the elimination of existing ones (synaptic pruning), and changes in dendritic spine morphology. These dynamic alterations contribute to the continuous rewiring and adaptation of neural circuits, enabling the brain to refine its connectivity based on experiences and environmental demands. Intrinsic plasticity, on the other hand, encompasses modifications in the intrinsic properties of individual neurons, such as ion channel properties and membrane potential. By adjusting these intrinsic features, neurons can finely tune their excitability in response to varying input patterns and activity levels.

1.5 Role of NMDA and AMPA receptors in spatial learning

LTP stands as a critical mechanism in the processes governing learning and memory. NMDA (N-methyl-D-aspartate), glutamate receptors, play a pivotal role in both the induction and expression of LTP. Seminal studies by Morris and colleagues [MAL86, Mor89] demonstrated that the NMDA receptor antagonist AP5 blocked LTP, and lead to impairments in spatial learning. Further investigations utilizing genetic knockout approaches targeting NMDA receptors provided compelling evidence of deficits in LTP induction to impairments in spatial navigation [SPW92, GOK92]. Additionally, research by McHugh et al. [MBT96] showed that mutant mice with the NMDAR1 gene knocked out exclusively in the pyramidal cells of the CA1 subregion of the hippocampus exhibited impaired LTP in the CA1 region and deficits in spatial selectivity. Disruption of genes encoding Ca2+/calmodulin-dependent kinase II (CaMKII) similarly resulted in impaired hippocampal LTP and spatial navigation in water maze tasks [SPW92]. Furthermore, Sakimura et al. [SKI95] demonstrated that mice lacking the NMDA receptor 1 subunit exhibited reduced hippocampal LTP and impaired spatial learning. These collective findings underscore the integral role of NMDA receptors in LTP and emphasize their consequential impact on spatial memory and navigation.

Additionally, AMPA (α-amino-3-hydroxy-5-methyl-4-isoxazolepropionic acid) receptors, another type of glutamate receptor, contribute to the early phase of LTP. The inhibition or blockade of AMPA receptors leads to the prevention of fast excitatory postsynaptic potentials (EPSPs). In their 2018 study, Zhou et al. investigated three novel mouse lines: GluA1^{C2KI} mice, where the C-terminal domains (CTDs) of GluA1 were replaced by CTDs of GluA2; GluA2^{C1KI} mice, where the CTDs of GluA2 were replaced by CTDs of GluA1; and GluA1^{C2KI};GluA2^{C1KI} mice, obtained by crossing the previous two strains, resulting in swapping the CTDs of GluA1 and GluA2.

The study found that GluA1^{C2KI} mice exhibited impaired LTP and intact LTD, along with deficits in spatial learning. Conversely, GluA2^{C1KI} mice showed increased LTP and impaired LTD, along with deficits in contextual fear memory. Interestingly, both LTP and LTD were restored in GluA1^{C2KI};GluA2^{C1KI} mice, indicating that the CTDs of GluA1 and GluA2 are necessary and sufficient domains within the AMPA receptors for NMDAR-LTP and NMDAR-LTD[ZLX18].

1.6 Hippocampal dynamics in spatial navigation

Numerous studies have underscored the profound impact of visual cues—both proximal and distal—on hippocampal neurons. Müller et al. (1987) demonstrated that rotating cue cards on a wall could elicit a corresponding rotation of place fields in hippocampal cells, while alterations in environmental size could lead to remapping or scaling of place fields [MK87]. Similarly, Quirk et al. (1990) highlighted how transitioning animals from light to dark environments could affect place fields, emphasizing the pivotal role of visual cues in spatial representation [QMK90]. Markus et al. (1995) further illustrated that remapping occurred in response to changes in behavioral context, such as random foraging versus systematic movement between goal locations, despite environmental consistency [MQL95].

Moreover, research into head direction selectivity in hippocampal neurons has unveiled directional preferences across various spatial environments. Battaglia et al. (2004) identified directional selectivity in hippocampal neurons within a one-dimensional real world (RW) setting, while Ravas-

sard et al. (2013) observed similar selectivity in a virtual reality (VR) setting where animals navigated along a linear track [BSM04, RKW13]. Acharya et al. (2016) expanded on these findings, showing that visual cues in VR could directly influence directional selectivity during two-dimensional random foraging tasks, emphasizing the dispensability of vestibular cues for this directional selectivity in hippocampus [AAV16].

However, questions remain regarding how place cells and head direction cells adapt as animals learn spatial navigation tasks. Sarel et al. (2017) conducted experiments with Egyptian fruit bats, tasking them with flying from place A to place B, designated as their goal. Their research revealed a distinct subpopulation of neurons exhibiting directional selectivity toward the goal, persisting even when the goal was concealed. Additionally, these neurons displayed selectivity based on the distance to the goal, with heightened activity observed when the bat approached the goal vicinity [SFL17]. In a separate study, Hollup et al. (2001) investigated place cell activity in an annular water maze. They observed a pronounced accumulation of firing near the platform, suggesting a spatially specific response in hippocampal neurons [HMD01]. This suggests that enhanced stabilization of place fields near a 'reward zone' could form the basis for spatial learning. Similarly, Kentros et al. (2004) revealed a significant enhancement in the long-term stability of place field representations in animals performing spatial learning in their study. Their study involved animals engaged in random foraging behaviors, which were unexpectedly exposed to loud noises and bright lights, prompting them to seek refuge in unmarked areas—analogous to the hidden platform scenario in the Morris water maze task, aimed at terminating the auditory and visual stimuli. Remarkably, Kentros and colleagues found that the stability of the place fields was significantly higher in this task compared to animals solely engaged in random foraging [KAS04]. These results suggest stability of a single map for the environment between different sessions only when goal navigation was performed.

Further insights into hippocampal function come from studies employing virtual reality Morris water maze (VR MWM) tasks [MCA21]. Moore et al. (2021) investigated spatial learning within VR MWM environments, where animals relied exclusively on distal visual cues for navigation [MCA21]. Their research revealed the existence of distinct neural subpopulations encoding

parameters such as path distance traveled from the starting point. Additionally, they observed head-direction cells with peak angles clustered towards the platform. Notably, Moore and colleagues found a significant positive correlation between the selectivity of these cells and animal performance. Their results also show degraded place coding due to the VR setting. Thus, their model claims for the use of path integration to solve the 2-D goal navigation, the combination of coding for path distance and head direction.

1.7 Imaging large-scale neural activity in the MWM: a new approach for understanding changes in neural dynamics driving learning

Despite the progress made in understanding hippocampal dynamics through spatial navigation, existing studies often face limitations, such as the reliance on simplified 1D tasks or VR setups lacking vestibular cues. The first is a very degraded form of navigation and the second does not model navigation as it is implemented in nature. To overcome these shortcomings, we implemented a MWM task conducted in the real world, thereby incorporating both vestibular and visual distal cues while eliminating proximal cues. Furthermore, we employed miniscope calcium imaging to capture neural activity over extended periods, enabling a comprehensive examination of hippocampal responses during spatial learning. Additionally, we utilized AMPA knockout mice to utilized GluA1^{C2KI} to disrupt LTP, allowing us to explore how neural responses evolve during spatial navigation tasks under altered synaptic plasticity conditions.

1.8 Calcium imaging as a tool for studying population neural dynamics during navigation

Calcium imaging offers a powerful and widely embraced microscopy technique to monitor neuronal activity in vivo [THM09, NSL16, KMS20, RDR20, SAC20]. This method capitalizes on the intrinsic relationship between neural activity and the influx of calcium ions into active neurons

through voltage-gated calcium channels, ultimately leading to the emission of fluorescence. Here's a breakdown of the key steps in how calcium imaging works:

1. **Calcium Indicators**

   When a neuron fires action potentials, there is activation of voltage-gated calcium channels resulting in a rise in intracellular calcium concentration. Researchers detect this activity by employing calcium-sensitive fluorescent indicators. Two main types exist: genetically encoded calcium indicators (GECIs) and synthetic calcium-sensitive dyes. GECIs [GPT85], like GCAMPs [NOI01], are often introduced using viral vectors such as adeno-associated viruses (AAVs).

2. **Tissue Excitation**

   After the introduction of GCAMP into neurons, the tissue undergoes illumination with a light source [SY06] to excite the calcium indicator molecule. This step is crucial since an excited state is necessary for the calcium indicator to emit fluorescence upon binding with calcium.

3. **Fluorescence Emission**

   Once the calcium indicator molecule is in its excited state, it stands ready to emits fluorescence upon binding with calcium ions. When a neuron becomes active, there's an influx of calcium ions that bind with the already excited calcium indicator molecules, leading to the emission of fluorescence.

4. **Imaging**

   The emitted fluorescence from the calcium indicator molecules is captured by a camera, recording the neuronal activity [GBC11, CAS16, SAC20]. Higher fluorescence intensity correlates with a higher number of neuronal spikes, providing insights into the intensity of neural activity.

1.9 Artificial neural network decoders

Artificial neural networks have emerged as an invaluable tool in neuroscience for several reasons. The utility of these networks arises due to multiple key features: 1. Neural networks adeptly capture intricate and nonlinear relationships in dynamic brain activity, overcoming challenges traditional decoding methods face. 2. They learn from data through training, associating neural patterns with desired outputs for predictions on new, unseen data. 3. Neural networks automatically extract crucial features during training, vital for identifying meaningful signals and understanding brain function. 4. Their efficiency in real-time processing makes them indispensable for applications like brain-machine interfaces, ensuring prompt decoding for responsive control. 5. the versatility of neural networks allows customization for diverse decoding tasks, accommodating both simple linear models and complex deep networks tailored to the intricacies of neural signals and decoding requirements. Examples of such models include the Kalman filter, Support Vector Regression, Extreme Gradient Boosting, Feedforward Neural Network, Gated Recurrent Unit, Simple Recurrent Neural Network, Long Short-Term Memory Network, and Naive Bayes. Moreover, the nature of the output determines whether the model functions as a regressor or a classifier. If the output is a continuous variable, such as position, the decoder operates as a regression model. On the other hand, if the output is discrete, like binary decisions, the model functions as a classifier.

CHAPTER 2

General Methods

This section will outline the methods utilized in this study[1].

2.1 Animals

Ethical Approval: All experimental protocols received approval from the Chancellor's Animal Research Committee of the University of California, Los Angeles (UCLA), and were conducted in adherence to the US National Institutes of Health (NIH) guidelines.

Animal Subjects: For the MWM experiments, a total of 10, 10-week-old hybrid male B6129SF1/J1 (Jackson Laboratories, 10143) or B6129SF2 mice were utilized. These mice were group-housed (2–5 per cage) on a 12-hour light–dark cycle. Hybrid mice were chosen for their improved learning abilities in the Morris water maze task [SFM97]. Male mice were preferred due to their larger size at the appropriate age, facilitating better performance in the swimming tasks with the miniscope.

Strain and Genetic Background: A total of 5 GluA1^{C2KI} LTP deficient mice, provided by the Zhenping Jia lab on a C57/BL6 background [ZLX18], were crossed with S129 mice (Jackson Laboratories, 002448)) to obtain second-generation hybrids homozygous for the mutation and their littermate controls (B6129SF2).

[1]The research and experiments described in Chapters 2 and 3 were collaboratively conducted by Ronen Reshef, Thomas J. O'Dell, and myself. Ronen Reshef conducted the experiments, performed the surgeries, and collected the data. Thomas J. O'Dell specifically conducted the Long-Term Potentiation experiment, as detailed in Section 3.8. My contribution involved analyzing the collected data

Group Assignment and Blinding: Mice were randomly assigned to either control or LTP deficient groups. Blinding procedures were implemented during both data collection and analysis stages, ensuring unbiased interpretation of results.

2.2 Calcium imaging surgeries

For all surgeries, mice were anesthetized with 1.5–2.0% isoflurane and placed into a stereotactic frame (David Kopf Instruments). Lidocaine (2%, Akorn) was applied to the sterilized incision site as an analgesic, and subcutaneous saline injections were administered throughout each surgical procedure to prevent dehydration.

For calcium imaging experiments, all mice underwent two stereotaxic surgeries. First, mice were unilaterally injected with 500 nl of AAV1.Syn.jGCaMP7f.WPRE virus at 1 nl per second in the dorsal CA1 (-2 mm anteroposterior relative to bregma, +2.0 mmm mediolateral from bregma, and 1.6 mm ventral from the skull surface) using a Nanoject microinjector (Drummond Scientific). Then, mice underwent a GRIN lens implantation surgery. A craniotomy 2 mm in diameter was performed above the viral injection site. The cortical tissue above the targeted implant site was carefully aspirated using 27-gauge and 30-gauge blunt needles. Buffered ACSF was constantly applied throughout the aspiration to prevent desiccation of the tissue. The aspiration ceased after partial removal of the corpus callosum and full termination of bleeding, at which point a GRIN lens (1.8 mm diameter, 4.31 mm length, 0.25 pitch, 0.50 numerical aperture, Edmund Optics) was stereotaxically lowered to the targeted implant site (-1.3 mm dorsoventral from the skull surface relative to the most posterior point of the craniotomy). Cyanoacrylate glue and dental cement were used to seal and cover the exposed skull, and Kwik-Sil covered the exposed GRIN lens. Carprofen (5 mg kg^{-1}) and dexamethasone (0.2 mg kg^{-1}) were administered [SAC20] during surgery and for 7 days after surgery together with amoxicillin (0.25 mg ml^{-1}) in the drinking water. Animals were anesthetized again 3 weeks later, and a miniature microscope locked onto an aluminum baseplate was placed on top of the GRIN lens. After searching the field of view for in-focus blood vessels

and cells, the baseplate was cemented into place and the miniscope was unlocked and detached from the baseplate. A plastic cap was locked into the baseplate to prevent debris build-up.

2.3 Wire-free miniscope

The wire-free miniscope is a modified version of the wired miniscope described previously [CAS16, SAC20], with the additional features of being battery-powered and logging imaging data onto onboard removable memory. The optics, Delrin housing, and excitation light source of the wired and wire-free miniscope are identical but the complementary metal oxide semiconductor (CMOS) imaging sensor electronics and data acquisition electronics were redesigned and packaged onto a single printed circuit board (PCB) to enable wire-free operation. All electrical components were chosen to minimize power consumption and weight. The main components of the wire-free PCB were a low-power CMOS imaging sensor (Teledyne E2V, JADE EV76C454), ARM Cortex M7 microcontroller (Atmel, ATSAME70N21A), and microSD card mount (Molex, 0475710001). The PCB also includes necessary voltage regulators, an SD card voltage translation transceiver (Texas Instruments, TXS0206AYFPR), a custom excitation LED current-driving circuitry, a battery connector, and a 12 MHz oscillator. A single-cell lithium-polymer battery (Power Stream, GM041215, 45 mAH, 1.1 g) was attached to the side of the miniscope and connected to the wire-free PCB during operation. The upper limit on the length of recording sessions was determined by the size and efficiency of the battery. Storage space was not a limiting factor as microSD cards can now store up to 1 TB of data (147 h of continuous recording). Using 45 mAh batteries we reliably recorded for at least 30 min. Overall, the wire-free miniscope weighs 4–5 g, depending on the imaging sensor and battery used. Following power-up, the microcontroller (MCU) accessed configuration information, programmed by custom PC software, in a specific memory block of the microSD card that held recording parameters such as recording length, frame rate, excitation LED intensity, imaging resolution, and imaging exposure length. Once the configuration was complete, the MCU waited 5 seconds before beginning recording, at which time the excitation LED and

onboard status LED turned on. At the end of the configurable recording duration, the excitation LED and onboard status LED turned off and the MCU terminated data logging onto the microSD card. Offline synchronization of the miniscope recording with a behavioral camera was achieved by detecting the on-and-off event of the status LED of the miniscope. Pixel values from the CMOS imaging sensor were clocked into a three-frame circular buffer in the MCU using its parallel capture interface and direct memory access (DMA) controller to minimize processor overhead. Once an imaging frame was received by the MCU, it was written in raw format into incremental memory blocks of the microSD card together with a footer containing timing and error flag information. Wire-free miniscope data were recorded at 20 frames per second at a resolution of 320 pixels by 320 pixels using × 2-pixel subsampling. Running at this data rate, the entire system consumed approximately 300 mW of power during recording.

2.4 Custom imaging in water maze

Wire-free scope was coated with a polymer (Key Polimer, Tough-Seal^{tm} 21) that insulated its printed electrical boards (PCBs). The compound was applied with an applicator gun on electrically exposed parts of the PCB. The polymer was viscous at first and then cured into a rubbery form for long-term durability. 3 Mylar Helium balloons (round 18" in diameter) were used to reduce the weight load on the animal's head to avoid sinking. The balloons were filled with Helium (2HE) gas. Then the balloons were attached to the wire-free scope using cords onto a custom metal holder attached to the body of the scope. During each day of imaging the miniscope was kept on the head of the animal until the completion of the training or probe sessions. This was done to avoid movements in the imaged field of view. The miniscope was removed at the end of each day.

2.5 Morris water maze

Imaging sessions in the MWM were conducted within a circular maze (120 cm in diameter) filled with water mixed with nontoxic white paint. The maze featured a submerged platform (10 cm in diameter) located in the northeast quadrant, with 8 fixed starting points randomly chosen for each trial.

13-week-old animals underwent imaging sessions every other day, amounting to a total of six training sessions. Each day comprised of 3 blocks, separated by 90 minutes, with 4 consecutive trials in each block. In each trial, the animals were allotted 60 seconds to locate the submerged platform. If unsuccessful, the trial was terminated at 60 seconds, and the animals were placed on the platform for 10 seconds between trials to facilitate learning. Animals started each trial with their backs turned to the maze to prevent observation of their previous location.

Two probe trials were conducted at the end of training on both day 3 and day 6, with each probe occurring one hour after the conclusion of the last block on the respective day. During probes, the platform was removed, allowing animals to search freely for 60 seconds.

Following the day 6 probe, up to two additional blocks of 12 trials were added to extend the recording time, making it comparable to the length of day 1. These blocks were separated by 90-minute intervals to allow for rest.

2.6 Behavioral tracking

We designed a stereo camera system for recording maze behavior from diagonal angles using monochrome CMOS cameras (Chameleon 3, Flir) equipped with magnifying lenses (Computar). An Arduino, generating a 20 Hz TTL signal, facilitated camera synchronization and frame rate alignment with the wire-free miniscope. SpinView 1.13.0.33 software controlled the cameras and saved videos in .AVI format.

Video processing was conducted in `MATLAB` (Mathworks, Natick, MA), employing custom-

written code. The code identified dark pixels representing the mouse in the white water of the maze, allowing us to determine each joint's mouse position from each camera view. Combining these views enabled the derivation of 3D positions. We used a 4 × 6 checkerboard with a 4.5 × 4.5 mm square size for mouse tracking video camera calibration. We then used a rotation matrix (Euler quaternions) to make the 3D positions flat on the Z-axis, as the 3D coordinates calculated by the calibration algorithm are perpendicular to the diagonal axis of the cameras. Hence, we generated the trajectory of the animal as though it were recorded from an overhead perspective. Subsequently, we normalized the x and y axes to precisely match the 60 cm radius of the maze.

The head-direction was calculated by determining the absolute values of distance traveled in the x and y axes at time points t and t+1. The calculated angles of the head-direction (Θ_t) were obtained using the following formulas:

$$\Theta_t = tan\left(\frac{y_{t+1} - y_t}{x_{t+1} - x_t}\right), \qquad x \geq 0, y \geq 0; \tag{2.1}$$

$$\Theta_t = tan\left(\frac{y_{t+1} - y_t}{x_{t+1} - x_t}\right) + \pi, \qquad x > 0, y < 0; \tag{2.2}$$

$$\Theta_t = tan\left(\frac{y_{t+1} - y_t}{x_{t+1} - x_t}\right) + \pi, \qquad x < 0, y > 0; \tag{2.3}$$

$$\Theta_t = tan\left(\frac{y_{t+1} - y_t}{x_{t+1} - x_t}\right) + 2\pi, \qquad x < 0, y < 0. \tag{2.4}$$

The animal's head-direction corresponds to its heading direction while swimming in water, as the head remains consistently parallel to the swimming direction.

2.7 Calcium imaging analysis

The wire-free miniscope data were retrieved from microSD cards and stored as uncompressed 8-bit AVI video files for subsequent processing and analysis. Each day's imaging data from the MWM training blocks were aligned and concatenated into a single video file. The NoRMCorre algorithm, incorporating non-rigid registration, corrected for frame-to-frame translational shifts in the brain caused by animal movement [PG17].

For the identification and extraction of spatial shapes and fluorescent calcium activity of individual neurons, the Constrained Non-negative Matrix Factorization for endoscopic recordings (CNMF-E) method was employed [ZRR18]. Fast online deconvolution for calcium imaging using the `OASIS toolbox` was applied to deconvolve the fluorescent activity from each neuron with an AR1-constrained model [FZP17].

The resulting measure represents the probability of a neuron being active at each frame, scaled by a constant. To address the scaling factor that varies across cells, each frame was binarized, considering it as active (1) if the number was above zero and inactive (0) otherwise. This binarization step was specifically employed for Generalized Linear Model (GLM) analysis. For neural network decoding, raw calcium traces were utilized.

2.8 Tracking the same cells across days

To consistently track the same neurons across multiple days of calcium imaging, we utilized the CellReg package developed by Sheintuch et al. (2017) [SRB17] (https://github.com/zivlab/CellReg). The spatial footprints of neurons recorded on each day were input into the CellReg GUI. The package computed a probabilistic model based on spatial correlations and centroid distances of the spatial footprints, estimating the likelihood that these footprints originated from the same cell across days.

For each animal, the CellReg GUI generated a probability distribution of the nearest neighbors suspected to be the same cells across days. This distribution was plotted according to centroid distance and spatial correlation grade. Similarly, another distribution was created for the second nearest neighbors, representing cells not suspected to be the same across days. The cutoff values for the maximal centroid distance and the lowest spatial correlation grade to consider cells as the same was set at the intersection of these two distributions. This approach aimed to minimize false positives. Although these cutoff values varied slightly between animals, animals with significant overlap between the two distributions were excluded from the analysis.

CellReg provided a mapping of all registered cells to their indices on each day, organized in a matrix of size N (registered cells) x M (imaging days). This matrix facilitated the tracking of the activity of the same cells across different recording days.

2.9 Slice preparation

Hippocampal slices were obtained from the dorsal third of the hippocampus of 2- to 3-month-old male GluA1^{C2KI} B6129SF2 hybrid mice and their respective littermate controls. Mice were deeply anesthetized with isoflurane, and following cervical dislocation, the brain was promptly removed and placed in cold (4°C), oxygenated (95% O2/5% CO2) artificial cerebrospinal fluid (ACSF). The ACSF composition included 124 mM NaCl, 4 mM KCl, 25 mM NaHCO3, 1 mM NaH2PO4, 2 mM CaCl2, 1.2 mM MgSO4, and 10 mM glucose (all obtained from Sigma-Aldrich).

Subsequently, both hippocampi were dissected from the brain, and a manual tissue slicer was employed to create 400-µm-thick slices. The CA3 region was removed, and the slices were transferred to interface-type chambers with continuous perfusion of ACSF (2-3 ml/min). The slices were allowed to recover at 30°C for a minimum of 2 hours before commencing recordings.

2.10 Electrophysiological slice recordings

Extracellular recordings were done using slices maintained in interface-type recording chambers perfused (2-3 ml/min) with ACSF. Two bipolar, stimulating electrodes fabricated from twisted strands of Formvar-insulated nichrome wire (A-M Systems) were placed in stratum radiatum to activate Schaffer collateral/commissural fiber synapses onto CA1 pyramidal cells (basal stimulation rate = 0.02 Hz). Field EPSPs (fEPSPs) were recorded in stratum radiatum using low-resistance (5-10 MW) glass microelectrodes filled with ACSF and a Multi-clamp 700B amplifier (Molecular Devices). Signals were low pass filtered with a cutoff frequency of 2 kHz and digitized at 10 kHz. After determining the maximal amplitude of fEPSPs evoked by presynaptic fiber stimulation,

the stimulation intensity was adjusted to evoke fEPSPs with an amplitude 50% of the maximal amplitude. Independence of the presynaptic axons activated by the two stimulating electrodes (hereafter referred to as S1 and S2) was confirmed by the absence of paired-pulse facilitation when pulses of presynaptic fiber stimulation were delivered to S1 and then S2 (and vice-versa) with an inter-pulse interval of 50 ms.

2.11 Slice recording experimental design and statistical analyses

CS burst-dependent LTP was induced using trains of theta-pulse stimulation (TPS) that consisted of single pulses of presynaptic fiber stimulation delivered at 5 Hz. Average slopes of fEPSPs (normalized to baseline) recorded 40-45 min after TPS were used for statistical comparisons. Data were collected and analyzed using pClamp10 software (Molecular Devices).

2.12 Exploring spatial and head-directional modulations: GLM approach

We modeled the time-varying calcium event activities as an inhomogeneous Poisson process with a time-varying rate $r(t)$. For an inhomogeneous Poisson process, the number of events in any interval is a Poisson random variable. We defined time-varying rate function, denoted as $r(t)$ as follows:

$$r(t) = \frac{r_S(t) r_{HD}(t) r_{base}}{\tau}, \tag{2.5}$$

where τ is the time bin size (we chose 100 ms) and r_{base} is a constant term and related to the baseline activity of a neuron. $r_S(t)$ and $r_{HD}(t)$ are intensity functions for space and head-direction,

respectively, and are defined as follows:

$$r_S(t) = e^{A_S \alpha_S} = \exp\left(\sum_{i=1}^{Q} \sum_{m=-q}^{q} c_{q,m} z_q^m(\rho(t), \psi(t))\right) \tag{2.6}$$

$$r_{HD}(t) = e^{A_{HD} \alpha_{HD}} = \exp\left(\sum_{j=1}^{J} c_j sin(j\phi(t)) + c'_j cos(j\phi(t))\right) \tag{2.7}$$

$$r_{base} = e^{\alpha_0}. \tag{2.8}$$

A_S and A_{HD} are design matrices for space and head-direction, respectively. Following Acharya's approach [AAV16], we modeled the spatial and head-directional intensity function by initially employing a linear function on the expanded behavioral covariates. Subsequently, this linear model underwent further processing through a nonlinear exponential function. In other words, we initially expanded the behavioral covariates using a set of defined functions. Specifically, we expanded space using a set of orthogonal two-dimensional Zernike polynomials (Figure 2.1), and head-direction was expanded using a set of sine and cosine functions (Figure 2.2). Next, we subjected them to a linear function, followed by a nonlinear link function, namely an exponential function, denoted as e^x.

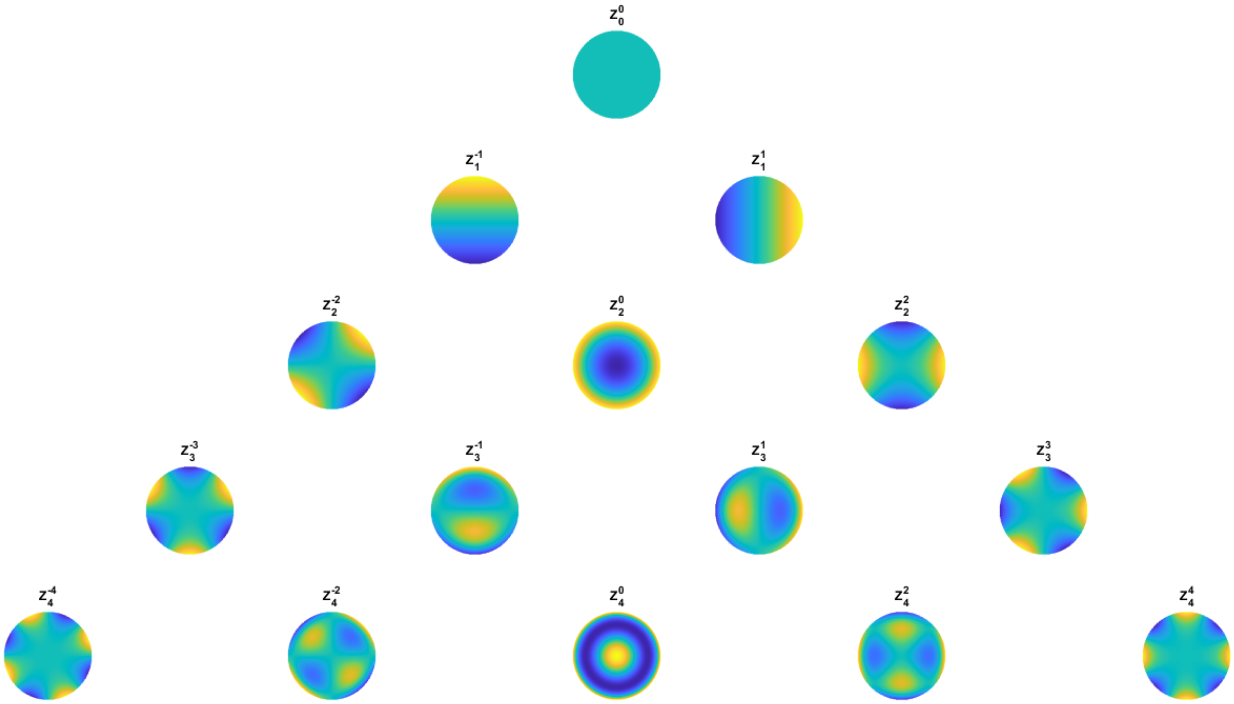

Figure 2.1: EXAMPLE REPRESENTATION OF ZERNIKE POLYNOMIALS
Display the first 15 Zernike functions: $z_l^m, l = [0, 1, 2, 3, 4], m = [-l, ..., l]$.

In Equation 2.6 and 2.7, α_S and α_{HD} are the parameters associated with the design matrices A_S and A_{HD}, respectively and in Equation 2.8, α_0 is a constant term. The notation z_q^m in Equation 2.6 signifies the m-th component of the q-th order Zernike polynomial function. The radial and angular components of position in polar coordinates at time t are represented by $\rho(t)$ and $\psi(t)$, respectively. Hence, A_S is $[n, s]$ matrix, where n = number of time bins and s = number of Zernike polynomials. In Figure 2.1 we have shown the first 15 two-dimensional Zernike functions. The first Zernike function z_0^0 is constant. In Equation 2.7, $\phi(t)$ is the head-direction of the animal at time t and $sin(j\phi(t))$ and $cos(j\phi(t))$ are orthogonal basis functions to expand the head-direction covariate. Hence, A_{HD} is $[n, h]$ matrix, where n = number of time bins and h = number of sin and cos functions. In Figure 2.2 5 examples of $sin(k\theta)$ and $cos(k\theta)$ functions are illustrated, where various frequencies are represented by k values in the range of 1 to 5.

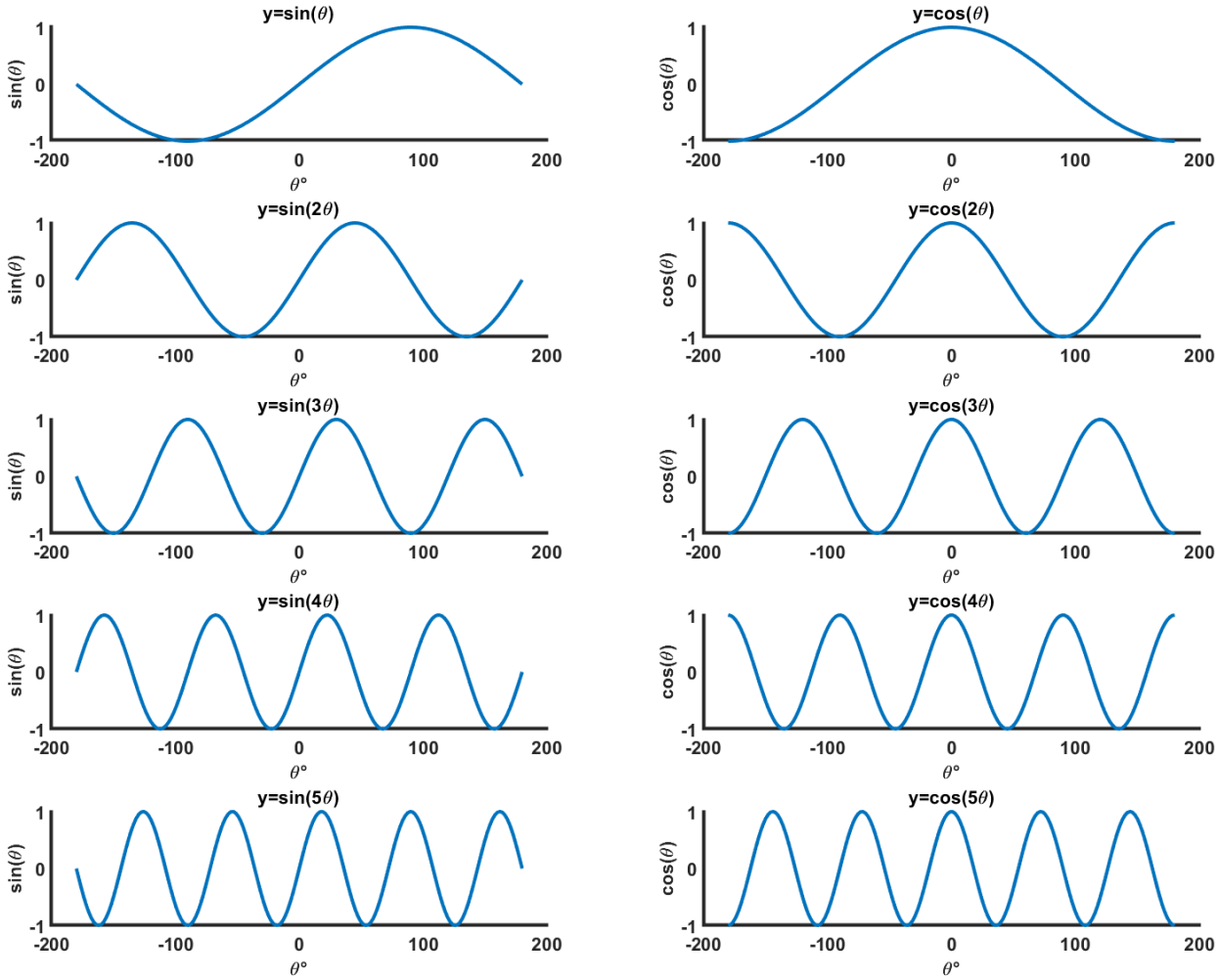

Figure 2.2: EXAMPLE REPRESENTATION OF SIN(θ) AND COS(θ)
Display of $\sin(k\theta)$ and $\cos(k\theta)$ functions, $k = [1, 2, 3, 4, 5]$.

To estimate the parameters in Equations 2.6–2.8, specifically α_S, α_{HD}, and α_0, we employed the `glmfit` function in `MATLAB`. This function utilizes maximum likelihood estimation through the standard iteratively reweighted least squares (IRLS) algorithm. Moreover, we used the Akaike Information Criterion (AIC) for model selection to determine the best number of basis functions for both space and head-direction. The AIC quantifies the trade-off between the goodness of fit of a statistical model and the complexity of the model by using the following equation:

$$AIC = 2k - 2ln(\hat{L}), \tag{2.9}$$

where $\hat{L}$ is the maximum likelihood for the model, and k is the number of parameters in the model. In our model

$$k = N_{Zernikefunctions} + N_{sinfuntions} + N_{cosfuntions} + 1. \tag{2.10}$$

To reconstruct the spatial and head-directional rate maps as a function of the position and head angle of an animal we used the following equations:

$$\lambda_S(x_i, y_i) = \exp\left(\sum_{i=1}^{Q}\sum_{m=-q}^{q} c_{q,m} z_q^m(x_i, y_i)\right) \tag{2.11}$$

$$\lambda_{HD}(\phi_p) = \exp\left(\sum_{j=1}^{J} c_j sin(j\phi_p) + c'_j cos(j\phi_p)\right), \tag{2.12}$$

where x_i and y_i represent the position of the i-th spatial bin and ϕ_p denotes the p-th head-direction bin. We used 4×4 cm^2 spatial bins and 3° angular bins. Furthermore, to obtain an unbiased rate map that is compatible with the mean firing activity of the neuron, we employed the following equation to predict the spatial and angular modulations:

$$\kappa_S = \overline{\lambda} \times \frac{\lambda_S(x, y)}{\overline{\lambda_S}} \tag{2.13}$$

$$\kappa_{HD} = \overline{\lambda} \times \frac{\lambda_{HD}(\phi)}{\overline{\lambda_{HD}}} \tag{2.14}$$

$$\overline{\lambda} = \text{mean firing rate of the neuron,} \tag{2.15}$$

where $\overline{\lambda_S}$ and $\overline{\lambda_{HD}}$ are the mean values of $\lambda_S(x, y)$ and $\lambda_{HD}(\phi)$, respectively.

2.13 Validation of GLM with synthetic data

To demonstrate the effectiveness of GLM in accurately estimating spatial and head-directional modulation in our data, we generated a synthetic cell with surrogate spike trains (Figure 2.3). The generation of surrogate spikes involved the following steps:

1- Define a synthetic spatial rate map, $\lambda_{synthS}(x, y)$, as a 2D Gaussian function (Equation 2.16). The peak of the spatial rate map is located at (x_0, y_0), and σ_X and σ_Y represent the spatial variances.
2- Define a synthetic angular rate map, $\lambda_{synthHD}(\theta)$, as a 1D Gaussian function (Equation 2.17). The peak of the angular rate map is at (θ_0), and σ_θ is the angular variance.
3- Define the rate function of the neuron with the mean firing activity μ as Equations 2.18 and 2.19. It's important to emphasize that we modeled the influences of spatial and head-directional covariates as independent variables.
4- Generate a time-varying rate function (Equation 2.20) by incorporating the empirical behavior of an animal and the rate map defined in Equation 2.18.
5- Generate synthetic spike trains (Equation 2.21) by employing a nonhomogeneous Poisson process with the rate function defined in Equation 2.20.

$$\lambda_{synthS}(x, y) = A \exp\left(-\left(\frac{(x - x_0)^2}{2\sigma_X^2} + \frac{(y - y_0)^2}{2\sigma_Y^2}\right)\right) + A_0 \tag{2.16}$$

$$\lambda_{synthHD}(\theta) = B \exp\left(-\frac{(\theta - \theta_0)^2}{2\sigma_\theta^2}\right) + B_0 \tag{2.17}$$

$$\lambda_{synth}(x, y, \theta) = c \times \lambda_{synthS}(x, y) \times \lambda_{synthHD}(\theta) \tag{2.18}$$

$$c = \frac{\mu}{< \lambda_{synthS}(x, y) \times \lambda_{synthHD}(\theta) >} \tag{2.19}$$

$$r(t) = \lambda_{synth}(x(t), y(t), \theta(t)) \tag{2.20}$$

$$P(N_{spike}(t + \Delta t) - N_{spike}(t) = n) = \frac{(r(t)\Delta t)^n}{n!} e^{-\int_t^{t+\Delta t} r(s)\, ds}. \tag{2.21}$$

Figure 2.3 illustrates the synthetic cell and its predicted spatial and head-directional rate maps using GLM. We employed a pre-defined 2D and 1D Gaussian functions for the spatial and head-directional modulations, respectively (Figure 2.3 (a and b)). To acquire synthetic behavioral data, we utilized the empirical behavior that we recorded in one of our sessions. Utilizing the synthetic behavior and synthetic rate maps, we derived the time-varying rate function. This function was then employed as the rate parameter in the nonhomogeneous Poisson process, allowing us to

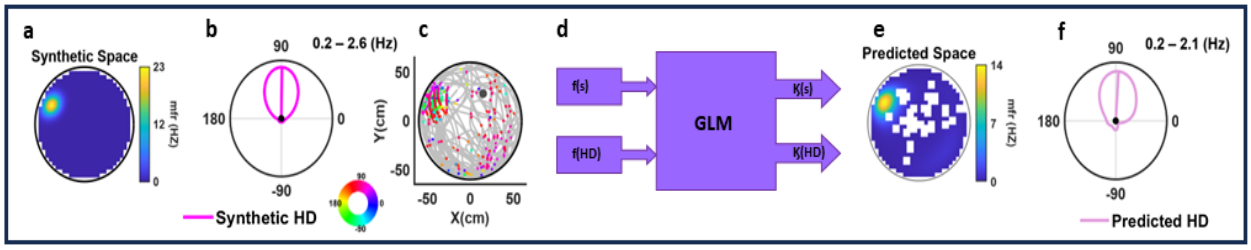

Figure 2.3: VALIDATION OF GENERALIZED LINEAR MODELS THROUGH SYNTHETIC CELLS
(a,b) We utilized synthetic spatial and head-directional rate maps to generate the spike trains. **(c)** Synthetic spike trains were generated using the spatial and head-directional rate maps from (a) and (b), combined with empirical behavior and a non-homogeneous Poisson process. Each dot represents a spike, with the color indicating the head-direction of the animal at the time of the spike. **(d)** Schematic of the GLM framework. To predict the spatial and head-directional rate maps, we utilized the spike trains and behavioral covariates, namely position and head-direction. **(e,f)** The predicted spatial and head-directional rate maps align closely with their synthetic counterparts.

generate the synthetic spike train (Figure 2.3 (c)). Next, we employed the GLM (Figure 2.3 (d)) to predict the spatial and head-directional rate maps shown in Figure 2.3 (e,f). The synthetic spatial and head-directional rate maps demonstrate a distinct similarity to their respective predicted counterparts.

2.14 Measure of selectivity for the spatial and head-directional rate map

One commonly used metric for quantifying the degree of selectivity in a rate map is the sparsity (S) which is defined as follows:

$$S = 1 - \frac{1}{N}\frac{(\sum_n^N r_n)^2}{\sum_n^N r_n^2}, \tag{2.22}$$

where N represents the total number of bins, such as spatial or angular bins, and, r_n denotes the firing rate in the i-th bin. The sparsity is a dimensionless metric, providing insight into the selectivity of a neuron's firing across various conditions, such as positions. The sparsity ranges from 0 to 1, with a higher value indicating greater selectivity.

2.15 Shuffling method

To facilitate data shuffling for the GLM analysis, we individually performed circular shuffling for each variable while maintaining the other variable unchanged. For instance, in computing the shuffled sparsity for the position, we circularly flipped the position signal and then applied circular shifts with random numbers 50 times, keeping the head-direction signal unchanged. Subsequently, we computed the spatial sparsity for each set of shuffled data. For the decoding analysis, we performed separate shuffling of the neural signal ($\frac{\Delta f}{f}$) for each neuron. The process involved flipping the neural signal and then applying circular shifts with a random number 50 times.

2.16 Shuffle subtraction

To mitigate potential bias in behavior on day 6 compared to day 1 and its potential impact on sparsity and decoding error values, we subtracted the 95th percentile of the shuffled sparsity (decoding error) from the original sparsity (decoding error), as follows:

$$S_{\text{shuffle-subtracted sparsity}} = S - p(S_{\text{shuffled}}, 95) \tag{2.23}$$

$$E_{\text{shuffle-subtracted decoding error}} = E - p(E_{\text{shuffled}}, 95) \tag{2.24}$$

2.17 Feedforward neural networks

To decode position, head-direction, and the distance from the platform, we implemented three feedforward neural networks with different structures, First, we needed to preprocess the data. Figure 2.4 (a,b) illustrates the schematic for preprocessing the data, involving the following steps:

1. Divide the calcium fluorescence signal ($\frac{\Delta f}{f}$) for each neuron into 100 ms bins.
2. Take the average of the signal in each bin.
3. Divide the behavioral variable, such as position, into 100 ms bins.

4. Take the average of the behavioral variable in each bin.

5. To decode the i-th output, utilize 2k+1 bins of neural signal for each neuron, including k bins preceding the i-th bin, the concurrent i-th bin, and k bins following the i-th bin.

6. Generate the feature matrix from the neural signal and utilize it as input for the feedforward neural network (FFN). The matrix comprises M rows, representing the number of training data, and $N \times (2k + 1)$ columns. Here, N is the number of neurons, k is the number of preceding and following bins, and 1 is for the concurrent bin. For each neuron, extract the calcium fluorescence signal and gather information from the k bins preceding, the k bins following, and the concurrent bin (representing the current time step). This results in a set of $2k + 1$ bins associated with each neuron. This process is repeated for all neurons, concatenating these sets successively. This is shown in Figure 2.4 (b), and the entries are denoted by s^i_j, where s represents the value of the calcium fluorescence signal for the i-th neuron at the j-th bin.

2.18 FFN's architectures for decoding position, head-direction, and distance to the platform

The input layer consisted of $N \times (2k + 1)$ nodes, where N represents the number of neurons, $k = 10$ was the number of preceding and following bins, and 1 corresponded to the concurrent i-th bin. To decode the position, we employed a feedforward neural network with a dropout rate of 0.2 and 15 epochs. The architecture included two hidden layers, with the number of nodes in each hidden layer matching the number of nodes in the input layer. The output layer was composed of two nodes representing the x and y coordinates of the animal's position at the i-th bin (Figure 2.5). For head-direction decoding, a dropout rate of 0.2 and 10 epochs were applied, utilizing a single hidden layer with node count equal to that of the input layer. The output layer comprised two nodes representing $sin(\theta)$ and $cos(\theta)$, where θ denotes the animal's head-direction at the i-th bin (Figure

2.6). To decode the distance to the platform, we employed a dropout rate of 0.2 over 15 epochs, using a single hidden layer with a node count matching that of the input layer. The output layer consisted of two nodes representing the distance to the platform. (Figure 2.7).

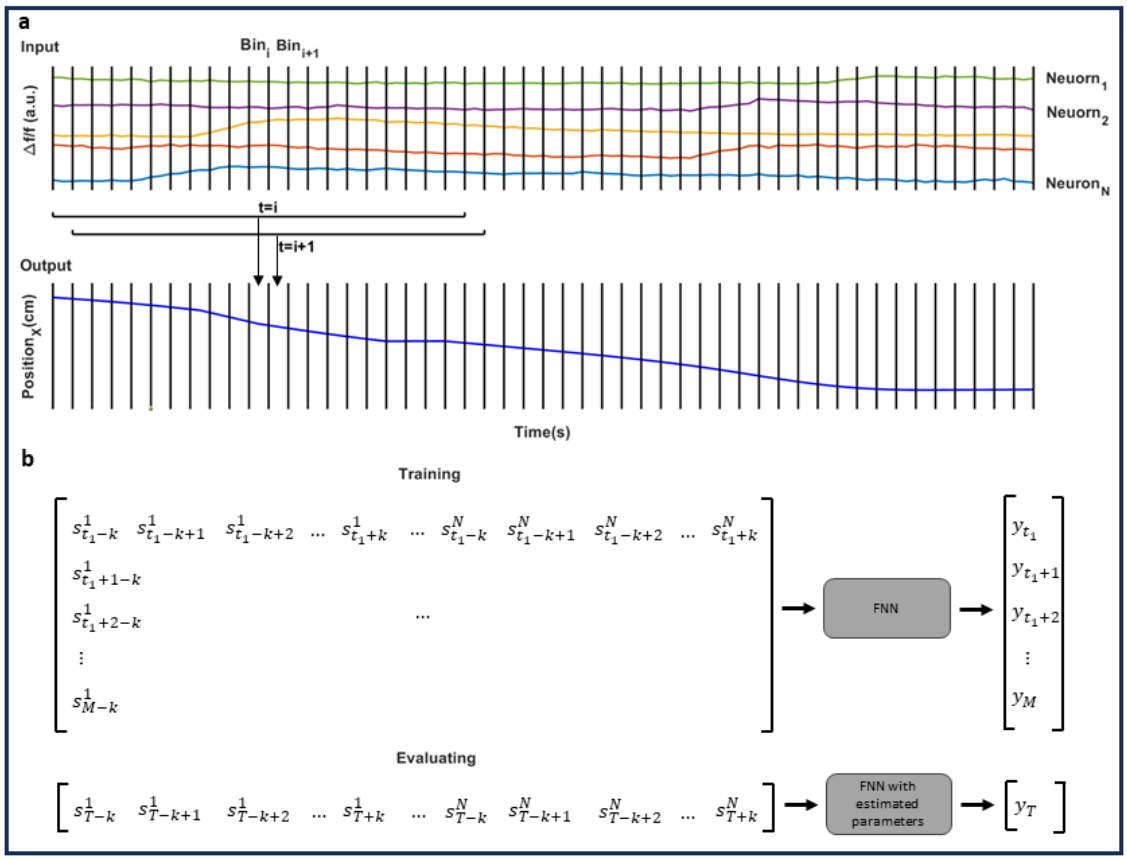

Figure 2.4: SCHEMATIC FOR PREPROCESSING DATA IN PREPARATION FOR FEEDFORWARD NEURAL NETWORK

(a) The calcium fluorescence signal of each neuron was segmented into bins of 100 ms. Simultaneously, the output variable, such as the position of the animal, was also binned into 100 ms intervals. To decode an output at the i-th bin, we employed information from k bins preceding the output, the concurrent i-th bin, and k bins following the i-th output. **(b)** The input (features) and output matrices were provided to the feedforward neural network (FFN) for training. Once the network was trained, and its parameters were estimated, for model evaluation, an input was given to predict the corresponding output.

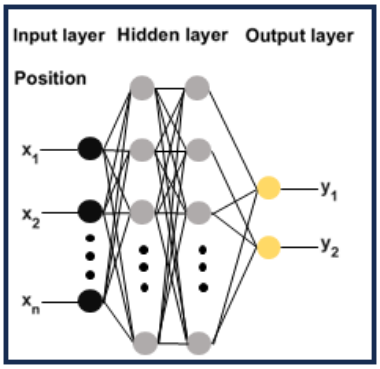

Figure 2.5: SCHEMATIC OF A FEEDFORWARD NEURAL NETWORK FOR DECODING POSITION

The input layer had $N \times (2k + 1)$ nodes, where N represented the number of neurons, $k = 10$ indicated the number of preceding and following bins, and 1 corresponded to the concurrent i-th bin. It also had two hidden layers with the number of nodes in each hidden layer equal to the number of nodes in the input layer. Additionally, parameters such as drop-out rate=0.2 and the number of epochs=15 were employed in the model. The output layer consisted of two nodes representing the x and y coordinates of the animal's position at the i-th bin.

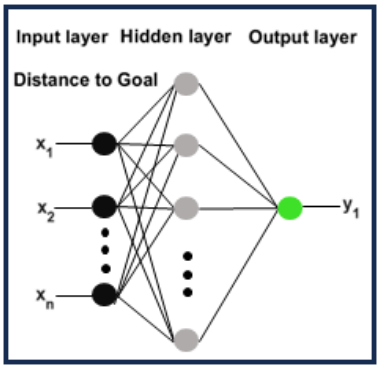

Figure 2.7: SCHEMATIC OF A FEEDFORWARD NEURAL NETWORK FOR DECODING DISTANCE TO THE PLATFORM

The input layer had $N \times (2k + 1)$ nodes, where N represented the number of neurons, $k = 10$ indicated the number of preceding and following bins, and 1 corresponded to the concurrent i-th bin. It also had one hidden layer with the number of nodes in the hidden layer equal to the number of nodes in the input layer. Additionally, parameters such as drop-out rate=0.2 and the number of epochs=15 were employed in the model. The output layer consisted of one node representing the animal's distance to the platform at the i-th bin.

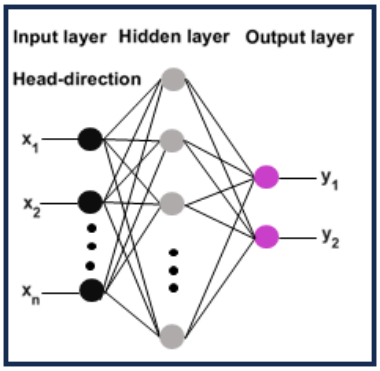

Figure 2.6: SCHEMATIC OF A FEEDFORWARD NEURAL NETWORK FOR DECODING HEAD-DIRECTION
The input layer had $N \times (2k + 1)$ nodes, where N represented the number of neurons, $k = 10$ indicated the number of preceding and following bins, and 1 corresponded to the concurrent i-th bin. It also had one hidden layer with the number of nodes in the hidden layer equal to the number of nodes in the input layer. Additionally, parameters such as drop-out rate=0.2 and the number of epochs=10 were employed in the model. The output layer consisted of two nodes representing the $sin(\theta)$ and $cos(\theta)$, where θ is the animal's head-direction at the i-th bin.

2.19 Decoding performance metrics

To quantify the improvement in the decoder's performance attributable to the animals' learning in the MWM task, and consequently, the increased information in the recorded neural signals, we computed the position decoding error using the following formula:

$$E_S = \frac{\sum_{i=1}^{L} \sqrt{(x^i - \hat{x}^i)^2 + (y^i - \hat{y}^i)^2}}{L}, \tag{2.25}$$

where x^i and $\hat{x}^i$ are the original and decoded x coordinates at the i-th bin, respectively. Similarly, y^i and $\hat{y}^i$ are the original and decoded y coordinates at the i-th bin, respectively. L is the size of the testing data set.

We employed 2D correlation as an additional metric to assess the performance of position decoding. We calculated the 2D correlation between the original coordinates $A = [X, Y]$ and the decoded coordinates $B = [\hat{X}, \hat{Y}]$ using the following formula:

$$R_S = \frac{\sum_{i=1}^{m} \sum_{j=1}^{n} (A(i,j) - \bar{A})(B(i,j) - \bar{B})}{\sqrt{\sum_{i=1}^{m} \sum_{j=1}^{n} (A(i,j) - \bar{A})^2 \sum_{i=1}^{m} \sum_{j=1}^{n} (B(i,j) - \bar{B})^2}}, \tag{2.26}$$

where m represents the number of rows, n is the number of columns, $A(i, j)$ and $B(i, j)$ denote the elements at the i-th and j-th columns of matrices A and B, respectively. The terms $\overline{A}$ and $\overline{B}$ are the means of matrices A and B, respectively.

The decoded errors for head-direction and distance to the goal were computed as follows:

$$E_{HD} = \frac{\sum_{i=1}^{L}(\theta^i - \hat{\theta}^i)}{L}, \tag{2.27}$$

where θ^i and $\hat{\theta}^i$ are the original and decoded head-direction at the i-th bin, respectively.

$$E_D = \frac{\sum_{i=1}^{L}(d^i - \hat{d}^i)}{L}, \tag{2.28}$$

where d^i and $\hat{d}^i$ are the original and decoded distance to the platform at the i-th bin, respectively.

CHAPTER 3

Results

This section will comprehensively present and delve into the detailed results obtained from this study, offering a thorough analysis and discussion of the findings.

3.1 Behavioral changes during learning the Morris water maze task

We recorded ten 13-week-old mice while they performed the MWM spatial navigation task. In preparation for calcium imaging, all mice underwent a stereotaxic surgery. Initially, mice received a unilateral injection of AAV1.Syn.jGCaMP7f.WPRE virus. Subsequently, they underwent GRIN lens implantation surgery. After a 20-day recovery period, the mice were anesthetized once again to facilitate the placement of a miniature microscope on an aluminum baseplate, positioned atop the GRIN lens. The procedure involved guiding the baseplate onto the skull surface using the miniscope, ensuring optimal field of view identification for the mice. Following a two-day recovery, we initiated training sessions for the MWM task, simultaneously imaging neural activities in the CA1 region (Figure 3.1 (a-c)).

The MWM task is a behavioral test designed to assess spatial memory in animals. The task consists of a circular pool, measuring 120 cm in diameter, filled with opaque water, and featuring a concealed platform just beneath the water's surface. The goal of the task is to assess the animal's ability to learn and remember the location of the hidden platform, utilizing distal cues positioned on the surrounding walls (Figure 3.2). Experiments took place over six recording days, with data collection occurring every other day for each animal. Each recording day was divided into 3 blocks,

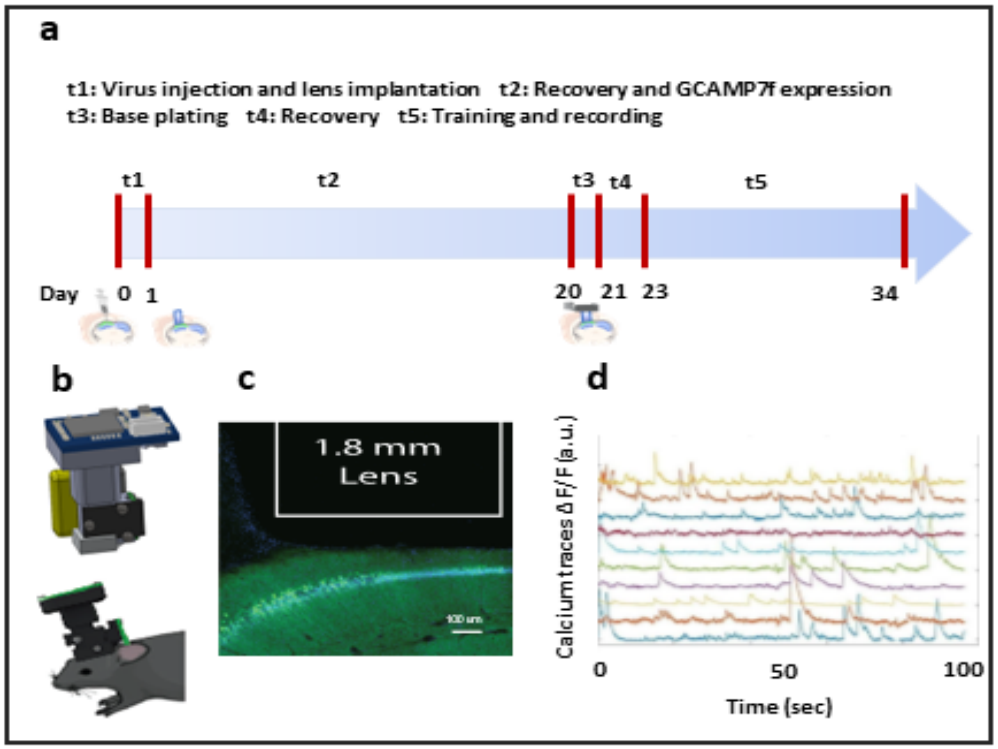

Figure 3.1: OVERVIEW OF EXPERIMENTAL PROCEDURES
(a) Chronology of surgical procedures and MWM training. **(b)** Miniscope schematic positioned on a mouse head. **(c)** Hippocampus slice with GRINLens placement, indicating recorded neuron positions. **(d)** Calcium transient signals for selected sample cells.

each consisting of 4 consecutive trials. The duration of each trial was limited to a maximum of 60 seconds or until the animal successfully located the hidden platform. If a trial was unsuccessful within the allotted 60 seconds, the session was concluded, and the animal was positioned on the platform for a 10-second interval between trials to enhance learning. To ensure unbiased navigation and eliminate the influence of prior knowledge regarding the platform's location, each trial commenced with the animal facing away from the maze. This strategic starting position aimed to prevent them from observing their prior locations, discouraging the use of the fastest trajectory based on familiarity with the platform's position.

During the trials in the MWM, we simultaneously measured the calcium transient activity of CA1 neurons (Figure 3.1 (d)), along with tracking the position and head-direction of the animals as they navigated through the water maze. As the animals acquired proficiency in the task, the

time required to reach the platform decreased in each trial, leading to shorter recorded times in subsequent sessions. Acknowledging the potential impact of recording duration on the analysis and results, we incorporated additional trials on day 6 to maintain comparable recording durations for both day 1 and day 6. Hence, after completing the probe trials on day 6, we conducted extra trials, involving 0–2 blocks, with each block consisting of 12 trials.

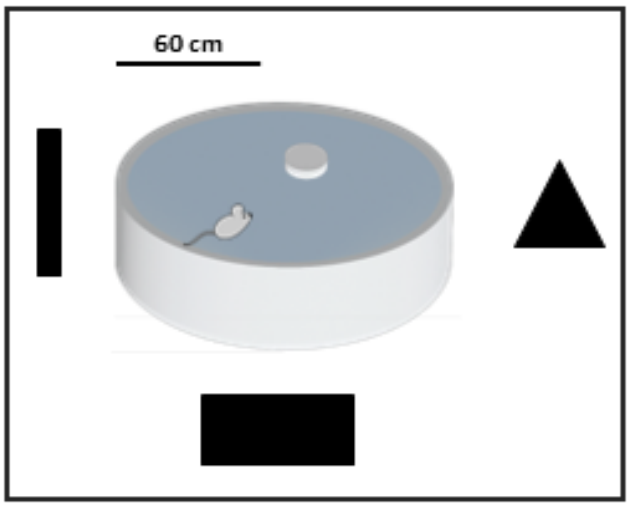

Figure 3.2: SCHEMATIC OF MORRIS WATER MAZE
MWM is a circular pool with a diameter of 120 cm, filled with opaque water. The hidden platform is depicted in grey within the northeast quadrant. Distal geometric shapes on the surrounding walls serve as distal visual cues for navigation.

Throughout the training process, animals learned to locate a hidden platform submerged just beneath the water's surface, utilizing distal visual cues on the walls as their navigational guides. On the first day of the training, the subjects were unfamiliar with the location of the hidden platform, indicated by the grey circle in Figure 3.3 (a_1–a_6), and its positioning in relation to the distal visual cues on the wall. This led them to explore various areas within the pool, often taking longer paths in their attempts to locate the platform (Figure 3.3 (a_1–a_6) and Figure 3.4 (a)). Throughout training, as the animals utilized the distal cues in the surrounding environment to navigate and learn the platform's location, they began to take shorter paths (Figure 3.3 (a_1–a_6)), resulting in reduced time to complete the task (Figure 3.4 (a)) and spending more time in vicinity of the hidden platform (Figure 3.3 (a_6)). As it is also shown in Figure 3.3 (b_1–b_6) the animal's preferred head angle tended

to shift towards the northeast, aligning with the location of the hidden platform.

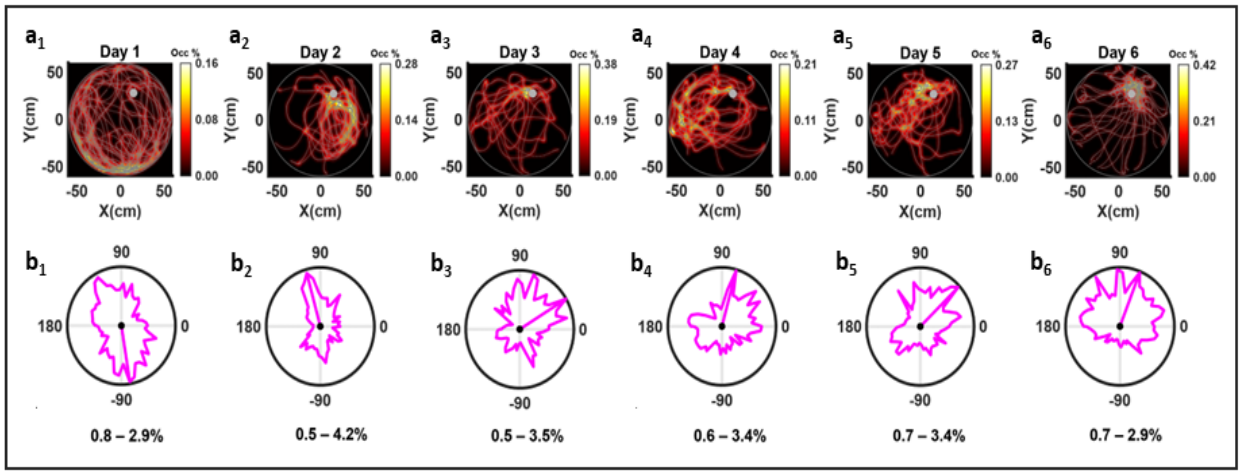

Figure 3.3: SPACE AND HEAD-DIRECTION OCCUPANCY
(a_1) On day 1 the animal explored various locations due to its unfamiliarity with the hidden platform's location. **(a_5–a_6)** As the animal acquired proficiency in the task, it adopted a more direct route to the platform and dedicated more time to its vicinity. **(b_1–b_6)** With growing expertise in the task, its preferred head-direction gradually oriented towards the northeast, indicating they learned where the hidden platform was located. The numerical values at the bottom of each polar plot indicate the range of head-direction occupancy in each day.

3.2 Neural firing activity changes during learning the Morris water maze task

The escape latency in the Morris Water Maze (MWM) signifies the duration it takes for an animal to locate and reach a hidden platform within the maze, serving as a metric for evaluating spatial learning and memory in rodents. In line with expectations, our findings demonstrated a consistent reduction in escape latency as animals progressed in learning the MWM task. During the initial trials, particularly on the first day, the animals exhibited a prolonged escape latency, reflecting their unfamiliarity with the maze. However, as the animals gained experience with the task, they progressively acquired the ability to learn and retain spatial cues guiding them to the platform's location. This acquired knowledge subsequently led to a significant decrease in escape latency

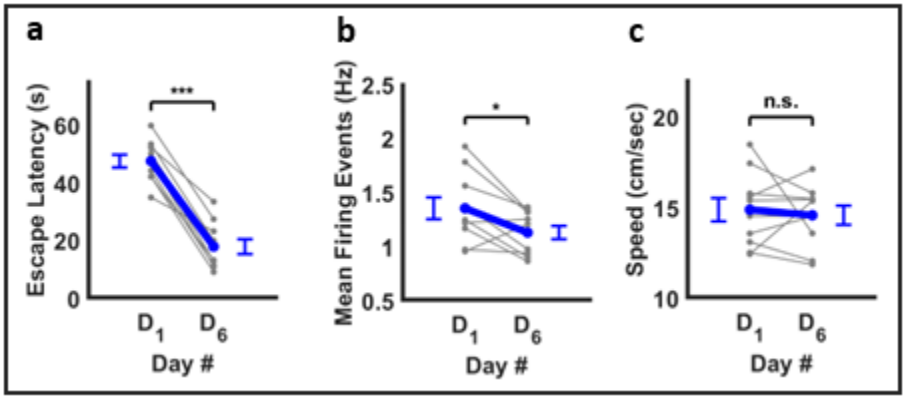

Figure 3.4: REDUCTION IN ESCAPE LATENCY AND AVERAGE FIRING ACTIVITY As the animal learned the task, two notable changes were observed: **(a)** Significant reduction in escape latency (day 1: 47.6 ± 2.2 s, day 6: 18.0 ± 2.6 s, paired sample t-test, $n = 10$, p= 9.96×10^{-7}) and **(b)** slight but significant reduction in mean firing activity (day 1: 1.36 ± 0.10 Hz, day 6: 1.13 ± 0.06 Hz, paired sample t-test, p= 0.0203). **(c)** The speed of the animal on day 1 is not significantly different than the speed on day 6 (day 1: 14.89 ± 0.65 cm/s, day 6: 14.58 ± 0.53 cm/s, paired sample t-test, p= 0.6527). '*' p< 0.05, '**' p< 0.005, '***' p< 0.0005.

over subsequent trials (Figure 3.4 (a), day 1: 47.6 ± 2.2 s, day 6: 18.0 ± 2.6 s, p= 9.96×10^{-7}). As the animals learned the task, mean calcium event frequency also decreased (Figure 3.4 (b), day 1: 1.4 ± 0.10 Hz, day 6: 1.1 ± 0.06 Hz, p= 0.0203). There was no statistically significant difference in the average speed of animals on both day 1 and day 6 of the experiment (Figure 3.4 (c), day 1: 14.9 ± 0.65 cm/s, day 6: 14.6 ± 0.53 cm/s, p= 0.6527).

3.3 Probe analysis

We conducted two probe trials as part of our study: the first occurred one hour after the conclusion of training in day 3, and the second took place one hour following the conclusion of day 6. Throughout the probe trial, the platform was removed, and the animals were allowed to swim freely in the pool for 60 seconds.

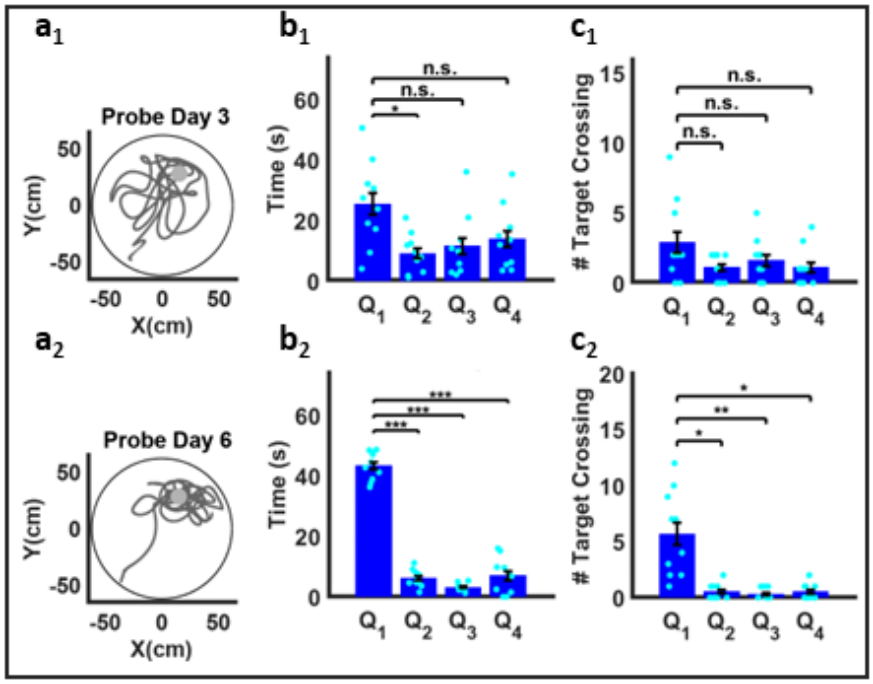

Figure 3.5: IMPROVED PERFORMANCE IN PROBE TRIALS
(a_1, a_2) Animal's trajectory during the first and second probe after day 3 and day 6. respectively. **(b_1, b_2)** During the probe trial after day 6, animals exhibited a prolonged presence in the vicinity where the hidden platform was located during training, in contrast to the probe after day 3 (day 1: repeated measures ANOVA, n=10, F(3,27)= 3.48, p= 0.0294. Planned comparisons paired t-test (Q_1, Q_2): = 0101, (Q_1, Q_3): = 0.0889, (Q_1, Q_4): = 0.1155; day 6: repeated measures ANOVA, F(3,27)= 165.82, p= 1.68×10^{-7}. Planned comparisons paired t-test (Q_1, Q_2)= 1.12×10^{-9}, (Q_1, Q_3)= 1.36×10^{-9}, (Q_1, Q_4)= 1.14×10^{-6}). **(c_1, c_2)** The number of target crossing is significantly higher in quadrant Q_1 in contrast to the remaining quadrant (day 1: repeated measures ANOVA, F(3,27)= 1.87, p= 0.1577. Planned comparisons paired t-test (Q_1, Q_2)= 0.0642, (Q_1, Q_3)= 0.2819, (Q_1, Q_4)= 0.1678, day 6: repeated measures ANOVA, F(3,27)= 16.71, p= 2.45×10^{-6}. Planned comparisons paired t-test (Q_1, Q_2)= 0.0018, (Q_1, Q_3)= 0.0014, (Q_1, Q_4)= 0.0041). Bonferroni correction is applied. '*' p< 0.0167, '**' p< 0.0017, '***' p< 1.67×10^{-4}.

The primary objective of the probe trial was to evaluate the spatial memory of the animals and their capacity to recall the location of the hidden platform. This assessment was conducted by observing their preference for the target quadrant (northeast, Q_1), where the platform was initially positioned. We assessed two parameters: (1) the duration spent in the target quadrant (Q_1) in comparison to other quadrants (Q_3–Q_4), and (2) the number of platform crossings. The term "platform crossing" refers to instances where the animal swims over the location where the hidden

platform used to be during the training phase. A greater frequency of platform crossings typically indicates enhanced retention of spatial memory, as the animal demonstrates a preference for the area where it previously found the platform. As it is shown in (Figure 3.5 (a_1 and a_2) during the probe trial on day 6, the animals tended to stay in closer proximity to the target quadrant, where the hidden platform was initially located. Figure 3.5 (b_1 and b_2) indicate that the animal spent a statistically significant amount of time more in quadrant Q_1 compared to the other quadrants (day 1: $F(3,27)= 3.48$, $p= 0.0294$, day 6: $F(3,27)= 165.82$, $p= 1.68 \times 10^{-7}$). Moreover, there was a statistically significant increase in the number of target crossings in quadrant Q_1 in contrast to the remaining quadrants (Figure 3.5 (c_1 and c_2), day 1: $F(3,27)= 1.87$, $p= 0.1577$, day 6: $F(3,27)= 16.71$, $p= 2.45 \times 10^{-6}$). Therefore, both escape latency and probe trials demonstrated robust learning in the MWM in animals implanted with the miniscope.

3.4 Elevated spatial and head-directional selectivity through learning the MWM task

In the preceding section, we demonstrated the proficiency of our control subjects in performing the MWM task through behavioral analysis. Next, we explored the alterations in neural selectivity as the animal acquired proficiency in the task. Our aim was to investigate the impact of spatial and head-directional covariates on the firing activity of hippocampal neurons. It is crucial to acknowledge that the behavior of animals in MWM task introduced certain biases, which, when not properly accounted for, could contribute to spurious results. Moreover, we had a particular interest in concurrently estimating the spatial and head-directional modulation.

The binning method has been one of the most commonly employed techniques in neuroscience for estimating neural firing rates about various covariates. This method entails dividing the stream of neural activity into discrete intervals, or “bins”, and quantifying the number of spikes within each bin. These intervals can represent time, space, head-direction, or any other relevant covariates. To compute the neural firing rate, one would then divide the number of spikes in each bin by the

corresponding time the animal spent in that bin. Notably, behavioral biases can heavily affect the firing rate of neurons predicted by the binning method. To simultaneously and independently predict space and head-directional modulation while also accounting for behavioral biases (refer to [AAV16] for insights into how behavioral biases impact the prediction of space and head-direction modulation), we employed established Generalized Linear Models (GLM) framework ([MLE11, LME12, TEF05, AAV16]). Truccolo et al. in their seminal paper proposed a statistical framework based on a point process likelihood function, to relate a neuron's spiking probability to extrinsic covariates such as behavior ([TEF05]). Moreover, they showed that the discrete time point process likelihood function can be analyzed in the GLM framework which uses parametric models.

GLM proves to be a fitting statistical framework for our data due to several key reasons:

Flexibility: GLM is a flexible statistical framework that accommodates various types of response variables, making it suitable for modeling complex neural activity patterns observed in the hippocampus.

Nonlinearity: The hippocampal neurons often exhibit nonlinear responses to space and head-direction. GLM can capture such nonlinear relationships, allowing for a more accurate representation of the underlying neural processes.

Multiple predictors: GLM offers the advantage of simultaneously including multiple predictors. This capability allows for the integration of both spatial and head-directional variables within a unified model, providing a more comprehensive understanding of the neural activity.

Non-normality: Neural responses may not always follow a normal distribution. GLM is well-suited for situations where the response variable is not normally distributed, making it more robust for modeling neural data.

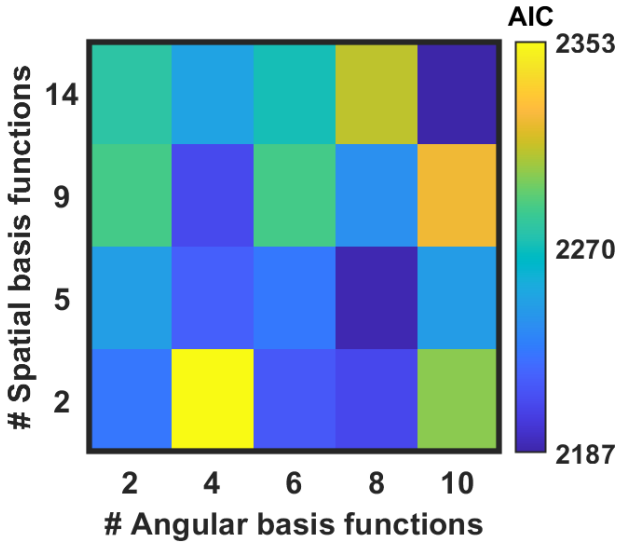

Figure 3.6: AIC-GUIDED MODEL SELECTION
The AIC values for various combinations of the number of spatial and angular basis functions for one animal. The AIC criteria is used for selecting the optimal models. the model's parameter count is determined by the summation of angular and spatial basis functions, alongside a constant function. The model with the minimum AIC is chosen as the most suitable. In this example, the optimal model consists of 15 spatial basis functions and 10 angular basis functions.

In our investigation of how neural selectivity changes with the acquisition of the MWM spatial navigation task, we recorded the activity of hundreds of hippocampal pyramidal cells (day 1: $n_{neurons}$= 171 ± 25, day 6: $n_{neurons}$= 197 ± 22, $n_{animals}$= 10) while recording the position and head-direction of the animals. To address the potential influence of varying total trial durations for day 1 and day 6 on the estimation of rate maps, we standardized the recording duration by increasing the number of trials recorded on day 6 and then randomly selecting trials for each day, ensuring that the sum of trial durations became equal for both days. Subsequently, we applied GLM to predict the spatial and head-direction modulation of these neurons (see section 2.12). To determine the best model, we tested different numbers of basis functions and utilized the Akaike Information Criterion (AIC) to identify the most suitable model. For the majority of animals, the preferred model featured 8–10 angular basis functions and 10–15 Zernike basis functions. Figure 3.6 illustrates the AIC values for various combinations of the number of spatial and angular basis functions for one animal. The optimal model was determined by the lowest AIC value. In this example, the optimal model

consisted of 15 spatial basis functions and 10 angular basis functions. To maintain a consistent model across all animals, we employed 15 spatial basis functions for position covariate and 10 angular basis functions for head-direction covariate.

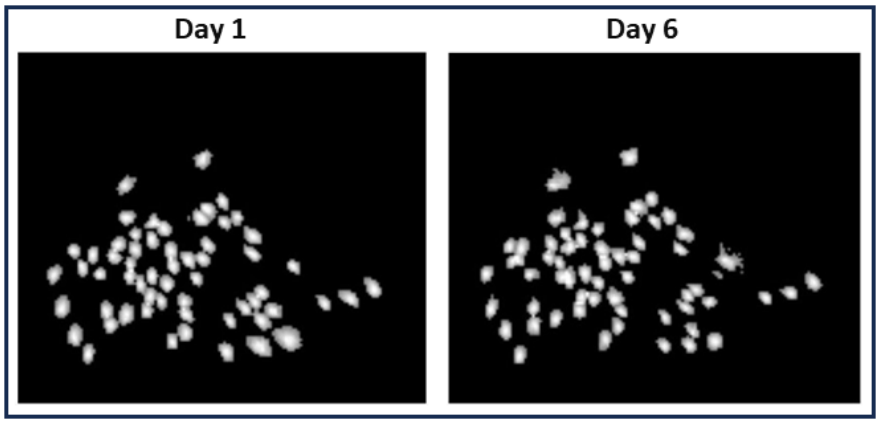

Figure 3.7: SAME CELLS CALCIUM IMAGING ACROSS DAYS
Calcium imaging of identical population of cells across day 1 and day 6

Leveraging the capabilities of the miniscope, we were able to consistently record from the identical set of cells across multiple days (Figure 3.7). This longitudinal approach provided us the opportunity to conduct a comprehensive analysis of individual cell activity, enabling a more refined understanding of how neural selectivity evolves throughout the learning process. Miniscope recordings followed by GLM analysis allowed us to track the spatial and HD selectivity of neurons throughout learning (Figure 3.8).

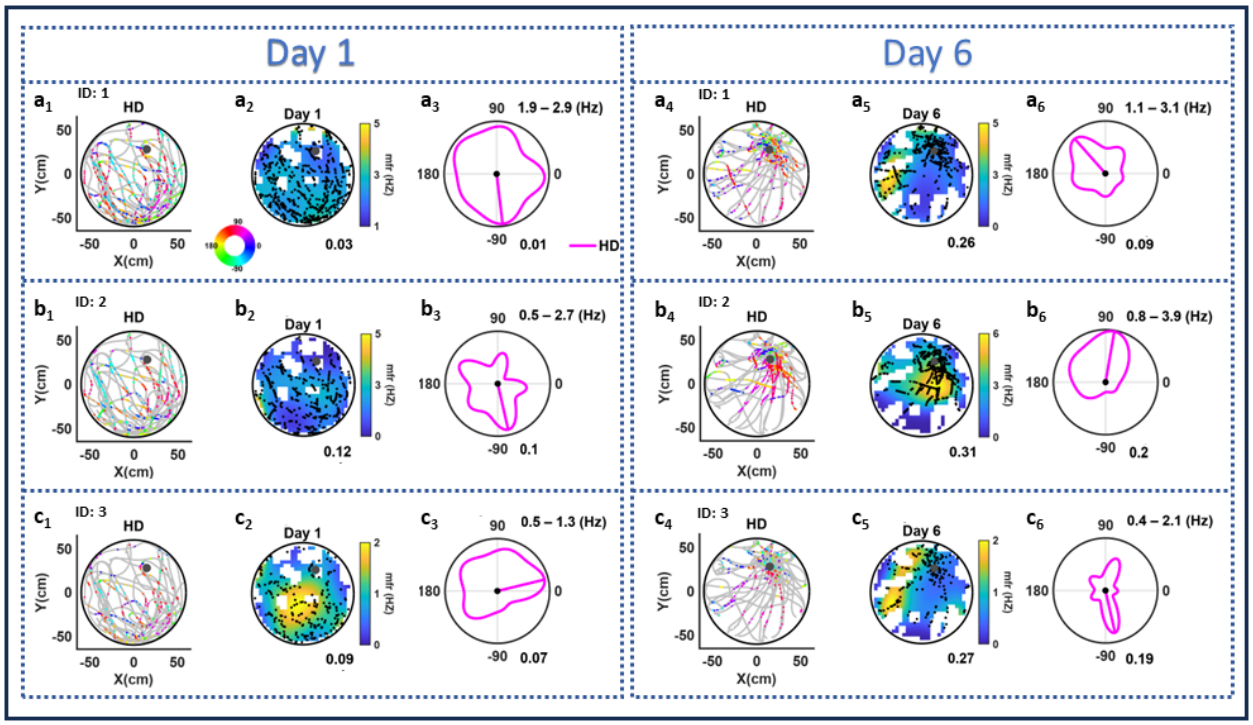

Figure 3.8: CELLS DISPLAYING VARYING DEGREES OF SPATIAL AND HEAD-DIRECTIONAL SELECTIVITY

Three representative cells are depicted with their spiking activities, spatial and head-directional selectivity, and the changes in the degree of selectivity observed between day 1 and day 6, after the animals successfully learned the task. **(a_1,b_1,c_1)** depict animal trajectories using light grey lines. Each dot represents the neuron's activity, with the color corresponding to the animal's head-direction. The grey circle located in the northeast quadrants depicts the position of the hidden platform. **(a_4,b_4,c_4)** and **(a_1,b_1,c_1)** represent the same three cells measured on day 1 and day 6, respectively. **(a_2,b_2,c_2)** and **(a_5,b_5,c_5)** illustrate the spatial firing rate map of the three neurons overlaid by the position of the animal when the firing activity occurred. The lighter color on the spatial firing rate map corresponds to the higher firing rate. The number in the bottom right corner indicates the sparsity of the spatial map. **(a_3,b_3,c_3)** and **(a_6,b_6,c_6)** show the angular rate map of the three cells. The number in the bottom right corner indicates the sparsity of the angular map and the two numbers in the top right corner of the polar plot show the range of firing rate of the angular rate map.

As the animals become more proficient in the MWM task, there was a significant increase in spatial sparsity (day 1: 0.19 ± 0.01, day 6: 0.28 ± 0.01, p= 6.63×10^{-4}). Similarly, head-directional sparsity increased, although the change was not statistically significant (day 1: 0.10 ± 0.01, day 6: 0.12 ± 0.01, p= 0.0568).

As we delved into potential factors that could influence the results obtained by GLM, we observed a notable shift in the animals' behavior, indicating increased bias on day 6. As the animals learned the task, they adopted more direct paths from the starting point toward the hidden platform (Figure 3.3). Consequently, this behavior led to a fewer visits to distinct locations within the pool. Moreover, the animals sampled fewer head-directions, particularly when taking a straight path, where the head-direction remained relatively stable. To address this concern, we calculated the sparsity for the shuffled data (see section 2.15). As illustrated in Figure 3.9 (a, b) the shuffled data also exhibited a significant increase in spatial sparsity (day 1: 0.16 ± 0.02, day 6: 0.21 ± 0.01, p= 0.0027) and a trend toward increased head-direction sparsity (day 1: 0.07 ± 0.01, day 6: 0.09 ± 0.01, p= 0.1331), respectively. To mitigate the impact of behavioral biases on the predicted sparsity of the rate maps by GLM and its potential influence on the observed increase in sparsity on day 6,we subtracted the sparsity of the shuffled data from the sparsity of the empirical data (see section 2.16). The results demonstrated a significant increase in spatial sparsity (day 1: 0.01 ± 0.01, day 6: 0.04 ± 0.01, p= 6.56×10^{-4}) and a significant increase in head-direction sparsity (day 1: 0.01 ± 0.01, day 6: 0.03 ± 0.01, p= 0.0226); Figure 3.9 (c) and (d), respectively.

Next, in our exploration of changes in neural responses associated with learning, we utilized the miniscope's capability to track neurons across multiple days. This approach enabled us to confine our analysis to the identical set of cells recorded on both day 1 and day 6, ensuring a direct and consistent comparison ($n_{neurons}$= 68 ± 10, $n_{animals}$= 10). As depicted in Figure 3.10 (a,b), the results were consistent with the findings obtained when comparing the spatial and head-directional sparsity of day 1 and day 6 using all recorded cells. The spatial sparsity showed a significant increase (day 1: 0.19 ± 0.02, day 6: 0.30 ± 0.01, p= 2.84×10^{-5}), and similarly, head-directional sparsity also significantly increased (day 1: 0.10 ± 0.01, day 6: 0.13 ± 0.01, p= 0.0133). Consistent with the previous results using all cells, the spatial and head-directional sparsity for the shuffled data exhibited a similar trend as the spatial and head-directional sparsity for the empirical data. For shuffled spatial sparsity: (day 1: 0.16 ± 0.02, day 6: 0.24 ± 0.02, p= 6.56×10^{-5}), and for shuffled head-directional sparsity (day 1: 0.08 ± 0.02, day 6: 0.1 ± 0.01, p= 0.0365). After

subtracting shuffled values from the sparsity measurements, the subtracted spatial sparsity exhibited a significant increase from day 1 to day 6 (day 1: 0.01 ± 0.01, day 6: 0.04 ± 0.01, p= 0.0014), and similarly, the subtracted head-directional sparsity showed a significant increase from day 1 to day 6 (day 1: 0.01 ± 0.01, day 6: 0.03 ± 0.01, p= 0.0289). Therefore, single cell GLM analysis demonstrates that spatial and HD sparsity increase with learning on the MWM task.

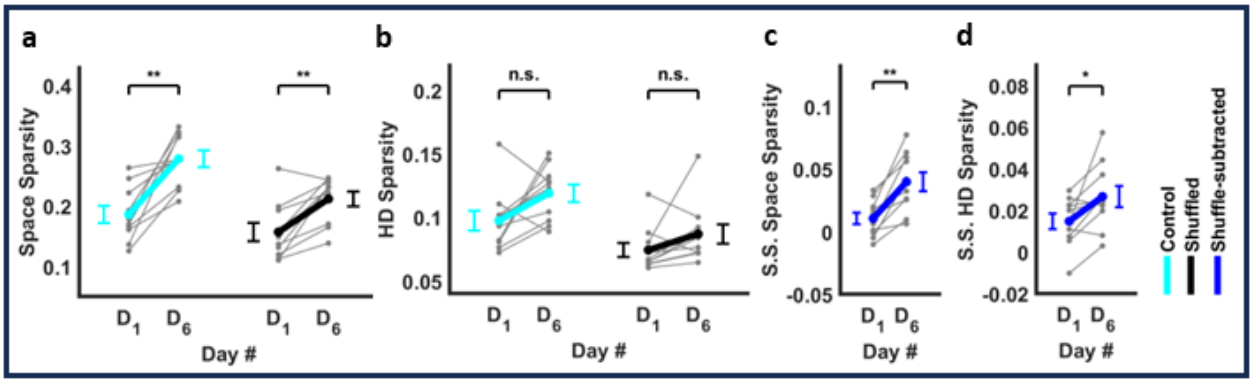

Figure 3.9: CHANGES OF SPATIAL AND HEAD-DIRECTIONAL SELECTIVITY THROUGH LEARNING ACROSS ALL RECORDED PYRAMIDAL NEURONS
(a) Significant increase in the control space sparsity (day 1: 0.19 ± 0.01, day 6: 0.28 ± 0.01, paired sample t-test, $n = 10$, p= 6.63×10^{-4}), and significant increase in shuffled space sparsity (day 1: 0.16 ± 0.02, day 6: 0.21 ± 0.01, paired sample t-test, p= 0.0027).**(b)** Non-significant increase in the control HD sparsity (day 1: 0.10 ± 0.01, day 6: 0.12 ± 0.01, paired sample t-test, p= 0.0568), and non-significant increase in the shuffled HD sparsity (day 1: 0.07 ± 0.01, day 6: 0.09 ± 0.01, paired sample t-test, p= 0.1331). **(c)** Significant increase in the shuffle-subtracted space sparsity (day 1: 0.01 ± 0.01, day 6: 0.04 ± 0.01, paired sample t-test, p= 6.56×10^{-4}), and **(d)** significant increase in shuffle-subtracted HD sparsity (day 1: 0.01 ± 0.01, day 6: 0.03 ± 0.01, paired sample t-test, p= 0.0226). '*' p< 0.05, '**' p< 0.005, '***' p< 0.0005.

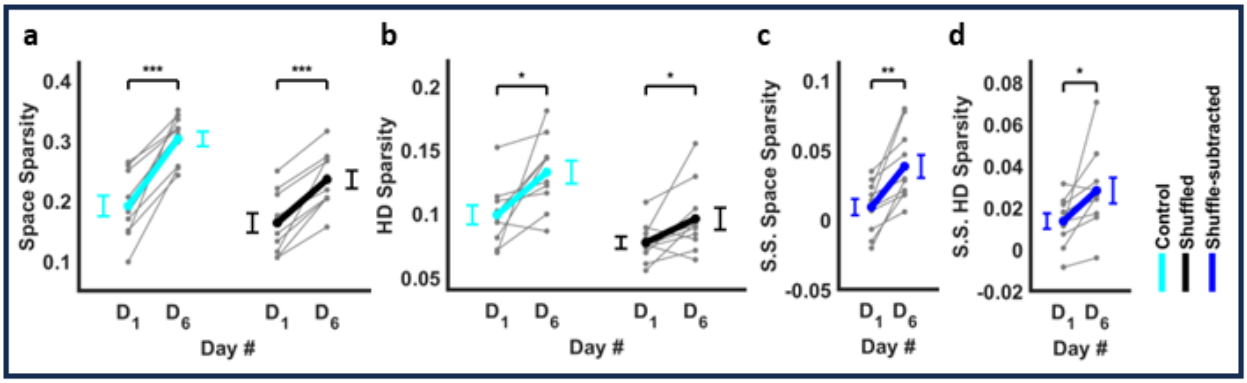

Figure 3.10: CHANGES OF SPATIAL AND HEAD-DIRECTIONAL SELECTIVITY THROUGH LEARNING ACROSS SAME PYRAMIDAL NEURONS RECORDED IN DAY 1 AND DAY 6

(a) Significant increase in the control space sparsity (day 1: 0.19 ± 0.02, day 6: 0.30 ± 0.01, paired sample t-test, $n = 10$, p= 2.84×10^{-5}), and significant increase in the shuffled space sparsity (day 1: 0.16 ± 0.02, day 6: 0.24 ± 0.02, paired sample t-test, p= 6.56×10^{-5}). **(b)** Significant increase in the control HD sparsity (day 1: 0.10 ± 0.01, day 6: 0.13 ± 0.01, paired sample t-test, p= 0.0133), and significant increase in the shuffled HD sparsity (day 1: 0.08 ± 0.01, day 6: 0.1 ± 0.01, paired sample t-test, p= 0.0365). **(c)** Significant increase in the shuffle-subtracted space sparsity (day 1: 0.01 ± 0.01, day 6: 0.04 ± 0.01, paired sample t-test, p= 0.0014), and **(d)** significant increase in shuffle-subtracted HD sparsity (day 1: 0.01 ± 0.01, day 6: 0.03 ± 0.01, paired sample t-test, p= 0.0289). '*' p< 0.05, '**' p< 0.005, '***' p< 0.0005.

3.5 Decoding neural signals with artificial neural networks

In the previous section, we explored how the sparsity of individual neurons' spatial and head-directional rate maps changes over time. We found a significant increase in the sparsity of these rate maps, and this change was statistically linked to the learning experience. Next, we explored the extent of information encoded by a neural population regarding different covariates. To assess this, we utilized feedforward artificial neural networks for decoding neural signals. Our hypothesis posits that as the neural activities encode more information about position and head direction, the performance of the feedforward neural network in decoding improves, consequently reducing decoding errors.

Glaser et al. demonstrated that for the data recorded from hippocampus, among the various

networks tested, feedforward neural networks (FFNs) achieved decoding accuracy comparable to or better than the other 10 models (e.g., recurrent neural networks, long short-term memory networks, gated recurrent unit, Wiener Filter, naive Bayes) they examined ([GBC20]). Considering their computational efficiency, with feedforward neural networks running faster than some other methods, and achieving either superior or comparable accuracy on our data, we made the decision to opt for FFNs. We employed three feedforward neural networks with different structures, incorporating multiple hidden layers and varying numbers of neurons in each layer to decode three variables: position, head-direction, and distance from the platform (see section 2.18). Our approach focused on using data exclusively from days 1 and 6, ensuring comparable data duration for a fair comparison. To achieve this, we randomly selected trials from day 1 and day 6, ensuring that the cumulative length of the trials was equal. Subsequently, we allocated 80% of the data for training the feedforward neural networks and reserved the remaining 20% for evaluating the prediction performance.

3.6 Decoding position, head-direction, and distance to the platform

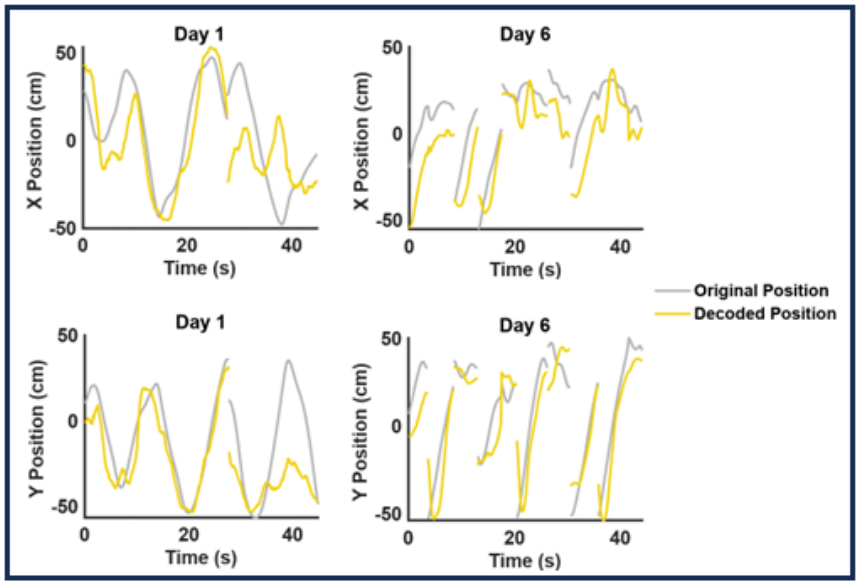

Figure 3.11: EXAMPLE DECODER RESULT FOR POSITION
Example of a decoding performance in predicting the position of an animal. The grey line shows the original position trace and the yellow line represents the decoded position by FNN. The decoder's performance increased on day 6 compared to day 1.

Feedforward neural decoders could predict spatial position, HD, and distance on both day 1 and day 6. (see Figure 3.11 for example position decoding). As the animals learned the task, the decoded position error decreased on day 6 compared to day 1 (day 1: 37.3 ± 2.4 cm, day 6: 25.6 ± 1.4 cm, p= 8.67×10^{-5}). Moreover, the position decoding error for shuffled data displayed a similar trend (day 1: 41.1 ± 2.3 cm, day 6: 35.9 ± 1.1 cm, p= 0.0338). Of note, as the animals learned the task, they visited fewer locations and took more direct paths to reach the platform. Consequently, this biased behavior could potentially result in smaller decoding error. To address this issue, we subtracted the 95-th percentile of the error for the shuffled data from the error of the decoded original position. The shuffle-subtracted error also significantly decreased in day 6 compared to day 1 (day 1: 1.8 ± 2.0, day 6: -4.9 ± 1.4, p= 0.0084). Therefore, population decoding of spatial position improves with learning.

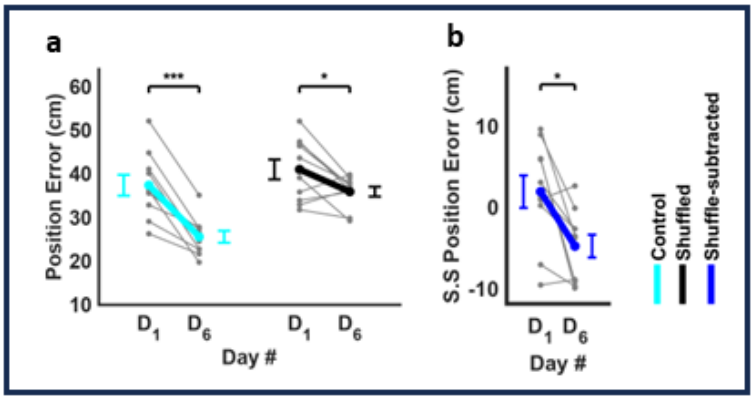

Figure 3.12: REDUCTION IN POSITION DECODING ERROR
The decoded position exhibited a notable decrease in error on day 6 compared to day 1. **(a)** The error for the empirical data demonstrated a significant drop (day 1: 37.3 ± 2.4 cm, day 6: 25.6 ± 1.4 cm, paired sample t-test, $n = 10$, p= 8.67×10^{-5}). Likewise, the error for the shuffled data revealed a significant decrease (day 1: 41.1 ± 2.3 cm, day 6: 35.9 ± 1.1 cm, paired sample t-test, p= 0.0338). **(b)** The error for the shuffle-subtracted exhibited a significant reduction (day 1: 1.8 ± 2.0, day 6: -4.9 ± 1.4, paired sample t-test, p= 0.0084).

While there was no significant change in correlation between empirical and decoded positions from day 1 to day 6 (day 1: 0.42 ± 0.08, day 6: 0.52 ± 0.06, p= 0.3015), the correlation for the shuffled data exhibited a significant decrease (day 1: 0.33 ± 0.09, day 6: 0.01 ± 0.04, p= 0.0071). Therefore, the correlation for the shuffle-subtracted data demonstrated a statistically significant increase (day 1: -0.07 ± 0.06, day 6: 0.24 ± 0.06, p= 0.0045). This reinforces the previous decoding results that showed improved decoding of spatial position after learning.

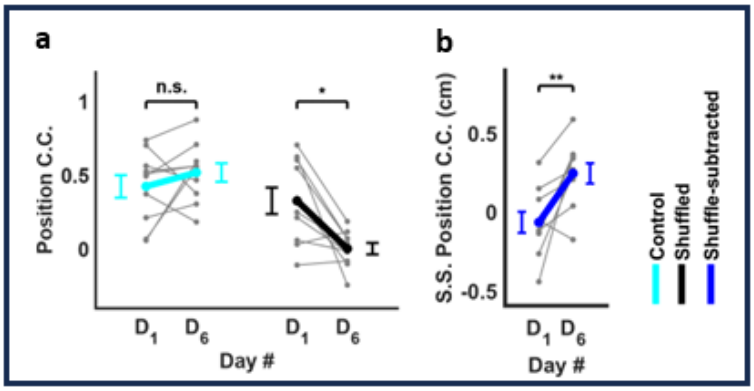

Figure 3.13: IMPROVEMENT IN POSITION DECODING CORRELATION
(a) Empirical-decoded position correlation showed no significant change in empirical data (day 1: 0.42 ± 0.08, day 6: 0.52 ± 0.06, paired sample t-test, $n = 10$, p= 0.3015), and the shuffled position showed a significant decrease (day 1: 0.33 ± 0.09, day 6: 0.01 ± 0.04, paired sample t-test, p= 0.0071). **(b)** The shuffle-subtracted data exhibited a significant increase (day 1: -0.07 ± 0.06, day 6: 0.24 ± 0.06, paired sample t-test, p= 0.0045).

Similarly, we decoded head-direction and distance to the platform using FNN. (Figure 3.14 and Figure 3.15).

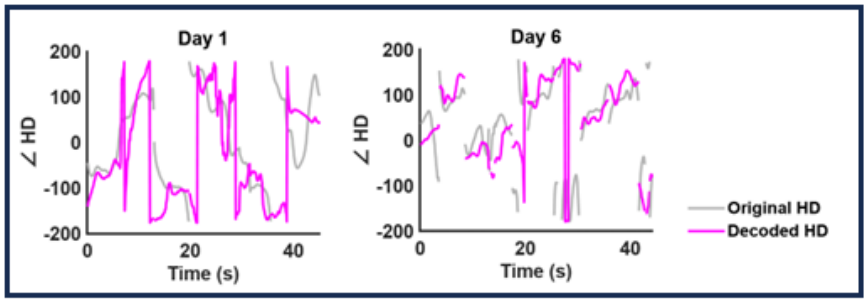

Figure 3.14: EXAMPLE DECODER RESULT FOR HEAD-DIRECTION
Example of a decoding performance in predicting the head-direction of an animal. The grey line shows the original head-direction trace and the magenta line represents the decoded head-direction by FNN. The decoder's performance increased on day 6 compared to day 1.

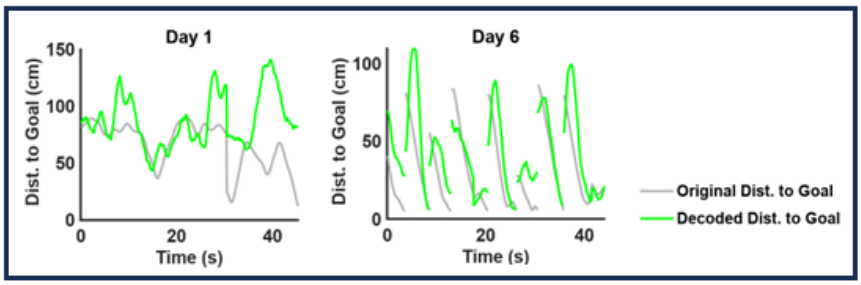

Figure 3.15: EXAMPLE DECODER RESULT FOR DISTANCE TO THE GOAL
Example of a decoding performance in predicting the distance to the platform of an animal. The grey line shows the original distance to the platform trace and the green line represents the decoded distance to the platform by FNN. The decoder's performance increased on day 6 compared to day 1.

There was a significant reduction in the error for the decoded head-direction (day 1: 71.9 ± 4.1, day 6: 54.6 ± 4.0, p= 8.19×10^{-4}), while the shuffled data didn't show any significant changes from day 1 to day 6 (day 1: 84.1 ± 5.1, day 6: 85.4 ± 4.3, p= 0.832; Figure 3.16). Moreover, the shuffle-subtracted data also showed a significant reduction (day 1: 0.7 ± 3.9, day 6: -11.3 ± 3.2, p= 0.002).

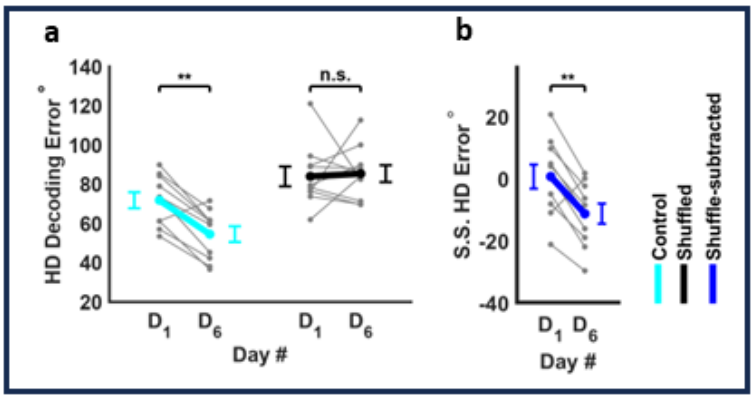

Figure 3.16: IMPROVEMENT IN HEAD-DIRECTION DECODING THROUGH LEARNING
The decoded head-direction exhibited a significant decrease in error on day 6 compared to day 1. **(a)** The error for the empirical data demonstrated a significant drop (day 1: 71.9 ± 4.1, day 6: 54.6 ± 4.0, paired sample t-test, $n = 10$, p= 8.19×10^{-4}). However, the error for the shuffled data revealed any significant changes (day 1: 84.1 ± 5.1, day 6: 85.4 ± 4.3, paired sample t-test, p= 0.832). **(b)** The error for the shuffle-subtracted exhibited a significant reduction (day 1: 0.7 ± 3.9, day 6: -11.3 ± 3.2, paired sample t-test, p= 0.002).

There was also a significant reduction in the decoded error for the distance to the platform (day 1: 24.6 ± 1.8 cm, day 6: 15.5 ± 0.6 cm, p= 0.0029; Figure 3.17). Conversely, the shuffled data exhibited no significant alterations from day 1 to day 6 (day 1: 27.9 ± 2.1 cm, day 6: 24.3 ± 1.1 cm, p= 0.1455). Therefore, the shuffle-subtracted data demonstrated a substantial reduction in error (day 1: 5.2 ± 1.7, day 6: −2.9 ± 0.4, p= 0.0022). Therefore, decoding of head direction and distance to the platform also improved with learning. These findings are in agreement with single neuron GLM analysis.

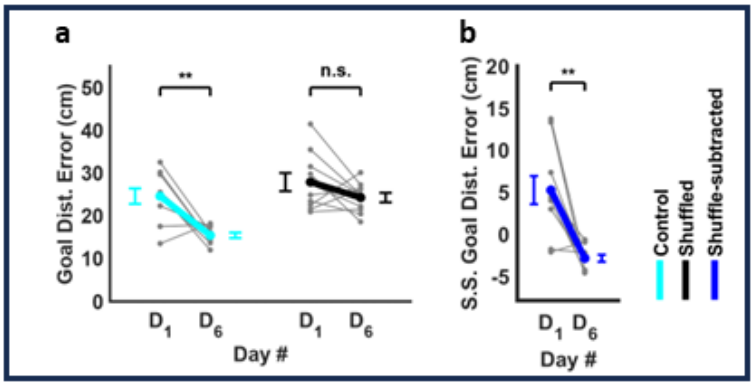

Figure 3.17: IMPROVEMENT IN DISTANCE TO THE PLATFORM DECODING THROUGH LEARNING
The decoded distance to the platform exhibited a significant decrease in error on day 6 compared to day 1. **(a)** The error for the empirical data demonstrated a significant drop (day 1: 24.6 ± 1.8 cm, day 6: 15.5 ± 0.6 cm, paired sample t-test, n = 10, p= 0.0029). However, the error for the shuffled data revealed no significant changes (day 1: 27.9 ± 2.1 cm, day 6: 24.3 ± 1.1 cm, paired sample t-test, p= 0.1455). **(b)** The error for the shuffle-subtracted exhibited a significant reduction (day 1: 5.2 ± 1.7, day 6: −2.9 ± 0.4, paired sample t-test, p= 0.0022).

3.7 Position and head-direction conjunctive analysis

In the previous sections, we examined changes in neural responses at both the single-cell and population levels. To further refine our analysis and ensure an unbiased comparison, we performed conjunctive coding analysis where we directly compared the firing rates of neurons when the animals were in the same position and headed in the same direction.

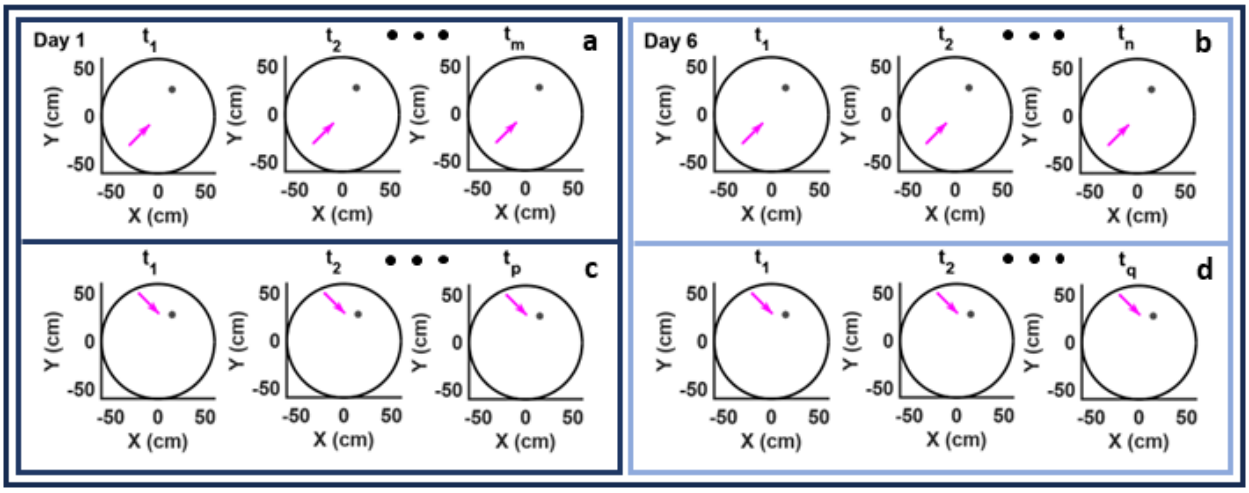

Figure 3.18: SCHEMATIC OF POSITION AND HEAD-DIRECTION CONJUNCTIVE ANALYSIS
Comparing neural responses by aligning position and head-direction bins on day 1 and day 6. The analysis focused on time bins with matched positions, head-direction, and speeds between 10–25 cm/s on both days. Averaged neural signals in m time bins of day 1 **(a)** are compared with n time bins of day 6 **(b)**, aligning position and head-direction shown as in the figure. Similarly, for another example, averaged neural signals in p time bins of day 1 **(c)** are compared with q time bins of day 6 **(d)**.

For the conjunctive analysis, we segmented the position and head-direction of an animal into bins, using 4x4 bins for space and 3 degrees for head-directions on both day 1 and day 6. Subsequently, we identified time bins on day 1 and day 6 that shared the same head-direction and position (schematic for approach shown in Figure 3.18).

Hence, we compared the neural signals of those time bins that had similar positions and head--directions on day 1 and day 6. Additionally, to further refine our analysis we focused exclusively on intervals when the animal's speed fell within the range of 10–25 cm/s on both days (Figure 3.19 (c)). Moreover, we only included cells recorded on both day 1 and day 6.

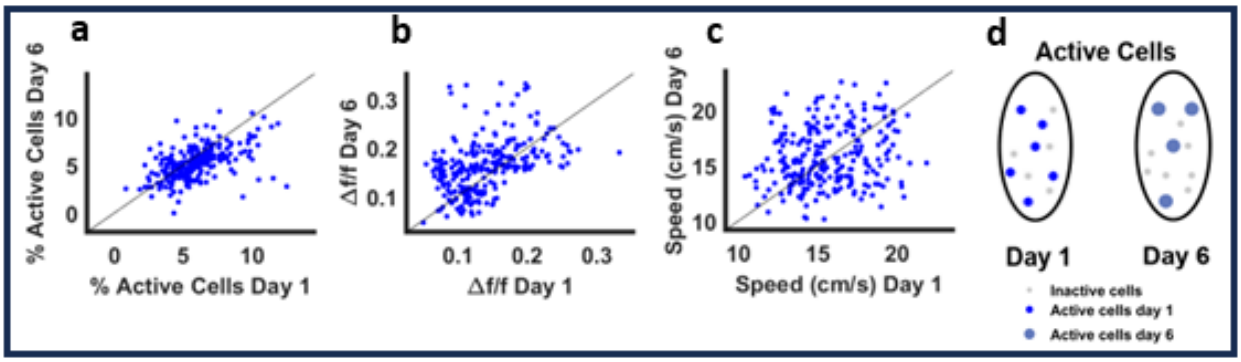

Figure 3.19: REDUCTION IN THE PERCENTAGE OF ACTIVE CELLS AND INCREASE IN FLUORESCENCE INTENSITY CHANGES AFTER LEARNING
Exploring neural activity within similar positions and head directions on both day 1 and day 6. **(a)** The percentage of active cells experienced a significant drop from day 1 to day 6 (day 1: 5.9% ± 1.9% ($\mu \pm \sigma$), day 6: 5.2% ± 1.6%, paired sample t-test, $n_{animals}$= 10, p= 6.35×10^{-9}). **(b)** There was a simultaneous significant increase in fluorescence intensity changes (day 1: 0.14 ± 0.05, day 6: 0.16 ± 0.05, paired sample t-test, p= 3.55×10^{-9}). **(c)** There were no significant differences in speed from day 1 to day 6 (day 1: 15.6 ± 2.4 (cm/sec), day 6: 15.8 ± 2.6 (cm/sec), paired sample t-test, p= 0.2452). **(d)** Summarizes the conjunctive analysis. Inactive cells, depicted by gray circles, contrast with active cells highlighted in color. A visible reduction in the percentage of active cells from day 1 to day 6 is reflected in fewer colored circles on day 6. Larger circle sizes on day 6 denote increased fluorescence intensity.

Our conjunctive analysis revealed a significant reduction in the percentage of active cells in each place/HD conjunction from day 1 to day 6 as the animals learned the task (Figure 3.19 (a), p= 6.35×10^{-9}). In addition, there was a significant increase in the average intensity of the calcium signals for activated neurons during the same learning period (Figure 3.19 (b), p= 3.55×10^{-9}). Notably, when considering data only within the speed range of 10–25 cm/s, no significant difference in speed was observed between day 1 and day 6 (Figure 3.19 (c), p= 0.2452).

In our subsequent analysis, we explored potential changes in neural response in each conjunctive field depending on their distance from the hidden platform (Figure 3.20). We found that there was no significant difference in the percentage of active cells and the mean amplitude of calcium transients for fields located at short distances (5–15 cm) and long distances (60–70 cm) from the platform on day 1 (p= 0.3397 and p= 0.2473 and, respectively). However, on day 6, there was a significant increase in the percentage of active cells (p= 1.80×10^{-21}), and a significant reduction

in the amplitude of the mean calcium transient with increasing distance from the platform ($p = 5.43 \times 10^{-55}$). Therefore, when comparing activity of the neurons firing when animals were in the same spatial location and headed in the same direction, fewer neurons were active after learning, though the intensity of neural signal increased.

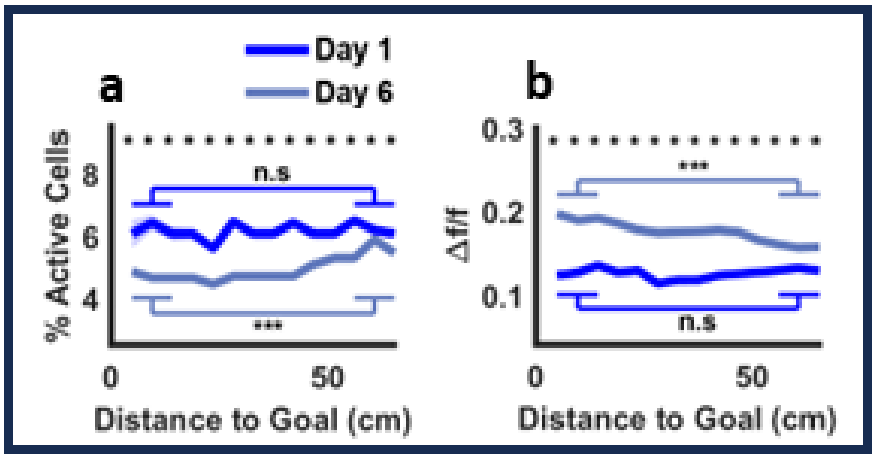

Figure 3.20: IMPACT OF LEARNING ON NEURAL RESPONSES AS A FUNCTION OF DISTANCE TO THE GOAL
(a) The percentage of active cells decreased from day 1 to day 6 across varying distances to the platform. Significant reductions in the percentage of active cells are denoted by '*'. There was no significant difference between the percentage of active cells for short distances (5–15 cm) compared to long distances (60–70 cm) from the goal on day 1 (day 1: close distance: 6.06 ± 4.22, far distance: 6.17 ± 3.62, two-sided Wilcoxon rank-sum test, $p = 0.3397$). However, a significant increase in the percentage of active cells for long distances compared to short distances from the goal was observed on day 6 (day 6: close distance: 4.65 ± 2.89, far distance: 5.45 ± 4.49, two-sided Wilcoxon rank-sum test, $p = 1.80 \times 10^{-21}$). **(b)** Fluorescence intensity changes exhibited a notable increase from day 1 to day 6 across diverse distances to the platform, with significant enhancements marked by '*'. On day 1, no statistically significant distinction emerged in fluorescence intensity changes between short distances and long distances from the goal (close distance: 0.13 ± 0.06, far distance: 0.13 ± 0.06, two-sided Wilcoxon rank-sum test, $p = 0.2473$). However, on day 6, a significant reduction in fluorescence intensity changes for long distances compared to short distances from the goal was evident (close distance: 0.19 ± 0.09, far distance: 0.16 ± 0.09, two-sided Wilcoxon rank-sum test, $p = 5.43 \times 10^{-55}$).

3.8 Link between LTP and learning spatial navigation

Long term potentiation in CA1 has been shown to be critical for learning [MAL86, SPW92, THT96, ZLX18]. To determine whether the improvements in spatial and HD coding measured after learning were driven by LTP, we conducted similar experiments in GluA1^{C2KI} mice. These mice have been previously characterized by normal synaptic transmission but exhibit reduced Schafer Collateral LTP and impaired performance in learning tasks such as the Morris water maze [ZLX18].

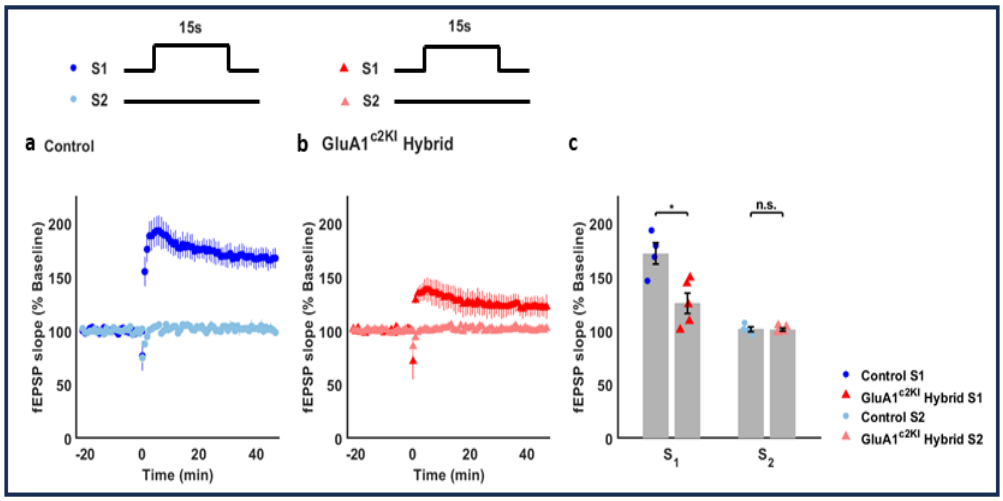

Figure 3.21: LTP DEFICIENCY IN GLUA1^{C2KI} ANIMALS
2 stimulating electrodes were used to activate independent groups of excitatory synapses (S1 and S2). After time = 0, a 15 second long train of 5 Hz stimulation was delivered to S1 synapses. **(a)** Results from wild type mice. **(b)** Results from GluA1^{C2KI} mutants. **(c)** Results from individual experiments showing changes in synaptic strength at S1 and S2 synapses. At 45 minutes post-TPS, S1 synapses potentiated to 172 ± 5% of baseline in slices from wild type mice ($n_{\text{wild type}}$ =4) and were 126 ± 4% of baseline in slices from GluA1^{C2KI} mutants ($n_{\text{GluA1}^{C2KI}}$= 5, two-sided Wilcoxon rank-sum test, p= 0.032). S2 synapses potentiated to 101 ± 1% of baseline in slices from wild type mice and were 101 ± 1% of baseline in slices from wildtGluA1^{C2KI} mutants (p= 0.905).

We first confirmed whether GluA1^{C2KI} animals indeed had reduced LTP. Two stimulating electrodes (S1 and S2) were used to activate independent groups of Schaffer collateral fiber synapses. 15 seconds of theta pulse stimulation (TPS, single stimulation pulses delivered at 5 Hz) was delivered to S1 synapses. At 45 minutes post-TPS, S1 synapses potentiated to 172% of baseline in slices from the wild type mice and were 126% of baseline in slices from GluA1^{C2KI} mutants. Therefore

significant LTP reduction was observed in GluA1^{C2KI} mutants (Figure 3.21).

In another experiment, we assessed a different paradigm for LTP induction based on behavioral time-scale cooperativity which may be similar to plasticity obsvered in in-vivo. 10 seconds of TPS was delivered to S1 synapses and, following a 2-second delay, a 5-second-long train of TPS was delivered to S2 synapses. Normally, 5 seconds of TPS alone has no lasting effect on synaptic strength but can induce LTP if delivered following trains of TPS delivered to S1 synapses. The result showed significant reduction in LTP in GluA1^{C2KI} animals compared to the wild type animals (Figure 3.22).

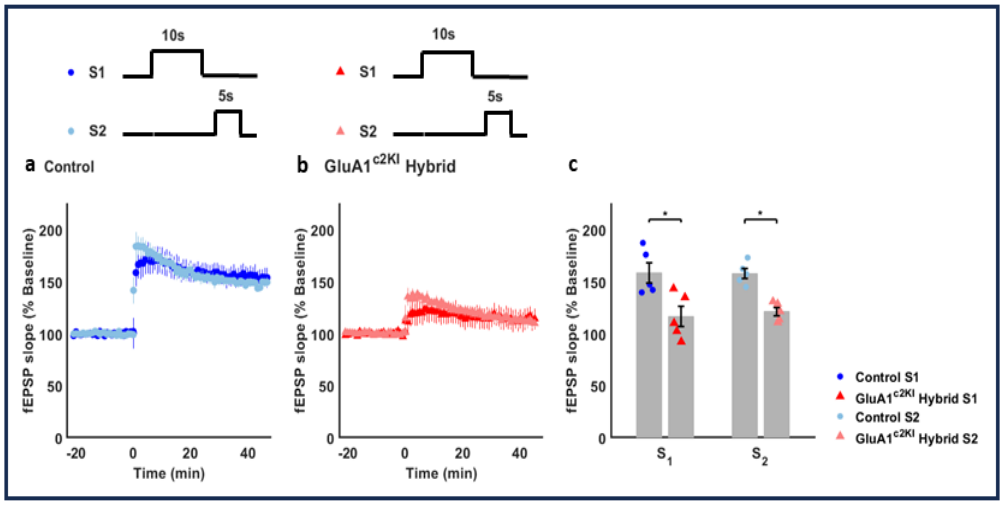

Figure 3.22: DISRUPTED BEHAVIORAL TIMESCALE SYNAPTIC COOPERATIVITY IN GLUA1^{C2KI} ANIMALS
Two stimulating electrode were used to activate 2 independent groups of synapses. At time = 0, 10 seconds of 5 Hz stimulation was delivered to S1 synapses followed by a 5 second long train of 5 Hz stimulation delivered to S2 synapses (inter-train interval = 2 seconds). **(a)** Wild type results. **(b)** Results from mutants. **(c)** Summary showing changes in synaptic strength at S1 and S2 synapses in slices from wild type and mutant mice. At 45 minutes post-TPS, S1 synapses potentiated to 159 ± 4% of baseline in slices from wild type mice ($n_{\text{wild type}}$= 5), and were 117 ± 4% of baseline in slices from GluA1^{C2KI} mutants ($n_{\text{GluA1}^{C2KI}}$= 5, two-sided Wilcoxon rank-sum test, p= 0.032). S2 synapses potentiated to 158 ± 2% of baseline in slices from wild type mice and were 121 ± 2% of baseline in slices from GluA1^{C2KI} mutants (p= 0.008)

3.9 Performance of the GluA1^{C2KI} mice in MWM

To determine if reduction of LTP results in altered spatial, HD and distance coding, we performed MWM experiments in GluA1c2K1 animals and controls. GluA1^{C2KI} and control animals showed a significant and similar decrease in escape latencies in the MWM with training (Figure 3.23 (a_1–a_6), Figure 3.24 (a), day 1: 51.4 ± 1.7 s, day 6: 23.9 ± 9.1 s, p= 0.0351). Moreover, similar to the controls, the head-direction occupancy of GluA1^{C2KI} animals exhibited a gradual shift towards the north, slightly offset from the northeast, indicating a directional preference aligned more towards the hidden platform (Figure 3.23 (b_1–b_6)). Therefore GluA1^{C2KI} animals do not show impairments in escape latency.

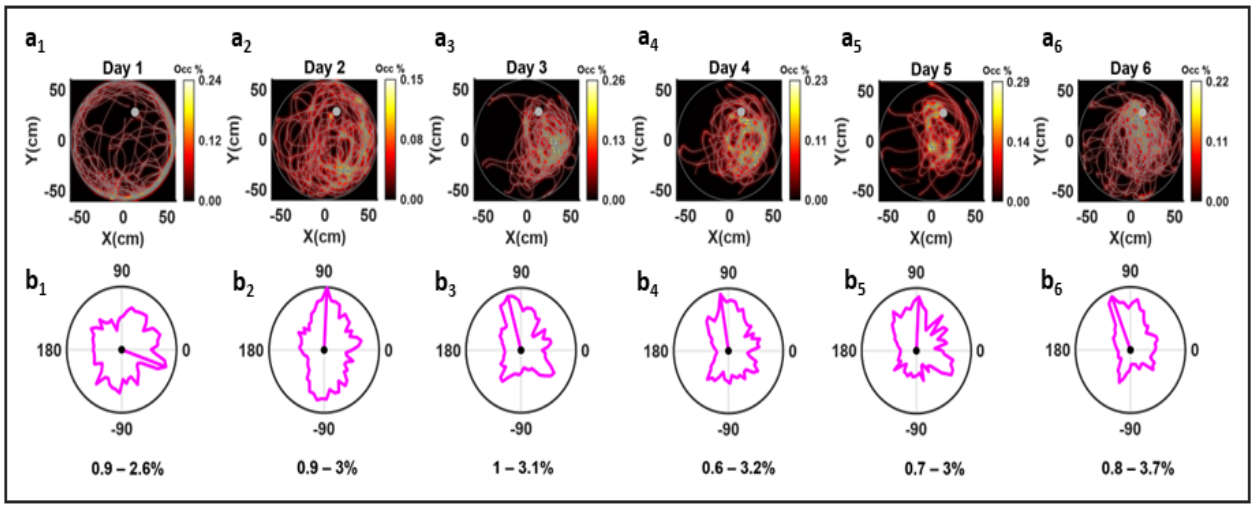

Figure 3.23: SPACE AND HEAD-DIRECTION OCCUPANCY IN GLUA1^{C2KI} ANIMALS
Example of space and head-direction occupancy for a GluA1^{C2KI} animal. (a_1–a_6) As the animal gained proficiency in the task, it started taking a more direct route to the platform and spent increased time in the vicinity of the hidden platform. (b_1–b_6) The head-direction gradually oriented towards the north, with a slight offset from the northeast, corresponding to the location of the hidden platform.

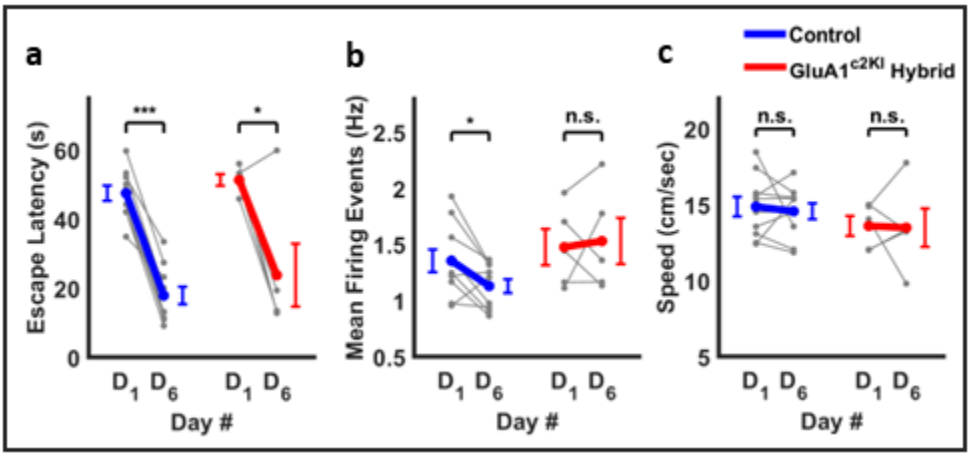

Figure 3.24: REDUCTION IN ESCAPE LATENCY AND AVERAGE FIRING ACTIVITY IN GLUA1^{C2KI} ANIMALS
As the animal gained proficiency in the task: (a) Experienced a significant reduction in escape latency (day 1: 51.4 ± 1.7 s, day 6: 23.9 ± 9.1 s, paired sample t-test, n = 5, p= 0.0351). (b) Demonstrated no significant change in mean firing activity (day 1: 1.48 ± 0.16 Hz, day 6: 1.53 ± 0.21 Hz, paired sample t-test, p= 0.7886). (c) The speed of the animal on day 1 was not significantly different from the speed on day 6 (day 1: 13.61 ± 0.66 cm/s, day 6: 13.50 ± 1.26 cm/s, paired sample t-test, p= 0.9358). '*' p< 0.05, '**' p< 0.005, '***' p< 0.0005.

To maintain consistency with the control group, we selectively included data from GluA1^{C2KI} animals when their speed exceeded 3 cm/s. As depicted in Figure 3.24 (c), there were no significant differences in speed between day 1 and day 6 for GluA1^{C2KI} animals (day 1: 13.61 ± 0.66 cm/s, day 6: 13.50 ± 1.26 cm/s, p= 0.9358). However, unlike the control group, which exhibited a significant drop in mean firing events, the GluA1^{C2KI} animals did not show any significant reduction in the mean firing events (3.24 (b), day 1: 1.48 ± 0.16 Hz, day 6: 1.53 ± 0.21 Hz, p= 0.7886).

3.10 Probe analysis of GluA1^{C2KI} mice in MWM

As stated previously, the control group demonstrated a significant increase in the time spent in the first quadrant during the probe trial after day 6 (Figure 3.25 (b)) demonstrating successful spatial learning. Similarly, the number of target crossings was significantly higher in the first quadrant than in the other quadrants (Figure 3.25 (c)). Yet, GluA1^{C2KI} animals did not demonstrate significant

difference in the quadrant occupancy in day 6 (Figure 3.25(b), F(3,12)= 1.29, p= 0.3215), and the mutant and control showed significantly different in the time spent on different quadrants on day 6 (Figure 3.25(b), F(3,39)= 3.38, p= 0.0276). The number of target crossings was not significantly different in the first quadrant compared to the other quadrants on day 6 in mutant animals (Figure 3.25(c), F(3,12)= 1.37, p= 0.2981). Therefore, while mutants showed no difference in escape latencies, probe trials which are a more sensitive assay for learning deficits demonstrated learning deficits in GluA1^{C2KI} mice.

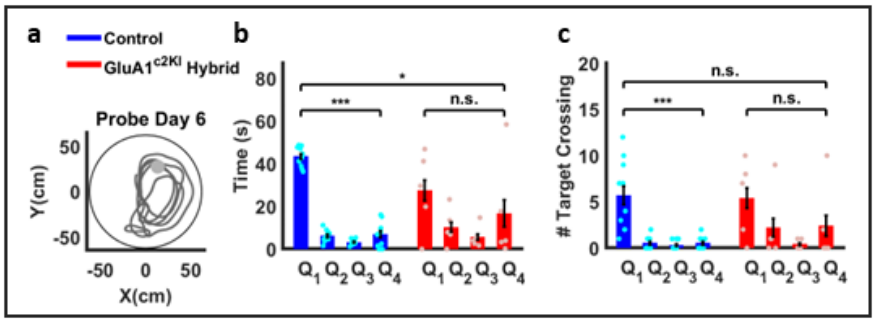

Figure 3.25: PROBE TRIAL DIFFERENCES IN GLUA1^{C2KI} MICE VS. CONTROLS
(a) Animal's trajectory during the second probe after the training on day 6. **(b)** During the probe trial after day 6, animals did not display a significant extended presence in the vicinity of the hidden platform's training location however, there is a significant difference between the control and the GluA1^{C2KI} groups in the time spent in different quadrants on day 6 (see Figure 3.5 for the control group statistics. GluA1^{C2KI} day 6: repeated measures ANOVA, F(3,12)= 1.29, p= 0.3215. Planned comparisons paired t-test (Q_1, Q_2)= 0.0787, (Q_1, Q_3)= 0.0682, (Q_1, Q_4)= 0.5963, repeated two-way measures ANOVA, F(3,39)= 3.38, p= 0.0276). **(c)** The number of target crossings is not significantly different in the first quadrant compared to the other quadrants, and there is no significant difference between the control and the GluA1^{C2KI} group on day 6 (day 6: repeated measures ANOVA, F(3,12)= 1.37, p= 0.2981. Planned comparisons paired t-test (Q_1, Q_2)= 0.1642, (Q_1, Q_3)= 0.0623, (Q_1, Q_4)= 0.4585, repeated two-way measures ANOVA, F(3,39)= 0.54, p= 0.6602). Bonferroni correction is applied. '*' p< 0.0167, '**' p< 0.0017, '***' p< 1.67×10^{-4}.

3.11 Significant impairment in spatial and head-directional selectivity in GluA1^{C2KI} knock-in mice

When performing analysis including all recorded neurons, the GluA1^{C2KI} group exhibited a significant increase in the shuffle-subtracted spatial sparsity (Figure 3.27(b), day 1: 0.01 ± 0.01; day 6: 0.02 ± 0.01, p= 0.0117), and no significant changes in the shuffle-subtracted HD sparsity (Figure 3.27(d), day 1: 0.01 ± 0.01; day 6: 0.01 ± 0.01, p= 0.5454, see Figure 3.26 for sample cells). This is in contrast to recordings in control animals which demonstrated significant improvements in both spatial and HD shuffle-subtracted sparsity measurements across all cells recorded in both day 1 and day 6.

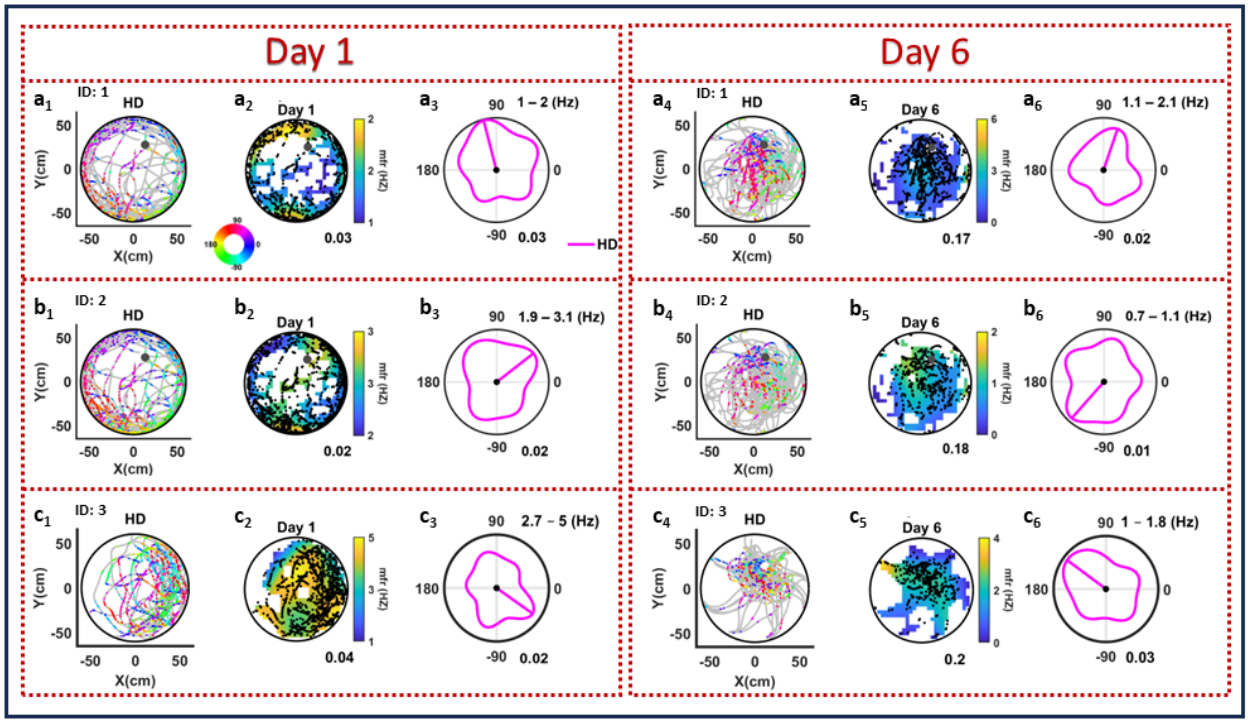

Figure 3.26: NO IMPROVEMENTS IN HEAD-DIRECTION SELECTIVITY IN GLUA1^{C2KI}
Three representative cells, recorded on both day 1 and day 6, are illustrated with their spiking activities, spatial, and head-directional rate maps. The examples highlight increased spatial selectivity with minimal changes in head-direction selectivity.

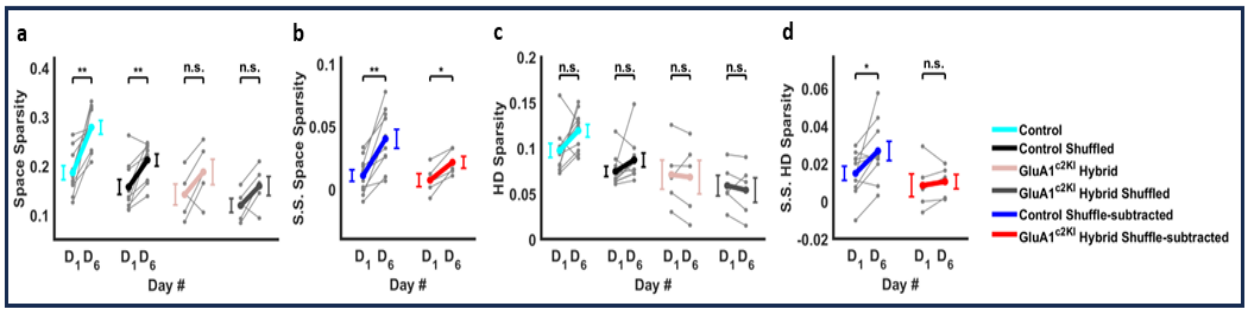

Figure 3.27: IMPAIRMENT IN HD SELECTIVITY AND INTACT SPATIAL SELECTIVITY ACROSS ALL CELLS BY LEARNING

See Figure 3.9 for the control group statistics. **(a)** No significant increase in the space sparsity (0.14 ± 0.02, day 6: 0.19 ± 0.03, paired sample t-test, $n = 5$, p= 0.1061), and no significant increase in the shuffled space sparsity (day 1: 0.12 ± 0.01; day 6: 0.16 ± 0.02, paired sample t-test, p= 0.0924). **(b)** Significant increase in the shuffle-subtracted space sparsity (day 1: 0.01 ± 0.01; day 6: 0.02 ± 0.01, paired sample t-test, p= 0.0117). **(c)** No significant increase in the HD sparsity (day 1: 0.07 ± 0.02; day 6: 0.07 ± 0.02, paired sample t-test, p= 0.7287), and no significant increase in the shuffled HD sparsity (day 1: 0.06 ± 0.01; day 6: 0.05 ± 0.01, paired sample t-test, p= 0.4829). **(d)** No significant increase in shuffle-subtracted HD sparsity (day 1: 0.01 ± 0.01; day 6: 0.01 ± 0.01, paired sample t-test, p= 0.5454). '*' p< 0.05, '**' p< 0.005, '***' p< 0.0005.

However, when considering only cells recorded on both day 1 and day 6, there was no significant increase in the shuffle-subtracted spatial sparsity (Figure 3.28(b), day 1: 0.01 ± 0.01; day 6: 0.02 ± 0.01, p= 0.3366), and no significant increase in the shuffle-subtracted HD sparsity (Figure 3.28(d), day 1: 0.01 ± 0.01; day 6: 0.01 ± 0.01, p= 0.4439). Therefore, animals with decreased CA1 LTP demonstrate a lack of improvement in spatial and HD sparsity, especially when comparing the same neurons across learning.

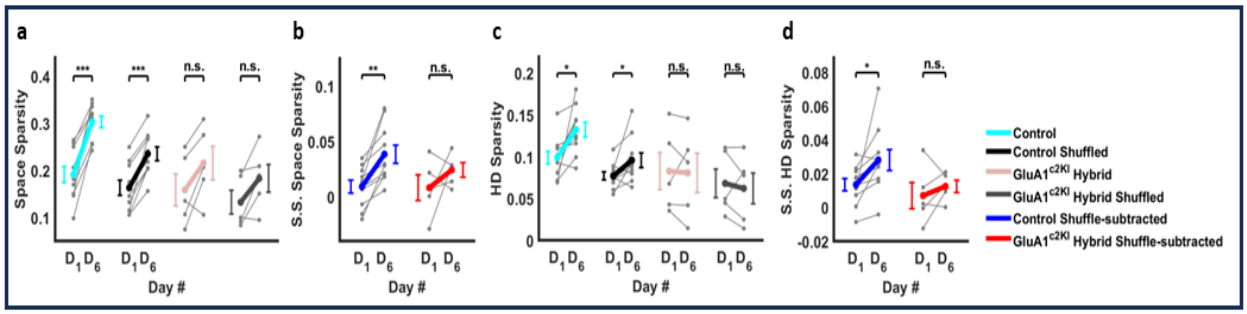

Figure 3.28: IMPAIRMENT IN HD AND SPATIAL SELECTIVITY ACROSS SHARED CELLS BY LEARNING

See Figure 3.10 for the control group statistics. **(a)** No significant increase in the space sparsity (day 1: 0.16 ± 0.03; day 6: 0.22 ± 0.04, paired sample t-test, n = 5, p= 0.0799), and no significant increase in shuffled space sparsity (day 1: 0.13 ± 0.03; day 6: 0.18 ± 0.03, paired sample t-test, p= 0.0688). **(b)** No significant increase in the shuffle-subtracted space sparsity (day 1: 0.01 ± 0.01; day 6: 0.02 ± 0.01, paired sample t-test, p= 0.3366). **(c)** No significant increase in the HD sparsity (day 1: 0.08 ± 0.02; day 6: 0.08 ± 0.02, paired sample t-test, p= 0.8668), and a no significant increase in the shuffled HD sparsity (day 1: 0.07 ± 0.02; day 6: 0.06 ± 0.02, paired sample t-test, p= 0.6014). **(d)** No significant increase in shuffle-subtracted HD sparsity (day 1: 0.01 ± 0.01; day 6: 0.01 ± 0.01, paired sample t-test, p= 0.4439). '*' p< 0.05, '**' p< 0.005, '***' p< 0.0005.

3.12 Decoding neural signals for the GluA1^{C2KI} animals

We conducted a comparative analysis of spatial, HD, and distance to goal decoding between the GluA1^{C2KI} animals and the control animals, employing identical neural networks and parameters as those used for the control group (see section 2.18, and Figures 3.29, 3.30, and 3.31).

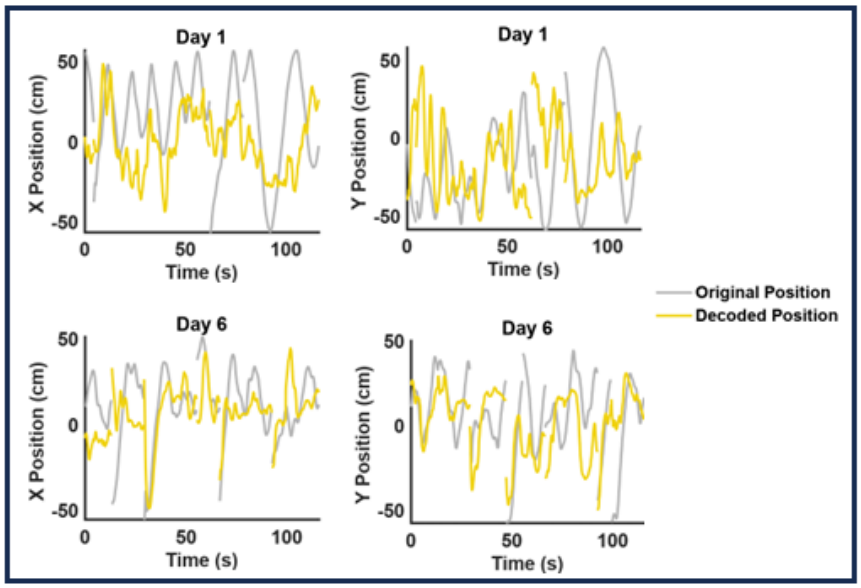

Figure 3.29: EXAMPLE DECODER RESULT FOR POSITION
Example of a decoding performance in predicting the position of a GluA1^{C2KI} animal. The grey line shows the original position trace and the yellow line represents the decoded position by FNN. The decoder's performance increased on day 6 compared to day 1.

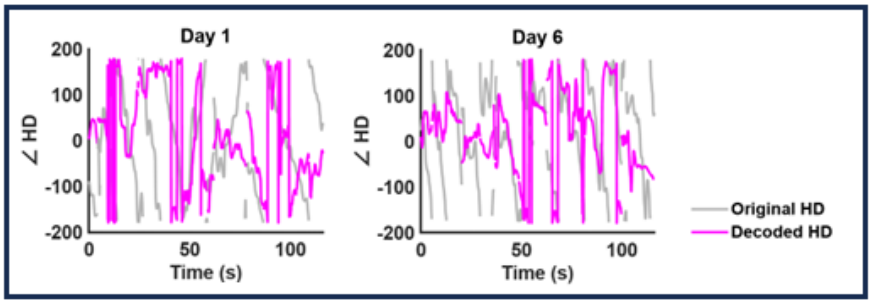

Figure 3.30: EXAMPLE DECODER RESULT FOR HEAD-DIRECTION
Example of a decoding performance in predicting the head-direction of a GluA1^{C2KI} animal. The grey line shows the original head-direction trace and the magenta line represents the decoded head-direction by FNN. The decoder's performance increased on day 6 compared to day 1.

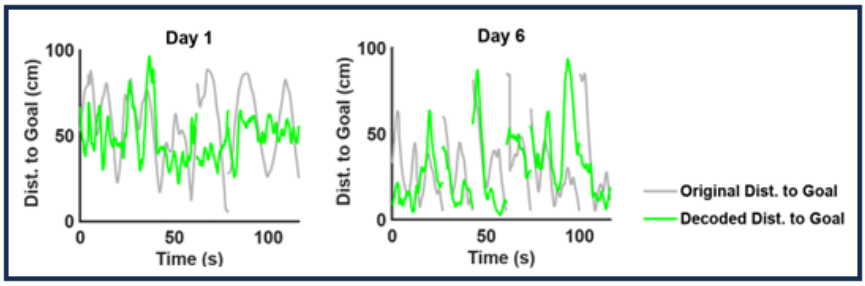

Figure 3.31: EXAMPLE DECODER RESULT FOR DISTANCE TO THE GOAL
Example of a decoding performance in predicting the distance to the platform of a GluA1^{C2KI} animal. The grey line shows the original distance to the platform trace and the green line represents the decoded distance to the platform by FNN. The decoder's performance increased on day 6 compared to day 1.

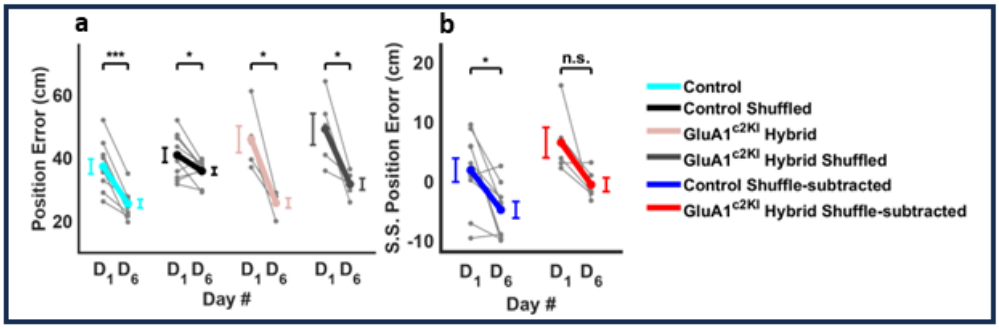

Figure 3.32: STRONG TREND FOR REDUCTION IN POSITION DECODING ERROR IN GLUA1^{C2KI} ANIMALS
The decoded position exhibited a significant decrease in error on day 6 compared to day 1. **(a)** The error for the empirical data demonstrated a significant drop (day 1: 45.9 ± 4.2, day 6: 25.8 ± 1.6 cm, paired sample t-test, n = 5, p= 0.0069). Likewise, the error for the shuffled data revealed a significant decrease (day 1: 49.1 ± 5.0, day 6: 31.8 ± 1.8 cm, paired sample t-test, p= 0.0254). **(b)** The reduction in the error for the shuffle-subtracted was no significant (day 1: 6.5 ± 2.6, day 6: −0.6 ± 1.2 cm, paired sample t-test, p= 0.0961).

While, the control group exhibited a significant reduction in both position error and shuffle-subtracted error, the GluA1^{C2KI} group only demonstrated a significant drop in position error (Figure 3.32(a), day 1: 45.9 ± 4.2, day 6: 25.8 ± 1.6 cm, p= 0.0069), while the shuffle-subtracted position error showed a similar trend without reaching statistical significance (Figure 3.32(b), day 1: 6.5±2.6, day 6: −0.6 ± 1.2 cm, p= 0.0961). Interestingly, both the control and GluA1^{C2KI} groups exhibited

a significant increase in the shuffle-subtracted position correlation coefficient (Figure 3.33(b), day 1: -0.20 ± 0.06, day 6: 0.07 ± 0.08, p= 0.0090).

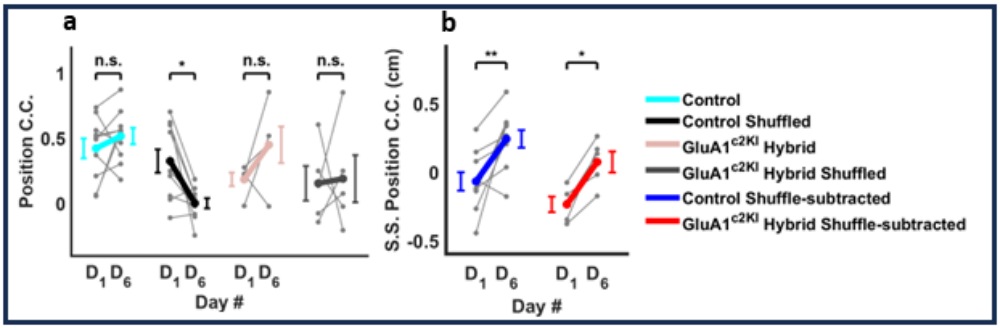

Figure 3.33: IMPROVEMENT IN POSITION DECODING CORRELATION
(a) There was no significant increase in the correlation between the empirical and decoded position (day 1: 0.19 ± 0.05, day 6: 0.45 ± 0.14, paired sample t-test, $n = 5$, p= 0.1644), and shuffled data also showed no significant increase (day 1: 0.16 ± 0.13, day 6: 0.19 ± 0.18, paired sample t-test, p= 0.90169). **(b)** The shuffle-subtracted data exhibits a significant increase (day 1: -0.20 ± 0.06, day 6: 0.07 ± 0.08, paired sample t-test, p= 0.0090).

On the other hand, there were dramatic differences in HD decoding between controls and mutant animals (Figure 3.34). Contrary to the control group, where there was a significant decrease in both HD decoding error and shuffle-subtracted HD error, the GluA1^{C2KI} animals did not exhibit a significant decrease in HD decoding error or subtracted HD error, instead showing a trend to increasing error (Figure 3.34(b), day 1: 0.6 ± 1.5, day 6: 9.4 ± 4.2, p= 0.0921). These findings are consistent with the single cell analysis showing no increase in HD sparsity in mutants.

Last, in contrast to improvements in distance to goal decoding that we observed in controls, there was no improvement in distance to the goal decoding error for the GluA1^{C2KI} group (Figure 3.35(a), day 1: 24.2 ± 3.3, day 6: 16.3 ± 1.0, p= 0.1078), and its shuffle-subtracted decoding error (Figure 3.35(b), day 1: 7.0 ± 4.1, day 6: 0.8 ± 1.5, p= 0.3023). Therefore, LTP impairment in CA1 resulted in failures to improve decoding of HD and distance to goal from CA1 activity that occur with learning in controls, suggesting that these changes depend on LTP and may be causally driving learning.

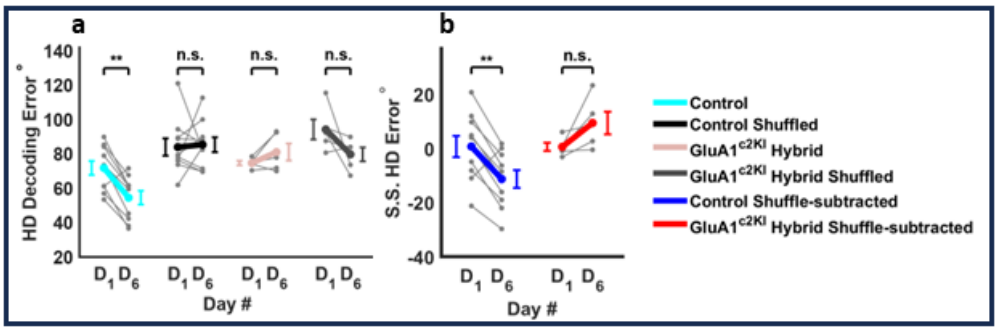

Figure 3.34: LACK OF IMPROVEMENT IN HEAD-DIRECTION DECODING THROUGH LEARNING

(a) The decoded head-direction error exhibited no significant increase on day 6 compared to day 1 (day 1: 74.7 ± 1.3, day 6: 81.1 ± 41.0, paired sample t-test, n = 5, p= 0.1885). Moreover, the error for the shuffled data revealed no significant decrease (day 1: 94.3 ± 5.9, day 6: 79.8 ± 4.1, paired sample t-test, p= 0.1557). **(b)** The error for the shuffle-subtracted also exhibited no significant increase on day 6 compared to day 1 (day 1: 0.6 ± 1.5, day 6: 9.4 ± 4.2, paired sample t-test, p= 0.0921).

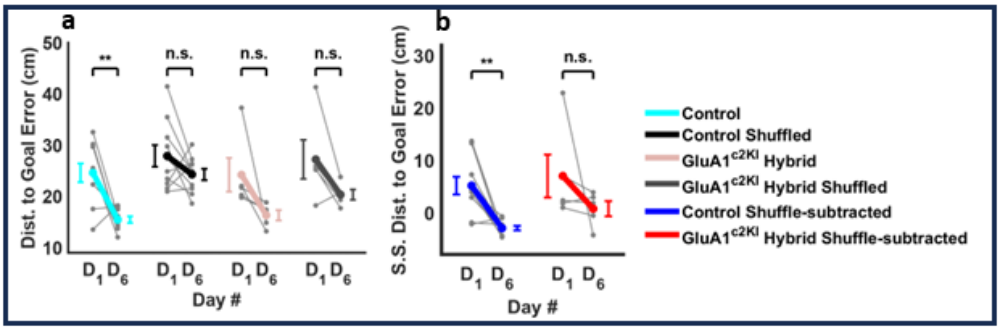

Figure 3.35: LACK OF SIGNIFICANT IMPROVEMENT IN DISTANCE TO THE PLATFORM DECODING THROUGH LEARNING

(a) The decoded distance to the platform exhibited no significant decrease in error on day 6 compared to day 1(day 1: 24.2 ± 3.3, day 6: 16.3 ± 1.0, paired sample t-test, n = 5, p= 0.1078). Additionally, the error for the shuffled data revealed no significant decrease (day 1: 27.2 ± 3.8, day 6: 20.4 ± 1.0, paired sample t-test, p= 0.0979). **(b)** The error for the shuffle-subtracted exhibited no significant reduction (day 1: 7.0 ± 4.1, day 6: 0.8 ± 1.5, paired sample t-test, p= 0.3023).

3.13 Position and head-direction conjunctive analysis for GluA1^{C2KI} animals

Our analysis of place/HD conjunctions revealed a significant increase in the percentage of active cells from day 1 to day 6 as the animals acquired the task, as depicted in Figure 3.36 (a) (p= 0.0021). However, there were no significant changes in the average amplitude of calcium signals for the activated neurons during this learning period (Figure 3.36 (b), p= 0.4956). Notably, when restricting the analysis to data within the speed range of 10–25 cm/s, there was no significant difference in speed observed between day 1 and day 6 (Figure 3.36 (c), p= 0.7554).

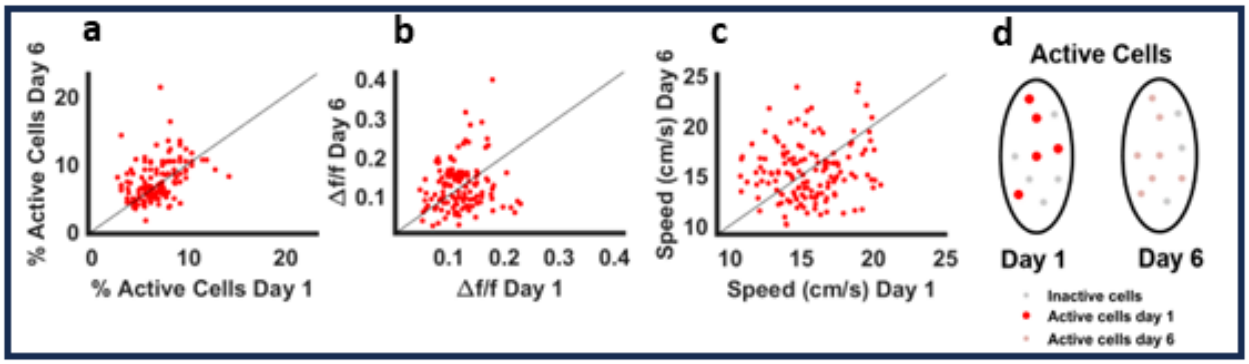

Figure 3.36: INCREASE IN THE PERCENTAGE OF ACTIVE CELLS AFTER LEARNING FOR GLUA1^{C2KI} ANIMALS
Exploring neural activity within similar positions and head directions on both day 1 and day 6. **(a)** The percentage of active cells experienced a significant increase from day 1 to day 6 (day 1: 6.7% ± 2.1% ($\mu \pm \sigma$), day 6: 7.4% ± 3.0%, paired sample t-test, $n_{animals}$= 5, p= 0.0021). **(b)** There were no significant changes in fluorescence intensity changes (day 1: 0.12 ± 0.04, day 6: 0.12 ± 0.06, paired sample t-test, p= 0.4956). **(c)** There were no significant differences in speed from day 1 to day 6 (day 1: 15.5 ± 2.4 (cm/sec), day 6: 15.4 ± 2.9 (cm/sec), paired sample t-test, p= 0.7554) S. **(d)** Summarizes the conjunctive analysis. Inactive cells, depicted by gray circles, contrast with active cells highlighted in color. A visible increase in the percentage of active cells from day 1 to day 6 is reflected by the increased number of colored circles observed on day 6.

3.14 Discussion

The present study marks a significant advancement in our understanding of neural activity during spatial learning tasks, particularly through the innovative use of miniscope technology to observe

calcium transient activity in hundreds of neurons simultaneously. By employing this technique during the MWM navigation task, we were able to longitudinally track neural responses and correlate them with behavioral changes as animals acquired the task.

Initially, wild-type animals exhibited longer and less direct paths to locate the hidden platform, indicative of a lack of familiarity with the task. However, as learning progressed, we observed significant shorter, more efficient paths, accompanied by a reduction in trial escape latency, a classical marker of task proficiency. Additionally, during probe trials where the platform was removed, animals displayed a preference for the quadrant where the platform was previously located, as evidenced by increased time spent and higher frequency of target crossings in that area.

To decipher the neural mechanisms underlying this learning process, we employed a generalized linear model to analyze single-cell responses, considering spatial and head directional tuning. Given the inherent biases in animal behavior within the MWM task, this statistical framework was essential for accurately disentangling the effects of head direction and position on neuronal firing rates. Our results revealed a significant enhancement in sparsity of both spatial and head-directional firing rate over the learning period, indicating a refinement of neuronal representations associated with task performance.

Furthermore, employing artificial neural networks, we successfully decoded positional, directional, and distance to platform information from neural activity patterns, with decoding errors markedly decreasing as animals became proficient in the task. Additionally, correlations between decoded and actual positions strengthened with learning, further supporting the accuracy of neural representations.

Subsequent investigations into the role of LTP in task learning involved experiments with $GluA1^{C2KI}$ mutant mice, known to exhibit impaired LTP and learning deficits. While these mice displayed a learning-related reduction in trial escape latencies similar to controls, probe trial analysis failed to reveal significant differences in quadrant preferences, suggesting learning impairment.

Single-cell and network analyses in $GluA1^{C2KI}$ mice did not demonstrate improvements in HD

and distance coding observed in wild-type mice, indicating a potential role of LTP in refining neural representations associated with task learning.

Our findings were built upon previous studies examining hippocampal involvement in goal-directed navigation. For instance, Hollup et al. demonstrated an accumulation of place fields near the goal during probe trials, indicative of memory encoding for goal location [HMD01]. Similarly, Dupret et al. observed reorganization of place fields near the goal in a 2D maze, both during learning and probe trials [DOP10]. However, these studies did not elucidate the neural changes underlying the actual navigation to goal locations. Our study addressed this gap by revealing improved place and head direction coding during navigation learning. This fills a crucial void by exploring neural changes directly tied to goal navigation.

Kentros et al. (2004) made a significant discovery regarding the stability of single place cells across sessions where mice navigated towards a goal using distal cues, compared to sessions without goal navigation amidst noise and flashing lights in a 2D arena. They found that place cell responses were stable in goal-directed sessions but unstable otherwise, highlighting the role of attention to cues in creating stable place cell maps correlated with successful navigation [KAS04].

These findings did not elucidate the neural changes crucial for goal-directed navigation, as the stability analysis mostly pertains to periods when animals are random foraging rather than navigating towards the goal from different starting points. Kentros et al.'s results implied that attention to cues generates a stable place cell map correlated with successful goal navigation. Our study, in contrast, revealed enhanced place coding during the learning of 2D navigation towards the goal, providing deeper insights into the neural processes involved in successful goal-oriented navigation.

Our findings also provide additional insights into a study by Moore et al. (2021), which investigated neural responses during 2D navigation in virtual reality towards a hidden goal and their changes with learning. Aligning with our day-to-day learning results, Moore et al. demonstrated enhanced decoding of the CA1 population for head direction within the same learning session [MCA21].

Furthermore, our study with LTP-deficient mice revealed that the absence of improvement in head direction coding during learning correlated with reduced accuracy in goal navigation during probe trials. These combined results further support the significance of CA1 head direction coding in 2D goal navigation, reinforcing the importance of these neural mechanisms in spatial orientation tasks.

REFERENCES

[AAV16] Lavanya Acharya, Zahra M Aghajan, Cliff Vuong, Jason J Moore, and Mayank R Mehta. "Causal influence of visual cues on hippocampal directional selectivity." *Cell*, **164**(1):197–207, 2016.

[And13] John R Anderson. *The architecture of cognition*. Psychology Press, 2013.

[BFW11] Tracy A Bedrosian, Laura K Fonken, James C Walton, Abraham Haim, and Randy J Nelson. "Dim light at night provokes depression-like behaviors and reduces CA1 dendritic spine density in female hamsters." *Psychoneuroendocrinology*, **36**(7):1062–1069, 2011.

[BKS07] Daniel A Butts, Patrick O Kanold, and Carla J Shatz. "A burst-based "Hebbian" learning rule at retinogeniculate synapses links retinal waves to activity-dependent refinement." *PLoS biology*, **5**(3):e61, 2007.

[BLH06] Caswell Barry, Colin Lever, Robin Hayman, Tom Hartley, Stephen Burton, John O'Keefe, Kate Jeffery, and N Burgess. "The boundary vector cell model of place cell firing and spatial memory." *Reviews in the Neurosciences*, **17**(1-2):71–98, 2006.

[BMG17] Katie C Bittner, Aaron D Milstein, Christine Grienberger, Sandro Romani, and Jeffrey C Magee. "Behavioral time scale synaptic plasticity underlies CA1 place fields." *Science*, **357**(6355):1033–1036, 2017.

[BP98] Guo-qiang Bi and Mu-ming Poo. "Synaptic modifications in cultured hippocampal neurons: dependence on spike timing, synaptic strength, and postsynaptic cell type." *Journal of neuroscience*, **18**(24):10464–10472, 1998.

[BSM04] Francesco P Battaglia, Gary R Sutherland, and Bruce L McNaughton. "Local sensory cues and place cell directionality: additional evidence of prospective coding in the hippocampus." *Journal of Neuroscience*, **24**(19):4541–4550, 2004.

[BSM16] David Berron, Hartmut Schütze, Anne Maass, Arturo Cardenas-Blanco, Hugo J Kuijf, Dharshan Kumaran, and Emrah Düzel. "Strong evidence for pattern separation in human dentate gyrus." *Journal of Neuroscience*, **36**(29):7569–7579, 2016.

[BWF09] Joachim Behr, Christian Wozny, Pawel Fidzinski, and Dietmar Schmitz. "Synaptic plasticity in the subiculum." *Progress in neurobiology*, **89**(4):334–342, 2009.

[CAS16] Denise J Cai, Daniel Aharoni, Tristan Shuman, Justin Shobe, Jeremy Biane, Weilin Song, Brandon Wei, Michael Veshkini, Mimi La-Vu, Jerry Lou, et al. "A shared neural ensemble links distinct contextual memories encoded close in time." *Nature*, **534**(7605):115–118, 2016.

[CB10] Sam F Cooke and Mark F Bear. "Visual experience induces long-term potentiation in the primary visual cortex." *Journal of Neuroscience*, **30**(48):16304–16313, 2010.

[DOP10] David Dupret, Joseph O'neill, Barty Pleydell-Bouverie, and Jozsef Csicsvari. "The reorganization and reactivation of hippocampal maps predict spatial memory performance." *Nature neuroscience*, **13**(8):995–1002, 2010.

[Eic00] Howard Eichenbaum. "A cortical–hippocampal system for declarative memory." *Nature reviews neuroscience*, **1**(1):41–50, 2000.

[Eic17] Howard Eichenbaum. "Prefrontal–hippocampal interactions in episodic memory." *Nature Reviews Neuroscience*, **18**(9):547–558, 2017.

[EPB98] Peter S Eriksson, Ekaterina Perfilieva, Thomas Björk-Eriksson, Ann-Marie Alborn, Claes Nordborg, Daniel A Peterson, and Fred H Gage. "Neurogenesis in the adult human hippocampus." *Nature medicine*, **4**(11):1313–1317, 1998.

[EPJ17] Russell A Epstein, Eva Zita Patai, Joshua B Julian, and Hugo J Spiers. "The cognitive map in humans: spatial navigation and beyond." *Nature neuroscience*, **20**(11):1504–1513, 2017.

[FZP17] Johannes Friedrich, Pengcheng Zhou, and Liam Paninski. "Fast online deconvolution of calcium imaging data." *PLoS computational biology*, **13**(3):e1005423, 2017.

[GAC10] Stephen D Ginsberg, Melissa J Alldred, Scott E Counts, Anne M Cataldo, Rachael L Neve, Ying Jiang, Joanne Wuu, Moses V Chao, Elliott J Mufson, Ralph A Nixon, et al. "Microarray analysis of hippocampal CA1 neurons implicates early endosomal dysfunction during Alzheimer's disease progression." *Biological psychiatry*, **68**(10):885–893, 2010.

[GB09] Paul E Gilbert and Andrea M Brushfield. "The role of the CA3 hippocampal subregion in spatial memory: a process oriented behavioral assessment." *Progress in Neuro-Psychopharmacology and Biological Psychiatry*, **33**(5):774–781, 2009.

[GBC11] Kunal K Ghosh, Laurie D Burns, Eric D Cocker, Axel Nimmerjahn, Yaniv Ziv, Abbas El Gamal, and Mark J Schnitzer. "Miniaturized integration of a fluorescence microscope." *Nature methods*, **8**(10):871–878, 2011.

[GBC20] Joshua I Glaser, Ari S Benjamin, Raeed H Chowdhury, Matthew G Perich, Lee E Miller, and Konrad P Kording. "Machine learning for neural decoding." *Eneuro*, **7**(4), 2020.

[GBD97] John DE Gabrieli, James B Brewer, John E Desmond, and Gary H Glover. "Separate neural bases of two fundamental memory processes in the human medial temporal lobe." *Science*, **276**(5310):264–266, 1997.

[GK06] Paul E Gilbert and Raymond P Kesner. "The role of the dorsal CA3 hippocampal subregion in spatial working memory and pattern separation." *Behavioural brain research*, **169**(1):142–149, 2006.

[GMD06] Agnès Gruart, María Dolores Muñoz, and José M Delgado-García. "Involvement of the CA3–CA1 synapse in the acquisition of associative learning in behaving mice." *Journal of Neuroscience*, **26**(4):1077–1087, 2006.

[GOK92] Seth GN Grant, Thomas J O'dell, Kevin A Karl, Paul L Stein, Philippe Soriano, and Eric R Kandel. "Impaired long-term potentiation, spatial learning, and hippocampal development in fyn mutant mice." *Science*, **258**(5090):1903–1910, 1992.

[GPT85] Grzegorz Grynkiewicz, Martin Poenie, and Roger Y Tsien. "A new generation of Ca2+ indicators with greatly improved fluorescence properties." *Journal of biological chemistry*, **260**(6):3440–3450, 1985.

[GRG99] Elizabeth Gould, Alison J Reeves, Michael SA Graziano, and Charles G Gross. "Neurogenesis in the neocortex of adult primates." *Science*, **286**(5439):548–552, 1999.

[GSB14] Lisa M Giocomo, Tor Stensola, Tora Bonnevie, Tiffany Van Cauter, May-Britt Moser, and Edvard I Moser. "Topography of head direction cells in medial entorhinal cortex." *Current Biology*, **24**(3):252–262, 2014.

[Heb05] Donald Olding Hebb. *The organization of behavior: A neuropsychological theory*. Psychology press, 2005.

[HFM05] Torkel Hafting, Marianne Fyhn, Sturla Molden, May-Britt Moser, and Edvard I Moser. "Microstructure of a spatial map in the entorhinal cortex." *Nature*, **436**(7052):801–806, 2005.

[HMD01] Stig A Hollup, Sturla Molden, James G Donnett, May-Britt Moser, and Edvard I Moser. "Accumulation of hippocampal place fields at the goal location in an annular watermaze task." *Journal of Neuroscience*, **21**(5):1635–1644, 2001.

[HS09] Anthony Holtmaat and Karel Svoboda. "Experience-dependent structural synaptic plasticity in the mammalian brain." *Nature Reviews Neuroscience*, **10**(9):647–658, 2009.

[HS14] Frederick L Hitti and Steven A Siegelbaum. "The hippocampal CA2 region is essential for social memory." *Nature*, **508**(7494):88–92, 2014.

[HSA19] Øyvind Arne Høydal, Emilie Ranheim Skytøen, Sebastian Ola Andersson, May-Britt Moser, and Edvard I Moser. "Object-vector coding in the medial entorhinal cortex." *Nature*, **568**(7752):400–404, 2019.

[KAS04] Clifford G Kentros, Naveen T Agnihotri, Samantha Streater, Robert D Hawkins, and Eric R Kandel. "Increased attention to spatial context increases both place field stability and spatial memory." *Neuron*, **42**(2):283–295, 2004.

[KCM15] Emilio Kropff, James E Carmichael, May-Britt Moser, and Edvard I Moser. "Speed cells in the medial entorhinal cortex." *Nature*, **523**(7561):419–424, 2015.

[KHW08] Raymond P Kesner, Michael R Hunsaker, and Matthew W Warthen. "The CA3 subregion of the hippocampus is critical for episodic memory processing by means of relational encoding in rats." *Behavioral neuroscience*, **122**(6):1217, 2008.

[KMS20] Nathaniel R Kinsky, William Mau, David W Sullivan, Samuel J Levy, Evan A Ruesch, and Michael E Hasselmo. "Trajectory-modulated hippocampal neurons persist throughout memory-guided navigation." *Nature communications*, **11**(1):2443, 2020.

[KTW07] Nohjin Kee, Cátia M Teixeira, Afra H Wang, and Paul W Frankland. "Preferential incorporation of adult-generated granule cells into spatial memory networks in the dentate gyrus." *Nature neuroscience*, **10**(3):355–362, 2007.

[LBJ09] Colin Lever, Stephen Burton, Ali Jeewajee, John O'Keefe, and Neil Burgess. "Boundary vector cells in the subiculum of the hippocampal formation." *Journal of Neuroscience*, **29**(31):9771–9777, 2009.

[LL07] Stefan Leutgeb and Jill K Leutgeb. "Pattern separation, pattern completion, and new neuronal codes within a continuous CA3 map." *Learning & memory*, **14**(11):745–757, 2007.

[LME12] Kyle Q Lepage, Christopher J MacDonald, Howard Eichenbaum, and Uri T Eden. "The statistical analysis of partially confounded covariates important to neural spiking." *Journal of neuroscience methods*, **205**(2):295–304, 2012.

[LRM00] Stefan Leutgeb, Katherine E Ragozzino, and Sheri JY Mizumori. "Convergence of head direction and place information in the CA1 region of hippocampus." *Neuroscience*, **100**(1):11–19, 2000.

[LSL07] Lusha Liu, S Charles Schulz, Susanne Lee, Teri J Reutiman, and S Hossein Fatemi. "Hippocampal CA1 pyramidal cell size is reduced in bipolar disorder." *Cellular and molecular neurobiology*, **27**:351–358, 2007.

[MAL86] RGM Morris, Elizabeth Anderson, GS a Lynch, and Michel Baudry. "Selective impairment of learning and blockade of long-term potentiation by an N-methyl-D-aspartate receptor antagonist, AP5." *Nature*, **319**(6056):774–776, 1986.

[MBM94] Etan J Markus, Carol A Barnes, Bruce L McNaughton, Victoria L Gladden, and William E Skaggs. "Spatial information content and reliability of hippocampal CA1 neurons: effects of visual input." *Hippocampus*, **4**(4):410–421, 1994.

[MBT96] Thomas J McHugh, Kenneth I Blum, Joe Z Tsien, Susumu Tonegawa, and Matthew A Wilson. "Impaired hippocampal representation of space in CA1-specific NMDAR1 knockout mice." *Cell*, **87**(7):1339–1349, 1996.

[MCA20] Thomas D Miller, Trevor TJ Chong, Anne M Aimola Davies, Michael R Johnson, Sarosh R Irani, Masud Husain, Tammy WC Ng, Saiju Jacob, Paul Maddison, Christopher Kennard, et al. "Human hippocampal CA3 damage disrupts both recent and remote episodic memories." *Elife*, **9**:e41836, 2020.

[MCA21] Jason J Moore, Jesse D Cushman, Lavanya Acharya, Briana Popeney, and Mayank R Mehta. "Linking hippocampal multiplexed tuning, Hebbian plasticity and navigation." *Nature*, **599**(7885):442–448, 2021.

[MCT68] B Milner, S Corkin, and HL Teuber. "Further analysis of the hippocampal amnesic syndrome: 14-year follow-up study of HM Neuropsychologia, 6 (3), 215–234.", 1968.

[MF11] G MacQueen and Thomas Frodl. "The hippocampus in major depression: evidence for the convergence of the bench and bedside in psychiatric research?" *Molecular psychiatry*, **16**(3):252–264, 2011.

[Mil70] Brenda Milner. "Memory and the medial temporal regions of the brain." *Biology of memory*, **23**:31–59, 1970.

[MK87] Robert U Muller and John L Kubie. "The effects of changes in the environment on the spatial firing of hippocampal complex-spike cells." *Journal of Neuroscience*, **7**(7):1951–1968, 1987.

[MKM08] Edvard I Moser, Emilio Kropff, and May-Britt Moser. "Place cells, grid cells, and the brain's spatial representation system." *Annu. Rev. Neurosci.*, **31**:69–89, 2008.

[MLB18] Torcato Meira, Felix Leroy, Eric W Buss, Azahara Oliva, Jung Park, and Steven A Siegelbaum. "A hippocampal circuit linking dorsal CA2 to ventral CA1 critical for social memory dynamics." *Nature communications*, **9**(1):4163, 2018.

[MLB21] Aaron D Milstein, Yiding Li, Katie C Bittner, Christine Grienberger, Ivan Soltesz, Jeffrey C Magee, and Sandro Romani. "Bidirectional synaptic plasticity rapidly modifies hippocampal representations." *Elife*, **10**:e73046, 2021.

[MLE11] Christopher J MacDonald, Kyle Q Lepage, Uri T Eden, and Howard Eichenbaum. "Hippocampal "time cells" bridge the gap in memory for discontiguous events." *Neuron*, **71**(4):737–749, 2011.

[MM98] May-Britt Moser and Edvard I Moser. "Functional differentiation in the hippocampus." *Hippocampus*, **8**(6):608–619, 1998.

[Mor89] RG Morris. "Synaptic plasticity and learning: selective impairment of learning rats and blockade of long-term potentiation in vivo by the N-methyl-D-aspartate receptor antagonist AP5." *Journal of Neuroscience*, **9**(9):3040–3057, 1989.

[MQL95] Etan J Markus, Yu-Lin Qin, Brian Leonard, William E Skaggs, Bruce L McNaughton, and Carol A Barnes. "Interactions between location and task affect the spatial and directional firing of hippocampal neurons." *Journal of Neuroscience*, **15**(11):7079–7094, 1995.

[MST90] RGM Morris, F Schenk, F Tweedie, and LE Jarrard. "Ibotenate lesions of hippocampus and/or subiculum: dissociating components of allocentric spatial learning." *European Journal of Neuroscience*, **2**(12):1016–1028, 1990.

[MW93] SJ Mizumori and John D Williams. "Directionally selective mnemonic properties of neurons in the lateral dorsal nucleus of the thalamus of rats." *Journal of Neuroscience*, **13**(9):4015–4028, 1993.

[Nel00] Charles A Nelson. "Neural plasticity and human development: The role of early experience in sculpting memory systems." *Developmental Science*, **3**(2):115–136, 2000.

[NOI01] Junichi Nakai, Masamichi Ohkura, and Keiji Imoto. "A high signal-to-noise Ca2+ probe composed of a single green fluorescent protein." *Nature biotechnology*, **19**(2):137–141, 2001.

[NPJ99] Michael Nilsson, Ekaterina Perfilieva, Ulf Johansson, Owe Orwar, and Peter S Eriksson. "Enriched environment increases neurogenesis in the adult rat dentate gyrus and improves spatial memory." *Journal of neurobiology*, **39**(4):569–578, 1999.

[NSL16] Jeffrey P Nguyen, Frederick B Shipley, Ashley N Linder, George S Plummer, Mochi Liu, Sagar U Setru, Joshua W Shaevitz, and Andrew M Leifer. "Whole-brain calcium imaging with cellular resolution in freely behaving Caenorhabditis elegans." *Proceedings of the National Academy of Sciences*, **113**(8):E1074–E1081, 2016.

[OD71] John O'Keefe and Jonathan Dostrovsky. "The hippocampus as a spatial map: preliminary evidence from unit activity in the freely-moving rat." *Brain research*, 1971.

[OM06] Shane O'Mara. "Controlling hippocampal output: the central role of subiculum in hippocampal information processing." *Behavioural brain research*, **174**(2):304–312, 2006.

[ON79] John O'keefe and Lynn Nadel. "Précis of O'Keefe & Nadel's The hippocampus as a cognitive map." *Behavioral and Brain Sciences*, **2**(4):487–494, 1979.

[OSB09] Shane M O'Mara, Maria V Sanchez-Vives, Jorge R Brotons-Mas, and Eugene O'Hare. "Roles for the subiculum in spatial information processing, memory, motivation and the temporal control of behaviour." *Progress in Neuro-Psychopharmacology and Biological Psychiatry*, **33**(5):782–790, 2009.

[PAF05] Alvaro Pascual-Leone, Amir Amedi, Felipe Fregni, and Lotfi B Merabet. "The plastic human brain cortex." *Annu. Rev. Neurosci.*, **28**:377–401, 2005.

[PG17] Eftychios A Pnevmatikakis and Andrea Giovannucci. "NoRMCorre: An online algorithm for piecewise rigid motion correction of calcium imaging data." *Journal of neuroscience methods*, **291**:83–94, 2017.

[QMK90] Gregory J Quirk, Robert U Muller, and John L Kubie. "The firing of hippocampal place cells in the dark depends on the rat's recent experience." *Journal of Neuroscience*, **10**(6):2008–2017, 1990.

[RDR20] Nick TM Robinson, Lucie AL Descamps, Lloyd E Russell, Moritz O Buchholz, Brendan A Bicknell, Georgy K Antonov, Joanna YN Lau, Rebecca Nutbrown, Christoph Schmidt-Hieber, and Michael Häusser. "Targeted activation of hippocampal place cells drives memory-guided spatial behavior." *Cell*, **183**(6):1586–1599, 2020.

[RKW13] Pascal Ravassard, Ashley Kees, Bernard Willers, David Ho, Daniel Aharoni, Jesse Cushman, Zahra M Aghajan, and Mayank R Mehta. "Multisensory control of hippocampal spatiotemporal selectivity." *Science*, **340**(6138):1342–1346, 2013.

[SAC20] Tristan Shuman, Daniel Aharoni, Denise J Cai, Christopher R Lee, Spyridon Chavlis, Lucia Page-Harley, Lauren M Vetere, Yu Feng, Chen Yi Yang, Irene Mollinedo-Gajate, et al. "Breakdown of spatial coding and interneuron synchronization in epileptic mice." *Nature neuroscience*, **23**(2):229–238, 2020.

[SB15] Hugo J Spiers and Caswell Barry. "Neural systems supporting navigation." *Current opinion in behavioral sciences*, **1**:47–55, 2015.

[SBH01] Hugo J Spiers, Neil Burgess, Tom Hartley, Faraneh Vargha-Khadem, and John O'Keefe. "Bilateral hippocampal pathology impairs topographical and episodic memory but not visual pattern matching." *Hippocampus*, **11**(6):715–725, 2001.

[SBK08] Trygve Solstad, Charlotte N Boccara, Emilio Kropff, May-Britt Moser, and Edvard I Moser. "Representation of geometric borders in the entorhinal cortex." *Science*, **322**(5909):1865–1868, 2008.

[SFL17] Ayelet Sarel, Arseny Finkelstein, Liora Las, and Nachum Ulanovsky. "Vectorial representation of spatial goals in the hippocampus of bats." *Science*, **355**(6321):176–180, 2017.

[SFM97] Alcino J Silva, Paul W Frankland, Zachary Marowitz, Eugenia Friedman, George Lazlo, Dianna Cioffi, Tyler Jacks, and Roussoudan Bourtchuladze. "A mouse model for the learning and memory deficits associated with neurofibromatosis type I." *Nature genetics*, **15**(3):281–284, 1997.

[SGN09] Bechara J Saab, John Georgiou, Arup Nath, Frank JS Lee, Min Wang, Aubin Michalon, Fang Liu, Isabelle M Mansuy, and John C Roder. "NCS-1 in the dentate gyrus promotes exploration, synaptic plasticity, and rapid acquisition of spatial memory." *Neuron*, **63**(5):643–656, 2009.

[SKI95] Kenji Sakimura, Tatsuya Kutsuwada, Isao Ito, Toshiya Manabe, Chitoshi Takayama, Etsuko Kushiya, Takeshi Yagi, Shinichi Aizawa, Yoshiro Inoue, Hiroyuki Sugiyama, et al. "Reduced hippocampal LTP and spatial learning in mice lacking NMDA receptor $\varepsilon 1$ subunit." *Nature*, **373**(6510):151–155, 1995.

[SM57] William Beecher Scoville and Brenda Milner. "Loss of recent memory after bilateral hippocampal lesions." *Journal of neurology, neurosurgery, and psychiatry*, **20**(1):11, 1957.

[SM85] F Schenk and RGM Morris. "Dissociation between components of spatial memory in rats after recovery from the effects of retrohippocampal lesions." *Experimental Brain Research*, **58**:11–28, 1985.

[SMM12] Brandy Schmidt, Diano F Marrone, and Etan J Markus. "Disambiguating the similar: the dentate gyrus and pattern separation." *Behavioural brain research*, **226**(1):56–65, 2012.

[SPS07] Stephen William Scheff, Douglas A Price, Frederick A Schmitt, ST DeKosky, and Elliott J Mufson. "Synaptic alterations in CA1 in mild Alzheimer disease and mild cognitive impairment." *Neurology*, **68**(18):1501–1508, 2007.

[SPW92] Alcino J Silva, Richard Paylor, Jeanne M Wehner, and Susumu Tonegawa. "Impaired spatial learning in α-calcium-calmodulin kinase II mutant mice." *Science*, **257**(5067):206–211, 1992.

[Squ92] Larry R Squire. "Memory and the hippocampus: a synthesis from findings with rats, monkeys, and humans." *Psychological review*, **99**(2):195, 1992.

[SRB17] Liron Sheintuch, Alon Rubin, Noa Brande-Eilat, Nitzan Geva, Noa Sadeh, Or Pinchasof, and Yaniv Ziv. "Tracking the same neurons across multiple days in Ca2+ imaging data." *Cell reports*, **21**(4):1102–1115, 2017.

[SSM02] Hill-Aina Steffenach, Robert S Sloviter, Edvard I Moser, and May-Britt Moser. "Impaired retention of spatial memory after transection of longitudinally oriented axons of hippocampal CA3 pyramidal cells." *Proceedings of the National Academy of Sciences*, **99**(5):3194–3198, 2002.

[SW11] Larry R Squire and John T Wixted. "The cognitive neuroscience of human memory since HM." *Annual review of neuroscience*, **34**:259–288, 2011.

[SWC16] Adam S Smith, SK Williams Avram, Adi Cymerblit-Sabba, June Song, and W Scott Young. "Targeted activation of the hippocampal CA2 area strongly enhances social memory." *Molecular psychiatry*, **21**(8):1137–1144, 2016.

[SY06] Karel Svoboda and Ryohei Yasuda. "Principles of two-photon excitation microscopy and its applications to neuroscience." *Neuron*, **50**(6):823–839, 2006.

[SYK08] Francesco Savelli, D Yoganarasimha, and James J Knierim. "Influence of boundary removal on the spatial representations of the medial entorhinal cortex." *Hippocampus*, **18**(12):1270–1282, 2008.

[Tau95] Jeffrey S Taube. "Head direction cells recorded in the anterior thalamic nuclei of freely moving rats." *Journal of Neuroscience*, **15**(1):70–86, 1995.

[TEF05] Wilson Truccolo, Uri T Eden, Matthew R Fellows, John P Donoghue, and Emery N Brown. "A point process framework for relating neural spiking activity to spiking history, neural ensemble, and extrinsic covariate effects." *Journal of neurophysiology*, **93**(2):1074–1089, 2005.

[THM09] Lin Tian, S Andrew Hires, Tianyi Mao, Daniel Huber, M Eugenia Chiappe, Sreekanth H Chalasani, Leopoldo Petreanu, Jasper Akerboom, Sean A McKinney, Eric R Schreiter, et al. "Imaging neural activity in worms, flies and mice with improved GCaMP calcium indicators." *Nature methods*, **6**(12):875–881, 2009.

[THT96] Joe Z Tsien, Patricio T Huerta, and Susumu Tonegawa. "The essential role of hippocampal CA1 NMDA receptor–dependent synaptic plasticity in spatial memory." *Cell*, **87**(7):1327–1338, 1996.

[TMR90] Jeffrey S Taube, Robert U Muller, and James B Ranck. "Head-direction cells recorded from the postsubiculum in freely moving rats. I. Description and quantitative analysis." *Journal of Neuroscience*, **10**(2):420–435, 1990.

[TN04] Gina G Turrigiano and Sacha B Nelson. "Homeostatic plasticity in the developing nervous system." *Nature reviews neuroscience*, **5**(2):97–107, 2004.

[TPD20] Jiannis Taxidis, Eftychios A Pnevmatikakis, Conor C Dorian, Apoorva L Mylavarapu, Jagmeet S Arora, Kian D Samadian, Emily A Hoffberg, and Peyman Golshani. "Differential emergence and stability of sensory and temporal representations in context-specific hippocampal sequences." *Neuron*, **108**(5):984–998, 2020.

[TWP21] Sijue Tao, Yihang Wang, Jundan Peng, Yang Zhao, Xiaobin He, Xuefeng Yu, Qing Liu, Sen Jin, and Fuqiang Xu. "Whole-brain mapping the direct inputs of dorsal and ventral CA1 projection neurons." *Frontiers in neural circuits*, **15**:643230, 2021.

[Wal15] Matthew Charles Walker. "Hippocampal sclerosis: causes and prevention." In *Seminars in neurology*, volume 35, pp. 193–200. Thieme Medical Publishers, 2015.

[WMS17] Andrew M Wikenheiser, Yasmin Marrero-Garcia, and Geoffrey Schoenbaum. "Suppression of ventral hippocampal output impairs integrated orbitofrontal encoding of task structure." *Neuron*, **95**(5):1197–1207, 2017.

[YLS11] Michael A Yassa, Joyce W Lacy, Shauna M Stark, Marilyn S Albert, Michela Gallagher, and Craig EL Stark. "Pattern separation deficits associated with increased hippocampal CA3 and dentate gyrus activity in nondemented older adults." *Hippocampus*, **21**(9):968–979, 2011.

[ZL03] Wei Zhang and David J Linden. "The other side of the engram: experience-driven changes in neuronal intrinsic excitability." *Nature Reviews Neuroscience*, **4**(11):885–900, 2003.

[ZLX18] Zikai Zhou, An Liu, Shuting Xia, Celeste Leung, Junxia Qi, Yanghong Meng, Wei Xie, Pojeong Park, Graham L Collingridge, and Zhengping Jia. "The C-terminal tails of endogenous GluA1 and GluA2 differentially contribute to hippocampal synaptic plasticity and learning." *Nature neuroscience*, **21**(1):50–62, 2018.

[ZRR18] Pengcheng Zhou, Shanna L Resendez, Jose Rodriguez-Romaguera, Jessica C Jimenez, Shay Q Neufeld, Andrea Giovannucci, Johannes Friedrich, Eftychios A Pnevmatikakis, Garret D Stuber, Rene Hen, et al. "Efficient and accurate extraction of in vivo calcium signals from microendoscopic video data." *elife*, **7**:e28728, 2018.

[ZSA86] Stuart Zola-Morgan, Larry R Squire, and David G Amaral. "Human amnesia and the medial temporal region: enduring memory impairment following a bilateral lesion limited to field CA1 of the hippocampus." *Journal of neuroscience*, **6**(10):2950–2967, 1986.